Title

Novel Synthesis and Processing of Lanthanum Telluride (La3-xTe4) Thin Films via Electrophoretic Deposition and Ultrafast High-Temperature Sintering for Advanced High-Temperature Thermoelectric Device Applications

Author

Cheikh, Alexander

Publication Date

2023

Peer reviewed|Thesis/dissertation

UNIVERSITY OF CALIFORNIA

Los Angeles

Novel Synthesis and Processing of Lanthanum Telluride ($La_{3-x}Te_4$) Thin Films via Electrophoretic Deposition and Ultrafast High-Temperature Sintering for Advanced High-Temperature Thermoelectric Device Applications

A dissertation submitted in partial satisfaction of the

requirements for the degree Doctor of Philosophy

in Materials Science and Engineering

by

Alexander Cheikh

2023

ABSTRACT OF THE DISSERTATION

Novel Synthesis and Processing of Lanthanum Telluride ($La_{3-x}Te_4$) Thin Films
via Electrophoretic Deposition and Ultrafast High-Temperature Sintering
for Advanced High-Temperature Thermoelectric Device Applications

by

Alexander Cheikh

Doctor of Philosophy in Materials Science and Engineering

University of California, Los Angeles, 2023

Professor Bruce S. Dunn, Chair

Since the 20th century, deep space missions flown by NASA have been critical for exploration of the solar system and have provided a wealth of fundamental scientific knowledge. Electrical power for these missions is supplied by radioisotope thermoelectric generators (RTG's) which produce electricity from a radioactive heat source. This technology has a history of reliable power generation and has flown on missions such as Pioneer, Cassini, New Horizons, and, most notably, Voyager which has been in continuous operation for over 45 years. However, device efficiency is limited due to the poor heat-to-electricity conversion of thermoelectric materials, which is quantified by the dimensionless figure of merit, ZT. Therefore, a longstanding goal in the field is that of developing higher ZT materials to improve RTG specific power.

Lanthanum telluride ($La_{3-x}Te_4$) has been identified as a prime candidate for next generation RTG's owing to its ZT of 1.1 at 1275K. However, poor machinability and susceptibility to oxidation are current bottlenecks for device fabrication. The overarching goal of

the work presented in this dissertation is to investigate novel processing strategies for $La_{3-x}Te_4$ to facilitate device fabrication and expand pathways for fundamental study of its thermoelectric performance.

The first study (Chapter 2) investigates the $La_{3-x}Te_4$ oxidation mechanism to establish the process by which thermoelectric properties degrade and inform oxide mitigation strategies for synthesis and device fabrication. As-synthesized $La_{3-x}Te_4$ powder contains an amorphous surface oxide at room temperature. At elevated temperature, oxidation progresses with the formation of mobile elemental Te, Te-rich lanthanum telluride phases, and crystalline La_2O_2Te and glassy La_2O_3 as the bulk material reacts with oxygen. The oxide phases are non-passivating and thermodynamically stable, requiring multifaceted oxide mitigation strategies.

The second study (Chapter 3) demonstrates synthesis of $La_{3-x}Te_4$ films by electrophoretic deposition (EPD) using tetrahydrofuran (THF) as solvent. Uniform $La_{3-x}Te_4$ films 10-15 μm thick with a green density of ~65% are deposited on both planar and non-planar substrates. The versatility and scalability of EPD expands thermoelectric device fabrication capabilities and enables study of $La_{3-x}Te_4$-metal composite geometries that are not attainable with current bulk processing methods.

The third study (Chapter 4) utilizes ultrafast high-temperature sintering (UHS) to densify $La_{3-x}Te_4$ films and bulk pellets in as little as 10 seconds. Sample densities >90% can be achieved with well-defined grains on the order of 1-10 μm in size. Rapid densification is proposed to result from the extreme heating rate of UHS which maintains a high driving force for densification and quickly activates diffusion mechanisms that attend fast pore elimination and grain growth. Pressure-less sintering of $La_{3-x}Te_4$ via UHS is a significant achievement and demonstrates that complex pressure sintering techniques are not required for densification.

The fourth study (Chapter 5) investigates the thermoelectric properties of UHS $La_{3-x}Te_4$. Bulk UHS $La_{3-x}Te_4$ pellets achieve a peak ZT of 1.06 at 1273K with comparable performance to optimized $La_{3-x}Te_4$ prepared by established methods. Initial power factor measurements up to 573K suggest that the performance of UHS $La_{3-x}Te_4$ EPD films is similar to bulk UHS $La_{3-x}Te_4$, but more accurate thin film measurement techniques are necessary to fully characterize their ZT. Achievement of high performance $La_{3-x}Te_4$ via UHS greatly expands and simplifies processing of the material without sacrificing thermoelectric performance.

The results of these four studies significantly enhance processing and future device fabrication of $La_{3-x}Te_4$ for high-temperature thermoelectric applications. The detailed understanding of the $La_{3-x}Te_4$ oxidation mechanism informs oxide mitigation strategies for device design. The novel combination of EPD and UHS forms a simple, high-throughput processing scheme that expands possible device architectures while maintaining established thermoelectric performance. Finally, EPD and UHS can be applied to other thermoelectric materials, thus providing unique and adaptable processing enhancements for the broader thermoelectric community.

The dissertation of Alexander Cheikh is approved.

Sabah Bux

Richard B. Kaner

Jaime Marian

Yongho Ju

Bruce S. Dunn, Committee Chair

University of California, Los Angeles

2023

To everyone who has helped me along the way.

Particularly my family, whose unwavering support kept me on solid ground during this journey.

And to Justin, Hemi, Amo Fuad, and especially my father.

"What I've felt, what I've known

Turn the pages, turn the stone

Behind the door, should I open it for you?

What I've felt, what I've known

Sick and tired, I stand alone

Could you be there? 'Cause I'm the one who waits for you

Or are you unforgiven too?"

– The Unforgiven II by Metallica

"Those times when you get up early and you work hard; those times when you stay up late and you work hard; those times when don't feel like working — you're too tired, you don't want to push yourself — but you do it anyway. That is actually the dream. That's the dream. It's not the destination, it's the journey. And if you guys can understand that, what you'll see happen is that you won't accomplish your dreams. Your dreams won't come true, something greater will."

– Kobe Bryant

Table of Contents

List of Figures

List of Tables

Acknowledgements

This work was performed at UCLA and the California Institute of Technology/Jet Propulsion Laboratory under contract with the National Aeronautics and Space Administration. This work is supported by the NASA Science Missions Directorate's Radioisotope Power Systems program office.

The $La_{3-x}Te_4$ powder starting material for all experiments in Chapter 2, 3, and 4 was synthesized by Brea Hogan. In Chapter 2, XPS data was collected by Dr. Grace Whang. In Chapter 3, XPS data was collected by Yunkai Luo. SEM of as-synthesized $La_{3-x}Te_4$ powder and EPD $La_{3-x}Te_4$ on Cu foil were performed by Dr. Grace Whang. SEM of EPD $La_{3-x}Te_4$ on Mo foil and EDX of EPD $La_{3-x}Te_4$ on Ni foil were performed by Dr. Chris Choi. In Chapter 5, $La_{3-x}Te_4$ powder starting material was synthesized by Dr. Kurt Star and Duncan Zavanelli. Measurements of Seebeck coefficient were performed by Greg Gerig. Measurements of thermal diffusivity were performed by George Nakatsukasa. The SPS $LaTe_{1.46}$ samples used for comparison of thermoelectric performance, along with the temperature-dependent thermoelectric data (S, ρ, κ, $S^2\sigma$, and ZT) of those samples, were synthesized, measured, and analyzed by Dr. James Ma.

Chapter 2 and Appendix A are adapted from "Characterization of the Room-Temperature Surface Oxide and High-Temperature Oxidation Mechanism of Lanthanum Telluride ($La_{3-x}Te_4$) via XPS and XRD," which is a manuscript in preparation for publication. It was co-authored with Dr. Christofer Whiting, Brea Hogan, Dr. Sabah Bux, and Professor Bruce Dunn. Dr. Whiting provided input, analysis, and technical discussion to develop the oxidation mechanism and assisted in writing the manuscript. Brea synthesized the starting $La_{3-x}Te_4$ powder for all experiments. Dr. Bux and Professor Dunn were co-principal investigators and provided input for research experiments and writing/preparation of the manuscript.

…

As I put the finishing touches on this dissertation, I begin to write the final and perhaps most important section – the acknowledgements. Ironically, this section is generally agreed amongst my peers to be the most difficult part of the entire dissertation to write, and for good reason. It is a somewhat rare moment to have the culmination of five years' work completed and neatly organized all in one place, providing an interesting calm after countless hours, weeks, and years of grinding. While most of the Ph.D. is spent focusing on the intricate details of research and experiments, writing the dissertation is a unique chance to step back and reflect on the overall journey.

It is not lost on me how remarkable of a personal achievement this is, and I take great pride in the body of work I have put together. However, I by no means did it alone and I have been extremely fortunate to have the help, guidance, support, mentorship, and friendship of countless individuals throughout my academic career. To make a list thanking everyone that has helped me along the way would surely occupy a document longer than the dissertation itself. Therefore, I am given the difficult task of thanking as many individuals as possible with the space I have available. To those whom I do not specifically mention by name, please know that I am still extremely appreciative of you all.

I begin by thanking my advisor, Professor Bruce Dunn. I am beyond grateful for the opportunity to pursue my degree as a member of your group. Your constant support, guidance, leadership, and mentorship have helped me grow so much academically and personally. You have fostered an open, positive, and collaborative lab dynamic that is reflected in each group member. I am appreciative of your encouragement to explore all kinds of experiments and

fundamental science without being afraid to fail. You have taught me perseverance during the inevitable difficulties of research and to always push myself to be better.

Thank you to my JPL advisor, Dr. Sabah Bux. You have likewise given me the incredible and unique opportunity to pursue my Ph.D. not only at UCLA but also as a member of the JPL community. Your constant support and mentorship have helped me become a better researcher. I am appreciative of all the long hours you have spent helping me plan and perform experiments as well as discuss results. Thank you for all that you have taught me and all that you have done to make my Ph.D. possible.

Thank you to Dr. Bryan McEnerney for the amazing opportunity to do an undergraduate internship in your group and live out a childhood dream of working on space missions at JPL. That experience undoubtedly set the foundation for where I am today and what I will accomplish in the future. Your continued support and mentorship are greatly appreciated, and I am thankful for everything you have done to help me.

Thank you to my doctoral committee, Professor Jaime Marian, Professor Richard Kaner, and Professor Sungtaek Ju, for your helpful input and support of my research.

Thank you to the many current and former members and collaborators of the JPL thermoelectrics group (Dr. Ike Chi, Araseli Cortez, Dr. Fivos Drymiotis, Dr. Chris Whiting, Billy Li, George Nakatsukasa, Greg Gerig, Dr. Kurt Star, Duncan Zalvanelli, Professor Susan Kauzlarich, Dr. Chris Perez, Dr. Andy Justl, Dr. Paul Von Allmen, Dr. Trinh Vo, Professor David Dunand, Alex Proschel, Ming Chen, Yunjia Zhang, Alan Fung, Professor Shahab Derakhshan, Allison Garavito, Leah Webb, Bavley Mobarak, Patrick Pham, Professor Richard Blair) who have provided me with great research discussion and input, help setting up and running experiments, and friendly and entertaining conversations.

Thank you to the Dunn Lab members past and present who have made my undergraduate and graduate experiences at UCLA beyond enjoyable. Thank you to Dr. Esther Lan, Dr. David Ashby, Dr. Danielle Butts, Dr. Chris Choi, Dr. Jon Lau, Dr. Terri Lin (Tolbert Lab), Dr. Grace Whang, Dr. Ryan DeBlock, and Dr. Chun-Han Lai for helping me get started in the lab, providing me invaluable advice, guidance and assistance with research, and fun social times in and out of the lab. Thank you to Dr. Patricia McNeil for being an incredible friend, lab mate, and mentor. Thank you to Brea Hogan for all your critical help and support with research. Thank you to Yunkai Luo, Randy Chen, Jacky Yu, Bintao Hu, Winnie Hsieh, Mingyu Jung, Justin Huang, Makena White, Maggie Fox, Henry Choi, Peter Cao, Kyle Kotanchek, and Kyle Fujisaka for all your support and making the lab a fun place to be. Thank you to Alexandra Sangster for your help and for the opportunity to be your mentor – I look forward to seeing all the great things you'll accomplish.

Thank you to all the friends I have made during my time at UCLA. Thank you to the CNSI Outreach program and Dr. Elaine Morita, Dr. Cheylene Tanimoto, and Dr. Rita Blaik for the incredible opportunity to volunteer and help make a positive impact in the community. Thank you to Dr. Tait McLouth and Nicole Carpentier for your support, friendship, and fun food/movie nights. Thank you to Andrew Nuss for being a great mentor and friend. Thanks to F Dawg for all the fun times, basketball talk, emotional support, and epic workouts. Thanks to David for being an awesome friend and for all our deep intellectual conversations. Thanks to Connor for our great basketball conversations and funny jokes during class. I am forever indebted to the Undergrad Squad (Jason, Jon, Ray, Taran, Tim, Angelo, Tiffany, Helen, and Ben) for always being there for me and for encouraging me to truly be myself. I am grateful for all of you and all the amazing memories we've made.

Thank you to Alex and the Barry family, Chris, Joey, Noah, Anthony, Sean, Cory, Dan, Ira, Gary, Jose and the Palomares family, and the Carr family for being great friends and friends of my family. To Justin, thank you for inspiring me to make the world a better place. To James, Lars, Kirk, Rob, Cliff, and Jason, I am eternally grateful for everything you have done to inspire me, provide a constant source of sanity, and create so much positivity for the world. To Kobe, thank you for all your inspiration, teaching me the importance of discipline, hard work and attention to detail, and showing me that anything is possible.

Finally, I must close with the most important thanks of all, and that is to my family. To Mohamed, Dean, Nina, and Mom, none of this was possible without your constant support. Thank you for always believing in me and for everything you have done and continue to do to allow me to pursue my dreams. To Raekwon, thank you for always being there for me no matter what. To Hemi, thanks for all the joy you brought to everyone you met. To Ba, thank you for giving me the tools I needed to be successful in life – miss you and love you. Thank you to everyone else in the family for your support and your belief in me.

Fiat Lux Æterna

Vita

2014-2018	Bachelor of Science in Materials Science and Engineering Magna Cum Laude University of California, Los Angeles
2016	Undergraduate Student Researcher Bruce Dunn Lab, Department of Materials Science and Engineering University of California, Los Angeles
2017-2018	Undergraduate Student Intern (Year-Round) Materials and Processes Group Jet Propulsion Laboratory (JPL)
2018-2023	Graduate Student Researcher Bruce Dunn Lab, Department of Materials Science and Engineering University of California, Los Angeles
2018-2023	Graduate Student Researcher Thermal Energy Conversion Materials Group Jet Propulsion Laboratory (JPL)

Publications

A. Cheikh, C. E. Whiting, B. Hogan, S. K. Bux, B. S. Dunn, "Characterization of the Room-Temperature Surface Oxide and High-Temperature Oxidation Mechanism of Lanthanum Telluride ($La_{3-x}Te_4$) via XPS and XRD," (2023) *Manuscript in Preparation*

Chapter 1 Introduction and Motivation

1.1 Background on Thermoelectric Materials, Devices, and Applications

Worldwide energy needs are steadily increasing as evidenced by the predicted 40% increase in global energy consumption from 2020 to 2040.[1] Meeting these energy demands by increased use of fossil fuels is undesirable due to the harmful environmental effects of CO_2 production. There is a considerable push towards expanding renewable energy production as a way of meeting energy needs while simultaneously achieving the Paris Agreement goal of net-zero CO_2 emissions by 2050.[2,3] An abundant source of "free" energy is the substantial amount waste heat produced as a byproduct of most energy-generation, industrial/manufacturing, and transportation processes. For example, it is estimated that between 60-70% of energy in combustion engines[1] 40-65% of energy in Portland cement production[4], and 67% of electrical energy production[5] is lost as waste heat. In total, approximately 33% of the energy used by manufacturing industries alone is lost as waste heat which equates to 1.72 billion barrels of oil annually, or nearly 25% of the United States' total oil consumption in 2021.[5,6]

One promising method to capture this waste heat into useable energy is thermoelectrics, which can be used for zero-emission, direct conversion of heat energy into electricity.[7,8] Thermoelectric materials produce a voltage in response to an applied temperature gradient and vice versa via the thermoelectric effect. They are incorporated into thermoelectric devices that produce electricity from applied temperature gradients (thermoelectric generators) or provide active cooling from applied electrical power (thermoelectric coolers). Such devices are quite

reliable due to their solid-state operation and offer the potential for quiet, compact, easy-to-maintain, and environmentally-friendly waste-heat recovery and refrigeration.[8–10]

Despite their advantages, a major drawback of thermoelectric devices is their low conversion efficiency which makes them cost prohibitive for many applications. The performance of a thermoelectric material is characterized by the dimensionless figure of merit, *ZT*, defined as:

$$ZT = \frac{S^2\sigma}{\kappa}T \qquad \text{(Equation 1.1)}$$

where S is Seebeck coefficient, σ is electrical conductivity, κ is thermal conductivity, and T is temperature.

The efficiency of a thermoelectric generator depends on the average *ZT* of the material and the temperature difference between the hot side (T_H) and cold side (T_C):[7]

$$\eta_{max} = \frac{T_H - T_C}{T_H}\frac{\sqrt{1+ZT_{avg}}-1}{\sqrt{1+ZT_{avg}}+\frac{T_C}{T_H}} \qquad \text{(Equation 1.2)}$$

where η_{max} is the maximum device efficiency, T_H is the hot-side temperature, T_C is the cold-side, and ZT_{avg} is the dimensionless figure of merit defined in (Equation 1.1), evaluated at an average temperature T_{avg}.

Based on (Equation 1.2), strategies for improving device efficiency include increasing the temperature gradient (T_H - T_C) and increasing *ZT*. Since a material's thermoelectric properties are typically optimized over a narrow temperature range (Figure 1.1A) and operating temperatures are usually fixed by existing design constraints, improvement of *ZT* is the main focus of thermoelectric research. *ZT* has no theoretical upper limit[5,7] and, as it approaches infinity, the second term in (Equation 1.2) becomes unity such that the device efficiency equals the Carnot efficiency.

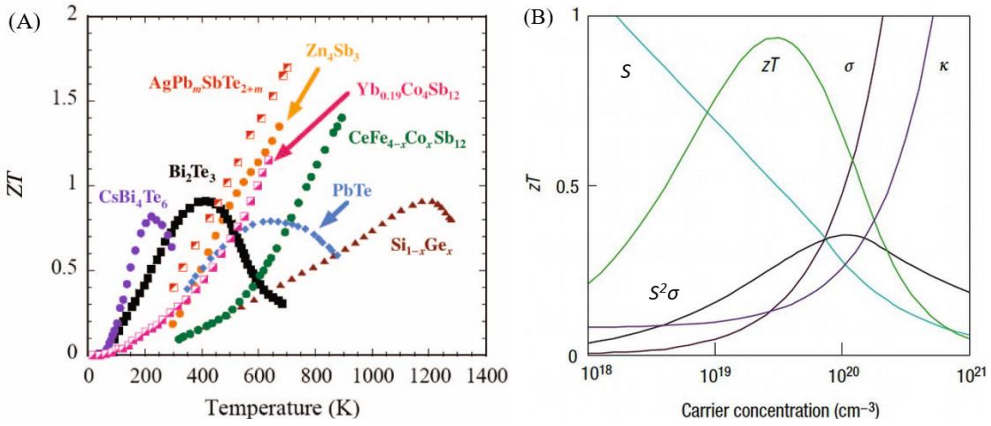

Figure 1.1: (A) (reprinted from Tritt *et al*, Thermoelectric Materials, Phenomena, and Applications: A Bird's Eye View, *MRS Bull*, vol. 31 (3), 188-194, **2006**[7]) ZT vs. temperature for various thermoelectric materials. (B) (reprinted from Tuyen *et al*, Nanostructuring Bi2Te3-Based Thermoelectric Thin-Films Grown Using Pulsed Laser Deposition. *Nanocrystals* **2021**[11]) Thermoelectric properties (ZT, Seebeck coefficient, electrical conductivity, thermal conductivity, and power factor) as a function of carrier concentration.

Slack described the ideal thermoelectric material to maximize *ZT* as a phonon glass/electron crystal[12], meaning it should be a poor conductor of heat (like an amorphous material) and an excellent conductor of electricity (like a crystalline material). In practice, this combination of properties is contradictory since good electrical conductors are also usually good thermal conductors. Therefore, as highlighted in Figure 1.1B, difficulties in improving *ZT* arise due to the interdependence of Seebeck coefficient (S), electrical conductivity (σ), and thermal conductivity (κ), where a favorable change in one property leads to an unfavorable change in the others. For this reason, state-of-the-art thermoelectric materials have long been limited to $ZT \leq$ ~1 despite the fact there is no theoretical upper limit on its value.[5,7] For widespread adoption of thermoelectric materials, *ZT* should be ~2-4 to be competitive with traditional systems such as internal combustion engines for power generation and compressor systems for cooling.[5,8,13]

Despite attempts over the past several decades to decouple electronic and thermal properties, the highest *ZT* materials remain limited to about 1.8-2.5 using advanced nano-structuring, complex hierarchical structures, and band diagram engineering.[14,15] The associated

low conversion efficiency constrains the use of thermoelectrics to specialized applications where the cost is justifiable, spurring considerable research in these areas. One such application is radioisotope thermoelectric generators (RTG's) for deep space missions, where reliable and sustained power output is critical.[5,9]

In an RTG, thermoelectric modules convert the heat produced from decay of a radioactive fuel source into electricity to power various electrical systems on the spacecraft. [5,16] The design and solid-state operation of RTG's afford them excellent reliability, allowing for decades of sustained power output.[5, 17] RTG's based on traditional thermoelectric materials such as SiGe, PbTe, and Te-Sb-Ge-Ag (TAGS) have heat-to-electricity conversion efficiencies around 6.5% due to their *ZT* values ≤ 1.[5, 17, 18, 19, 20] A long-standing goal in the field is that of creating higher *ZT* materials to increase conversion efficiency and improve device specific power (W/kg). SiGe, which is regarded as the high-temperature benchmark, was used for Voyager's MHW-RTG (remains in continuous operation after 45+ years) and Cassini's GPHS-RTG (operated for almost 20 years before mission termination) which produced 4.2 W/kg and 5.2 W/kg, respectively.[21] Recent research conducted by JPL has established lanthanum telluride ($La_{3-x}Te_4$) as a favored candidate to improve upon the performance of SiGe for next-generation RTG applications.[9,22,23]

1.2 Lanthanum Telluride ($La_{3-x}Te_4$) – Background and Thermoelectric Performance

Lanthanum telluride ($La_{3-x}Te_4$) is a state-of-the-art n-type thermoelectric material with a *ZT* of about 1.1 at 1275K.[9] The high *ZT* is a consequence of the intrinsically low thermal conductivity afforded by the complex crystal structure as well as the tunable electronic properties which are controlled by the lanthanum vacancy concentration, *x*, where $0 \leq x \leq 1/3$ with an optimized value of $x = 0.23$ for peak thermoelectric performance.[9,19,20,22] The *ZT* of $La_{3-x}Te_4$

exceeds other n-type thermoelectrics (Figure 1.2A) and provides a significant increase over heritage RTG SiGe above 900K. Replacing SiGe with $La_{3-x}Te_4$ could potentially double thermoelectric couple efficiency to ~15%.[19] Furthermore, the *ZT* of $La_{3-x}Te_4$ can be increased above its baseline performance by compositing with spherical Ni inclusions via composite-assisted funneling of electrons (CAFE), achieving as high as 1.9 at 1200K (Figure 1.2B).[23,24] Modeling suggests that varying the morphology of Ni inclusions (such as parallel slabs or wires) may enhance *ZT* even further.[25] Additionally, experimental results and theoretical predictions for other thermoelectric materials systems indicate that reducing the dimensionality of a thermoelectric may decouple the electrical and thermal conductivity, potentially allowing for additional improvement of *ZT* via thin film fabrication.[15]

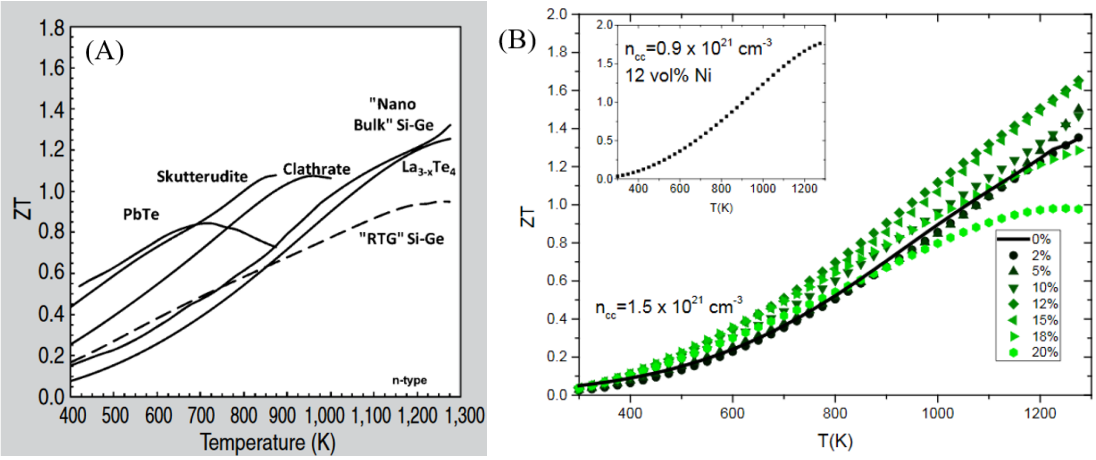

Figure 1.2: (A) (reprinted from Fleurial, Thermoelectric Power Generation Materials: Technology and Application Opportunities. *JOM*, *61* (4), 79–85l, **2009**[5]) ZT vs. temperature for various high-performance n-type thermoelectrics. (B) (reprinted from Ma, Improving the Mechanical Strength and Power Conversion Efficiency of High Temperature Thermoelectrics, UCLA, Los Angeles, 2014[24]) ZT vs. temperature for $La_{3-x}Te_4$-Ni composites at varying Ni volume fractions.

1.3 Traditional Processing of $La_{3-x}Te_4$ and Present Challenges

Synthesis of $La_{3-x}Te_4$ is currently achieved through mechanical alloying of elemental La and Te in stoichiometric amounts to produce $La_{3-x}Te_4$ powder followed by densification of the

powder through spark plasma sintering (SPS) or hot pressing to produce dense compacts.[9,22,23] Development of this synthesis strategy was a breakthrough for studying the thermoelectric performance of lanthanum telluride since it mitigated obstacles such as La oxidation sensitivity, Te vapor loss, high-temperature processing, and incongruent melting that hindered previous melt synthesis and solid-state diffusion routes.[9] With a well-established synthesis route and demonstrated state-of-the-art thermoelectric performance, the next stage of $La_{3-x}Te_4$ processing is device fabrication. However, $La_{3-x}Te_4$ faces additional materials and processing challenges that currently limit its incorporation into a device.

Thermoelectric device fabrication requires the synthesized pellets to be mechanically machined into the desired geometry followed by metallization, diffusion bonding, and/or brazing to make electrical and thermal contact.[24,26] $La_{3-x}Te_4$ is brittle, reactive, and extremely oxygen sensitive which makes its incorporation into a device difficult since each processing step adds complexity and provides a point at which $La_{3-x}Te_4$ is susceptible to mechanical failure, chemical reaction, or oxidation. As a result, no comprehensive processing strategy yet exists for $La_{3-x}Te_4$ device fabrication. Additionally, in the case of $La_{3-x}Te_4$-Ni composites, current synthesis involving SPS or hot pressing limits Ni inclusions to a spherical morphology[23] which impedes experimental validation of the modeled enhancements in *ZT* from other morphologies. Furthermore, there is broader community interest in producing thermoelectric thin films as a possible route for improving thermoelectric performance due to stalling improvements in bulk materials, in addition to reducing weight and expanding possible device architectures.[8,15,27,28]

Current $La_{3-x}Te_4$ research is thus multifaceted and focused on establishing both device processing strategies and routes for further fundamental study of thermoelectric properties. These areas include overcoming the materials and processing challenges associated with device

fabrication, establishing additional synthesis and processing schemes to expand potential device architectures, developing synthesis strategies for varying Ni inclusion morphologies, and synthesizing thin films to study the effects of microstructure and dimensionality on thermoelectric properties.

1.4 Objectives of the Dissertation

The dissertation work is motivated by NASA and JPL's interest in $La_{3-x}Te_4$ for use in next-generation RTG's. It aims to address several of the materials and processing limitations of $La_{3-x}Te_4$ to enhance JPL's capabilities in thermoelectric materials and devices. The investigation relates to developing facile, adaptable synthesis and processing strategies which are applicable for both device fabrication and synthetic methods for fundamental study of thermoelectric performance.

The research presented is comprised of four interconnected elements: 1) characterizing $La_{3-x}Te_4$ oxidation to obtain improved understanding of the underlying oxide formation mechanisms and inform strategies to prevent deleterious effects of oxidation during processing and in service; 2) developing a quick, facile method for depositing $La_{3-x}Te_4$ films and coatings via electrophoretic deposition; 3) developing a novel rapid sintering approach to densify $La_{3-x}Te_4$ in as little as 10 seconds which is combined with electrophoretic deposition to create a high-throughput processing scheme for films and coatings; and 4) characterizing thermoelectric properties to establish baseline performance. The results of this work significantly improve synthesis and processing of $La_{3-x}Te_4$ compared to current methods. They represent significant enhancement to JPL's capabilities in thermoelectrics and establish additional strategies for device fabrication and fundamental study of thermoelectric properties.

1.5 References

(1) Hewawasam, L. S.; Jayasena, A. S.; Afnan, M. M. M.; Ranasinghe, R. A. C. P.; Wijewardane, M. A. Waste Heat Recovery from Thermo-Electric Generators (TEGs). *Energy Reports* **2020**, *6*, 474–479. https://doi.org/10.1016/J.EGYR.2019.11.105.

(2) *Net Zero Coalition | United Nations*. https://www.un.org/en/climatechange/net-zero-coalition (accessed 2023-04-23).

(3) Rockström1, J.; Gaffney1, O.; Rogelj3, J.; Meinshausen5, M.; Nakicenovic3, N.; Schellnhuber1, H. J. A Roadmap for Rapid Decarbonization.

(4) Luo, Q.; Li, P.; Cai, L.; Zhou, P.; Tang, D.; Zhai, P.; Zhang, Q. A Thermoelectric Waste-Heat-Recovery System for Portland Cement Rotary Kilns. *J Electron Mater* **2015**, *44* (6), 1750–1762. https://doi.org/10.1007/S11664-014-3543-1/METRICS.

(5) Fleurial, J. P. Thermoelectric Power Generation Materials: Technology and Application Opportunities. *JOM* **2009**, *61* (4), 79–85. https://doi.org/10.1007/S11837-009-0057-Z/METRICS.

(6) *Frequently Asked Questions (FAQs) - U.S. Energy Information Administration (EIA)*. https://www.eia.gov/tools/faqs/faq.php?id=33&t=6 (accessed 2023-04-23).

(7) Tritt, T. M.; Subramanian, M. A. Thermoelectric Materials, Phenomena, and Applications: A Bird's Eye View. *MRS Bull* **2006**, *31* (3), 188–194. https://doi.org/10.1557/MRS2006.44/METRICS.

(8) Xiao, F.; Hangarter, C.; Yoo, B.; Rheem, Y.; Lee, K. H.; Myung, N. V. Recent Progress in Electrodeposition of Thermoelectric Thin Films and Nanostructures. *Electrochim Acta* **2008**, *53* (28), 8103–8117. https://doi.org/10.1016/J.ELECTACTA.2008.06.015.

(9) May, A. F.; Fleurial, J. P.; Snyder, G. J. Thermoelectric Performance of Lanthanum Telluride Produced via Mechanical Alloying. *Phys Rev B Condens Matter Mater Phys* **2008**, *78* (12), 125205. https://doi.org/10.1103/PHYSREVB.78.125205/FIGURES/11/MEDIUM.

(10) Yoo, I. J.; Myung, N. V.; Lim, D. C.; Song, Y.; Jeong, Y. K.; Kim, Y. Do; Lee, K. H.; Lim, J. H. Electrodeposition of BixTey Thin Films for Thermoelectric Application. *Thin Solid Films* **2013**, *546*, 48–52. https://doi.org/10.1016/J.TSF.2013.05.036.

(11) Tuyen, L. T. C.; Le, P. H.; Jian, S.-R.; Tuyen, L. T. C.; Le, P. H.; Jian, S.-R. Nanostructuring Bi2Te3-Based Thermoelectric Thin-Films Grown Using Pulsed Laser Deposition. *Nanocrystals [Working Title]* **2021**. https://doi.org/10.5772/INTECHOPEN.99469.

(12) Slack, G. New Materials and Performance Limits for Thermoelectric Cooling. *CRC Handbook of Thermoelectrics* **1995**. https://doi.org/10.1201/9781420049718.CH34.

(13) Mahan, G. D.; Balseiro, Ti.; Atomico Bariloche, C. The Best Thermoelectric. *Proc Natl Acad Sci U S A* **1996**, *93* (15), 7436. https://doi.org/10.1073/PNAS.93.15.7436.

(14) Zhang, X.; Zhao, L. D. Thermoelectric Materials: Energy Conversion between Heat and Electricity. *Journal of Materiomics* **2015**, *1* (2), 92–105. https://doi.org/10.1016/J.JMAT.2015.01.001.

(15) Chen, X.; Zhou, Z.; Lin, Y. H.; Nan, C. Thermoelectric Thin Films: Promising Strategies and Related Mechanism on Boosting Energy Conversion Performance. *Journal of Materiomics* **2020**, *6* (3), 494–512. https://doi.org/10.1016/J.JMAT.2020.02.008.

(16) Rinehart, G. H. Design Characteristics and Fabrication of Radioisotope Heat Sources for Space Missions. *Progress in Nuclear Energy* **2001**, *39* (3–4), 305–319. https://doi.org/10.1016/S0149-1970(01)00005-1.

(17) Cook, B. Silicon-Germanium: The Legacy Lives On. *Energies (Basel)* **2022**, *15* (8), 2957.

(18) Tritt, T. M.; Subramanian, M. A. Thermoelectric Materials, Phenomena, and Applications: A Bird's Eye View. *MRS Bull* **2006**, *31* (3), 188–194. https://doi.org/10.1557/MRS2006.44/METRICS.

(19) Ma, J. M.; Clarke, S. M.; Zeier, W. G.; Vo, T.; Von Allmen, P.; Jeffrey Snyder, G.; Kaner, R. B.; Fleurial, J. P.; Bux, S. K. Mechanochemical Synthesis and High Temperature Thermoelectric Properties of Calcium-Doped Lanthanum Telluride La3−xCaxTe4. *J Mater Chem C Mater* **2015**, *3* (40), 10459–10466. https://doi.org/10.1039/C5TC01648G.

(20) Cheikh, D.; Hogan, B. E.; Vo, T.; Von Allmen, P.; Lee, K.; Smiadak, D. M.; Zevalkink, A.; Dunn, B. S.; Fleurial, J. P.; Bux, S. K. Praseodymium Telluride: A High-Temperature, High-ZT Thermoelectric Material. *Joule* **2018**, *2* (4), 698–709. https://doi.org/10.1016/J.JOULE.2018.01.013.

(21) Bennett, G. L. Space Nuclear Power. *Encyclopedia of Physical Science and Technology* **2003**, 537–553. https://doi.org/10.1016/B0-12-227410-5/00715-8.

(22) May, A. High-Temperature Transport in Lanthanum Telluride and Other Modern Thermoelectric Materials, California Institute of Technology, Pasadena, 2010.

(23) Cheikh, D. Synthesis and Characterization of Rare-Earth Tellurides and Their Composites for High-Temperature Thermoelectric Applications, UCLA, Los Angeles, 2017.

(24) Ma, J. Improving the Mechanical Strength and Power Conversion Efficiency of High Temperature Thermoelectrics, UCLA, Los Angeles, 2014.

(25) Bergman, D. J.; Fel, L. G. Enhancement of Thermoelectric Power Factor in Composite Thermoelectrics. *J Appl Phys* **1999**, *85* (12), 8205–8216. https://doi.org/10.1063/1.370660.

(26) Sadia, Y.; Koron, I.; Gelbstein, Y. PbO-SiO2 Based Glass Coating of PbI2 Doped PbTe. *Metals 2020, Vol. 10, Page 284* **2020**, *10* (2), 284. https://doi.org/10.3390/MET10020284.

(27) Chi, S. chih. Novel Syntheses of Thermoelectric and Nanostructured Materials and a System for Purifying and Sorting Metallic and Semiconducting Single Walled Carbon Nanotubes in a Mixed Tube Suspension, Johns Hopkins, 2014. https://jscholarship.library.jhu.edu/handle/1774.2/37038 (accessed 2023-04-05).

(28) Chi, S. C.; Farias, S. L.; Cammarata, R. C. A Novel Approach to Synthesize Lanthanum Telluride Thermoelectric Thin Films in Ambient Conditions. *Materials Research Society Symposium Proceedings* **2013**, *1543* (1), 113–118. https://doi.org/10.1557/OPL.2013.929/METRICS.

Chapter 2 Characterization of the $La_{3-x}Te_4$ Oxidation Mechanism

2.1 Introduction and Motivation for Understanding Oxidation of $La_{3-x}Te_4$

One of the most significant materials challenges for $La_{3-x}Te_4$ is its sensitivity and susceptibility to oxidation which necessitates meticulous preparation procedures to avoid oxygen exposure during handling, processing, and designing of service conditions.[1–3] The most common oxide phase reported in the literature, La_2O_2Te, is detrimental to the thermoelectric properties and mechanical stability of $La_{3-x}Te_4$ since it is electrically resistive and extremely brittle.[1,4] Additionally, the presence of La_2O_2Te inhibits adequate sintering which is necessary to achieve high densities for optimum thermoelectric performance.[1] $La_{3-x}Te_4$ has been shown to oxidize significantly even under low partial pressures of oxygen ≤1 kPa.[4] As a result, a paramount concern during synthesis, preparation, and characterization of $La_{3-x}Te_4$ is avoiding oxidation, which is accomplished through deliberate handling in high-purity inert conditions.[1–3] Even with these precautions, partial oxidation to La_2O_2Te can still occur during high temperature thermoelectric measurements, though the presence of small amounts of the oxide do not appreciably alter thermoelectric performance.[5]

Despite these materials challenges, there is a lack of information in the literature studying oxidation of $La_{3-x}Te_4$. Research pertaining to $La_{3-x}Te_4$ acknowledges many of the issues associated with oxidation of the material but as of yet there have been only limited investigations into the underlying mechanisms of oxide formation.[1–3,5] Initial work conducted by JPL indicates that, at room temperature, $La_{3-x}Te_4$ forms an amorphous surface oxide consisting of La_2O_3, TeO_2, and elemental Te.[6] Recently, Li *et al* investigated the kinetics of oxide formation at high temperature in $La_{3-x}Te_4$ and $La_{3-x}Te_4$-Ni composites and demonstrated a significant degree of

oxidation to La_2O_2Te even under low partial pressures of oxygen, though Ni inclusions in the composite may form an oxygen barrier at the surface to slow oxide formation kinetics.[4]

The overarching goal of the research presented in this chapter is to experimentally characterize $La_{3-x}Te_4$ oxide formation via XPS and XRD to develop a more comprehensive understanding of the surface and bulk $La_{3-x}Te_4$ oxidation mechanisms. Knowledge of the chemical reactions between oxygen and $La_{3-x}Te_4$ provides information on the transformation of observed low-temperature amorphous oxide phases to the high-temperature La_2O_2Te phase. A thermodynamic analysis demonstrates the stability of the oxide phases at low oxygen partial pressures. The results inform proposed oxide mitigation strategies for $La_{3-x}Te_4$ synthesis, processing, and service conditions.

2.2 Experimental Methods

$La_{3-x}Te_4$ powder was synthesized using established mechanochemical methods.[5] Briefly, elemental La and Te were combined in the stoichiometric amounts and ball milled to achieve the alloyed powder. The elemental reactants were handled in an Ar-filled glovebox and the ball mill vial was sealed under Ar. The resulting as-synthesized $La_{3-x}Te_4$ powder was used without further treatment. The surface species of the as-synthesized powder at room temperature were characterized by X-ray photoelectron spectroscopy (XPS). Bulk phases of the as-synthesized powder were characterized by X-ray diffraction (XRD) at room temperature and after the furnace heat treatments described below.

Heat treatments were performed by adding approximately 50 mg of powder into a graphite crucible and loading it into in a tube furnace (MTI OTF-1200X). Ultra-high purity forming gas (nominal O_2 content of 1 ppm) (Airgas, mixture of 95% Ar and 5% H_2) flowed continuously at 15 mL/min during the entire experiment. After loading of the samples, the tube

was purged for two hours prior to heating to remove oxygen. The powder was then heated to the specified temperature and held for 2 hours. The heating/cooling rate in all cases was 3.33 ^{o}C/min. Figure 2.1 shows the general temperature vs. time profile.

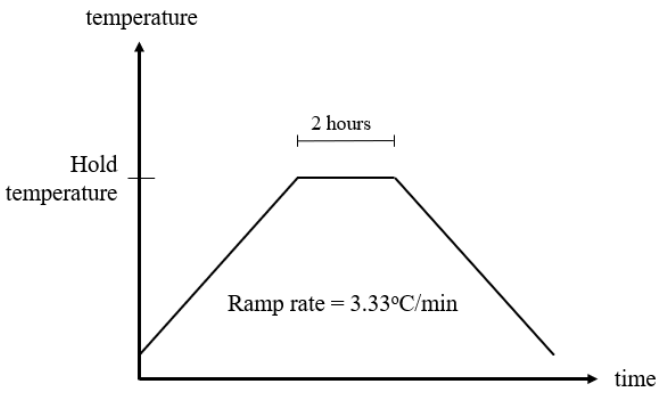

Figure 2.1. Temperature vs. time profile for heat treatment of $La_{3-x}Te_4$ powder in the tube furnace under flowing forming gas (95% Ar, 5% H_2).

2.3 XPS Characterization of $La_{3-x}Te_4$ Powder Room-Temperature Surface Oxide

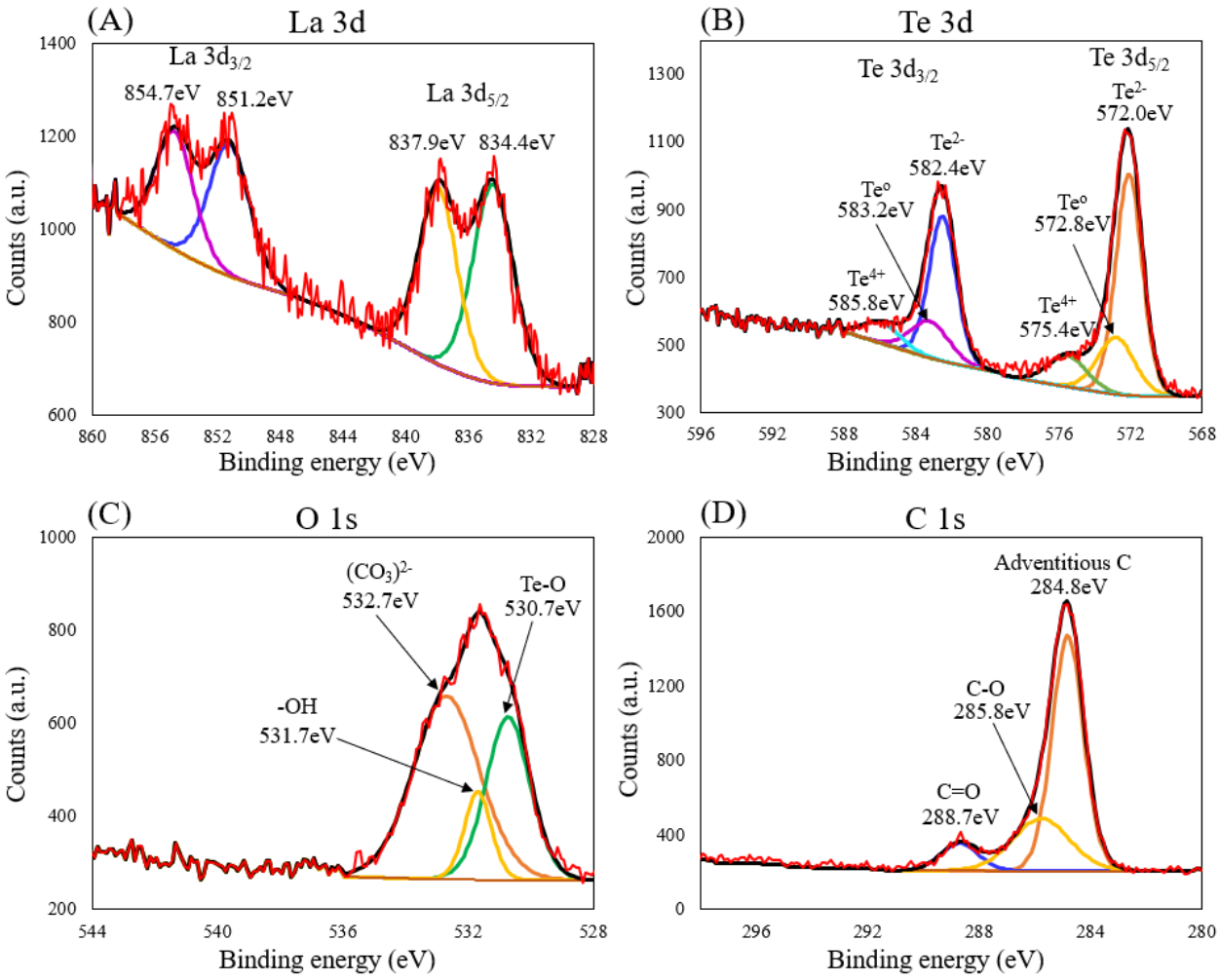

Figure 2.2. XPS scans of as-synthesized $La_{3-x}Te_4$ powder, showing the (A) La 3d, (B) Te 3d, (C) O 1s, and (D) C 1s regions. The binding energies and associated valence states or chemical bonds for fitted components are listed. (A) In the La 3d region, the two pairs of peaks are fit with four components corresponding to La^{3+}. (B) In the Te 3d region, there are a pair of peaks that are comprised of three components, with each component corresponding to Te^{2-} (La-Te), Te^0 (elemental Te), and Te^{4+} (Te-O). (C) The broad O 1s peak is fit with three components corresponding to -OH groups, $(CO_3)^{2-}$ groups, and Te-O bonding. (D) In the C 1s region, the adventitious carbon component is used for binding energy reference to 284.8eV. The other two components are associated with C-O and C=O bonding.

XPS was employed to analyze the surface species of as-synthesized powder at room temperature. The main results and analysis are presented here, and a detailed discussion is presented in Appendix **Error! Reference source not found.**. Figure 2.2 shows the XPS spectra f or the La 3d, Te 3d, O 1s, and C 1s regions. The fitted binding energy values and associated

valence states and chemical bonds are summarized in Table 2.1. The La 3d signal (Figure 2.2A) exhibits spin-orbit and multiplet splitting (four components corresponding to one valence state) which is associated with La^{3+}.[7] The Te 3d signal (Figure 2.2B) exhibits three cases of spin-orbit splitting (six components corresponding to three valence states), which are consistent with Te^{2-}, Te^{4+}, and Te^{0}.[8–10] La^{3+} and Te^{2-} are associated with La-Te bonding which would be expected in $La_{3-x}Te_4$ and is supported by the similarity in component binding energies to literature values for La_2Te_3 nanowires.[11] However, the binding energy difference of 3.5eV between the La^{3+} main and satellite components[7] along with the presence of Te^{4+} and Te^{0} [9, 10] provide evidence of additional surface oxide, hydroxide, and carbonate species. Analysis of the O 1s (Figure 2.2C) and C 1s (Figure 2.2D) regions enable the identification of hydroxyl groups (-OH), tellurium-oxygen (Te-O) bonding, and carbonate groups $(CO_3)^{2-}$.[9,10,12–15] Thus, the as-synthesized $La_{3-x}Te_4$ has a native surface oxide.

Elemental Te (associated with Te^{0}) is often observed in conjunction with tellurium oxide (associated with Te^{4+}) [10] and has been detected on the oxidized surfaces of Pt_3Te_4 [9], CdTe [16], SnTe [17], and PbTe and PbSnTe [18]. In the SnTe system, it has been proposed that Te^{0} formation is an intermediate step in tellurium oxidation according to the sequence [17]:

$$Te^{2-} \xrightarrow{i} Te^{0} \xrightarrow{ii} Te^{4+} \qquad \text{(Equation 2.1)}$$

It has also been reported that partial oxidation of the SnTe surface creates elemental Te via preferential oxidation of Sn.[18]:

$$SnTe + O_2 \rightarrow SnO_2 + Te + \text{unreacted SnTe} \qquad \text{(Equation 2.2)}$$

Sn and Te in the intermetallic begin to oxidize simultaneously, but the reaction of Sn with oxygen is more thermodynamically favorable [19] and Te^{2-} requires two oxidation steps (Equation 2.1) to form TeO_2, so SnO_2 and Te are the initial products of oxidation in (Equation 2.2).[18] Te

subsequently reacts with oxygen to form TeO_2 such that elemental Te and TeO_2 co-exist depending on the relative rates of step *i* and step *ii* in (Equation 2.1).[17] In the SnTe system, an accumulation of Te^0 occurs since the rate of step *i* exceeds that of step *ii*.[17]

A similar mechanism is proposed here for $La_{3-x}Te_4$ in which elemental Te forms as a stable intermediate in the lanthanum telluride oxidation process. Like with Sn in SnTe, the reaction of oxygen with La is also more thermodynamically favorable than with Te, so initial oxidation (Equation 2.3) involves breaking the La-Te bond in $La_{3-x}Te_4$ to form La_2O_3 and Te^0, with Te^0 eventually oxidizing to TeO_2 (Equation 2.4). The reaction of Te^0 with oxygen to form TeO_2 is slower than the initial reaction of $La_{3-x}Te_4$ with oxygen to form La_2O_3 and Te^0 (Equation 2.3) such that elemental Te is present as long as a significant amount of $La_{3-x}Te_4$ remains.

$$La_{3-x}Te_4 + O_2 \rightarrow La_2O_3 + Te + \text{unreacted } La_{3-x}Te_4 \qquad \text{(Equation 2.3)}$$

$$Te + O_2 \rightarrow TeO_2 \qquad \text{(Equation 2.4)}$$

Since there is no La-O bonding peak (528.6 eV) associated with La_2O_3, it is likely that all the La_2O_3 at the surface has reacted to form hydroxide and carbonate species.[7] In the literature, a pure La_2O_3 surface is known to rapidly hydroxylate at room temperature when exposed to moisture and CO_2, forming $La(OH)_3$ and small amounts of oxycarbonate ($La_2O_2CO_3$).[13,14] In the case of $La_{3-x}Te_4$, the formation of full $La(OH)_3$ is unlikely since the addition of each hydroxyl group requires displacing Te, so the (-OH) bonding in the O 1s region (Figure 2.2C) is likely indicative of a partially hydroxylated lanthanum or lanthanum telluride species. Furthermore, the lack of La-O bonding suggests that the carbonate bonding $(CO_3)^{2-}$ identified in the O 1s (Figure 2.2C) and C 1s (Figure 2.2D) regions is associated with a partially carbonated lanthanum telluride surface.

Table 2.1. XPS binding energy values and associated bonds for as-synthesized $La_{3-x}Te_4$ powder.

XPS region	Valence state(s)	Associated bonds	Fitted binding energies (eV)
La 3d	La^{3+}	La-Te, surface hydroxyl and carbonate species	834.4, 837.9, 851.2, 854.9
Te 3d	Te^{2-}	La-Te	572.0, 582.4
	Te^{0}	Elemental Te	572.8, 583.2
	Te^{4+}	Te-O	575.4, 585.8
O 1s	N/A	Te-O	530.7
	N/A	-OH (surface hydroxylation)	531.7
	N/A	$(CO_3)^{2-}$ (surface carbonation)	532.7
C 1s	N/A	Adventitious carbon	284.8
	N/A	C-O	285.8
	N/A	C=O	288.7

These results show that, at room temperature, the as-synthesized $La_{3-x}Te_4$ surface oxidizes to form La_2O_3 and elemental Te, and eventually TeO_2. Any surface oxides that form rapidly react with water and CO_2 to form surface hydroxyl and carbonate groups, respectively, which can occur from exposure to trace amounts of atmosphere or CO_2 during processing, storage, or loading in the XPS chamber.[20] Additionally, as demonstrated by previous research at JPL and corroborated in section 2.4, TeO_2 and La_2O_3 exist in a glassy phase. An illustration of the room-temperature oxidation process is shown in Figure 2.3.

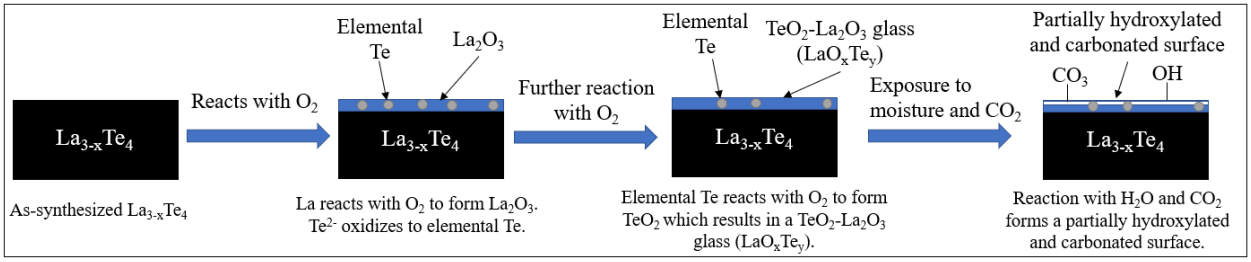

Figure 2.3. Illustration of the formation of a native surface oxide on as-synthesized $La_{3-x}Te_4$ at room temperature. The initially pristine surface quickly reacts with oxygen to form La_2O_3 and elemental Te. Te eventually reacts with oxygen to form TeO_2, leading to the formation of a TeO_2-La_2O_3 glass. Exposure to moisture and CO_2 creates a partially hydroxylated and carbonated surface.

Small quantities of this surface oxide do not noticeably affect thermoelectric performance since the thermoelectric properties of as-prepared $La_{3-x}Te_4$ are well established[5] even though the results shown here indicate the presence of a surface oxide after synthesis. However, a significant amount of surface oxide, which inhibits sintering, is detrimental since densification of $La_{3-x}Te_4$ is crucial to achieve optimum electronic properties for thermoelectric performance. Great care must be taken to avoid air exposure during sample preparation and processing.[1] This sensitivity suggests there is a "shelf-life" for $La_{3-x}Te_4$ powder. The sensitivity to large amounts of oxide is highlighted in the literature, where powders with large values of x are difficult to sinter (achieving <85% density when $x > 0.26$) due to their higher susceptibility to oxidation than samples with low values of x.[1,5] Furthermore, the formation of elemental Te as a result of oxidation is significant since, as discussed in section 2.4, large quantities of Te cause a change in the underlying bulk composition.

2.4 XRD Characterization of $La_{3-x}Te_4$ Powder Oxidation Progression at High Temperature

To further characterize the mechanisms of oxide formation, $La_{3-x}Te_4$ oxidation was studied as a function of temperature by heat treating as-synthesized powder in a tube furnace under flowing forming gas atmosphere (95% Ar, 5% H_2). Oxygen exposure occurred despite the reducing atmosphere and sealed tube furnace, leading to severe oxidation of the powder.

Oxidation of $La_{3-x}Te_4$ is expected even if the oxygen concentration is low because of the thermodynamic stability of the oxide at low oxygen partial pressures (*vide infra*).[21] However, trace oxygen in the forming gas at the upper limit of the gas specification (1ppm) is insufficient to cause the observed extent of oxidation. It is hypothesized that additional oxygen was present due to inadequate purging or a small leak in the furnace since an O_2 level on the order of 100-1000ppm is expected to severely oxidize $La_{3-x}Te_4$.

The powder was characterized by XRD after heat treatment at each temperature. For viewing clarity, only representative XRD scans associated with the most significant changes in bulk phases are shown in Figure 2.4. XRD scans for all heat treatments are shown in Figure 0.1 (Appendix .543). The XRD data in Figure 0.1 provides the basis for Figure 2.5, which is a graphical representation of the phases identified in the XRD scans as a function of heat treatment temperature. The total phases present in the sample, which are determined from additional analysis, are also shown.

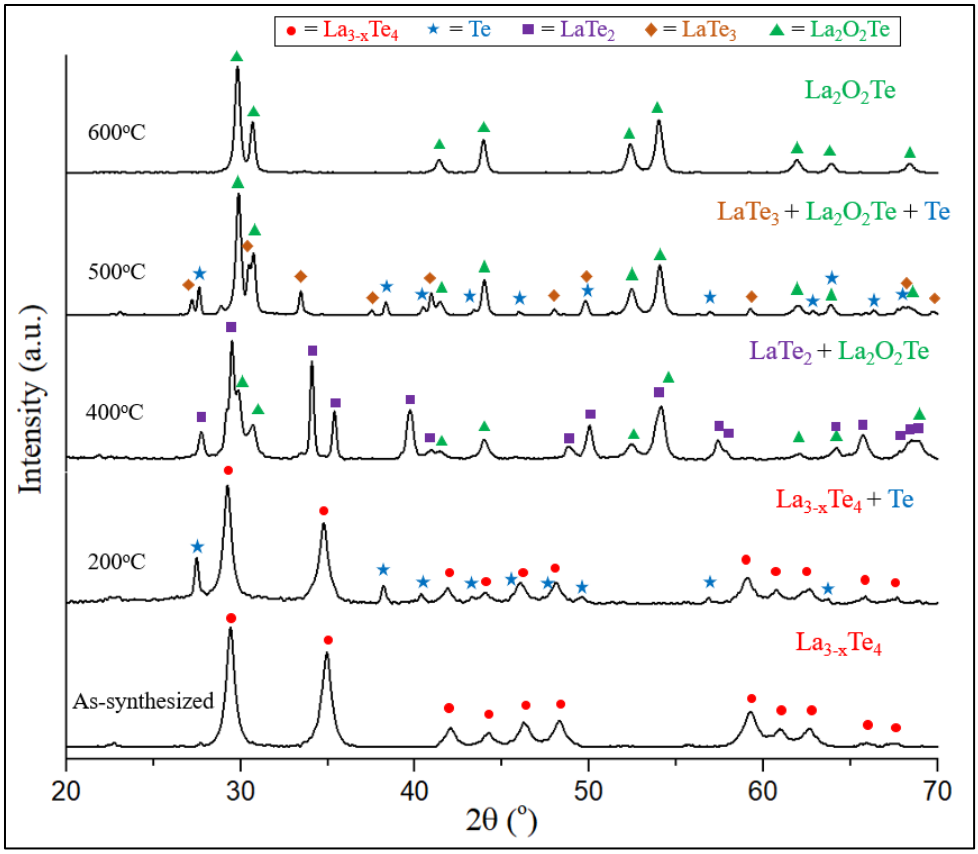

Figure 2.4. XRD scans for $La_{3-x}Te_4$ powder after tube furnace heat treatment for 2 hours in flowing forming gas 95% Ar, 5% H_2. For clarity, only scans associated with representative changes in the bulk phases are shown (scans for all temperatures are shown in Appendix .543 in Figure 0.1). The temperatures for each heat treatment are listed on the left, and identified phases at that heat treatment temperature are listed on the right above the associated scan.

At room temperature and after the 100°C heat treatment, $La_{3-x}Te_4$ is the only phase observed. The oxide is amorphous at these temperatures since there is a known surface oxide from the previous XPS analysis. After the 200°C heat treatment, $La_{3-x}Te_4$ is still present and a second phase identified as metallic Te is observed. After the 300°C heat treatment, the Te peaks are absent, and peaks associated with $LaTe_2$ are identified in addition to $La_{3-x}Te_4$. After the 400°C heat treatment, $LaTe_2$ peaks remain while $La_{3-x}Te_4$ peaks are absent, and crystalline lanthanum oxytelluride, La_2O_2Te, is also identified. This is the first direct observation of oxide in XRD and suggests the surface oxide crystallizes around 400°C. After the 500°C heat treatment,

La_2O_2Te peaks remain while $LaTe_2$ peaks are absent and replaced by $LaTe_3$ and Te metal. La_2O_2Te is the only phase observed after the 600-1000°C heat treatments. Based on the measured mass change of the powder (see Appendix .543), it is expected that in addition to La_2O_2Te, there is also a substantial amount of glassy La_2O_3 present in the sample. The severity of oxidation is significant because the oxide phases are non-passivating, and oxidation of the powder sample occurs well below the typical processing and service temperatures for $La_{3-x}Te_4$ (>1000°C).

T	Phases Identified in XRD Scans	Total Phases Present	T
1000°C	La_2O_2Te	$La_2O_2Te + La_2O_3$ (glass)	1000°C
900°C			900°C
800°C			800°C
700°C			700°C
600°C			600°C
500°C	$LaTe_3 + Te + La_2O_2Te$	$LaTe_3 + Te + La_2O_2Te + La_2O_3$ (glass)	500°C
400°C	$LaTe_2 + La_2O_2Te$	$LaTe_2 + La_2O_2Te + La_2O_3$ (glass)	400°C
300°C	$La_{3-x}Te_4 + LaTe_2$	$La_{3-x}Te_4 + LaTe_2 + LaO_xTe_y$ (glass)	300°C
200°C	$La_{3-x}Te_4 + Te$	$La_{3-x}Te_4 + Te + LaO_xTe_y$ (glass)	200°C
100°C	$La_{3-x}Te_4$	$La_{3-x}Te_4 + Te + LaO_xTe_y$ (glass)	100°C
Room temperature			Room temperature

Figure 2.5. Phases identified via XRD and total phases present for $La_{3-x}Te_4$ powder heat treated for 2 hours in forming gas (95% Ar, 5% H_2) at the listed temperature. XRD scans (shown in Figure 2.4) were taken after heat treatment. The total phases present are determined from the XRD data as well as additional analysis including XPS and mass change.

It is noteworthy that crystalline oxide is not detected in XRD for heat treatments below 400°C despite evidence of oxidation such as the presence of Te at 200°C and $LaTe_2$ at 300°C. It can be concluded then that the oxide is amorphous at low temperatures. The XPS analysis presented in section 2.3 suggests initial oxidation is in the form of a native surface oxide

composed of La_2O_3 and TeO_2 (though there is subsequent reaction to form a partially hydroxylated and carbonated surface). TeO_2 is a known conditional glass former and La_2O_3 can act as a network modifier.[22] Thus, the surface oxide is expected to be a TeO_2-La_2O_3 glassy phase. Additionally, the thermodynamic analysis presented in section 2.5 suggests that the TeO_2-La_2O_3 glass likely exists as an amorphous lanthanum oxytelluride phase (LaO_xTe_y). In the literature, TeO_2-TiO_2-La_2O_3 glass is known to crystallize to $La_2O_{15}Te_6$ at 450°C [23] which is similar to the behavior observed here in which the surface TeO_2-La_2O_3 glass crystallizes to La_2O_2Te at 400°C. As discussed in .543 (sections .543 and .543), a substantial amount of glassy La_2O_3 remains after crystallization of the TeO_2-La_2O_3 glass and is present along with La_2O_2Te at higher temperature. It is expected that formation of La_2O_3 is the most thermodynamically stable state of the system, so co-existence of La_2O_2Te and La_2O_3 suggests that transformation of La_2O_2Te to La_2O_3 may be incomplete due to slow reaction kinetics or a limiting oxygen concentration in the flowing gas.

This result is significant because the glassy oxide forms and grows at low temperatures without direct observation in XRD and, at high temperature, a considerable amount of oxide is still amorphous. This is important for powder processing such as ball milling, since inadvertent oxygen exposure can cause oxidation that could go undetected if XRD is used to check the phase purity of the batch.

Figure 2.6 illustrates the proposed oxidation progression along with the La-Te binary phase diagram as a qualitative reference for the lanthanum telluride phases. A detailed discussion is provided in .543 (section .543 and Figure 0.2). It is noted that the oxidation progression has a kinetic component and late stages of oxidation can be achieved with longer heat treatments at lower temperature. Figure 0.3 demonstrates that oxidation to crystalline La_2O_2Te and Te is achieved after heat treatment at 400°C for 24 hours which is similar to the products at 600°C for

2 hours where Te is given off as vapor such that only La_2O_2Te is identified. The oxide is expected to grow slowly and remain amorphous at low temperature since evidence of oxidation is not detected in XRD for $La_{3-x}Te_4$ exposed to air for as long as 1 month (Figure 0.3). The higher-temperature heat treatments thus allow oxidation progression to be systematically studied in a shorter time frame.

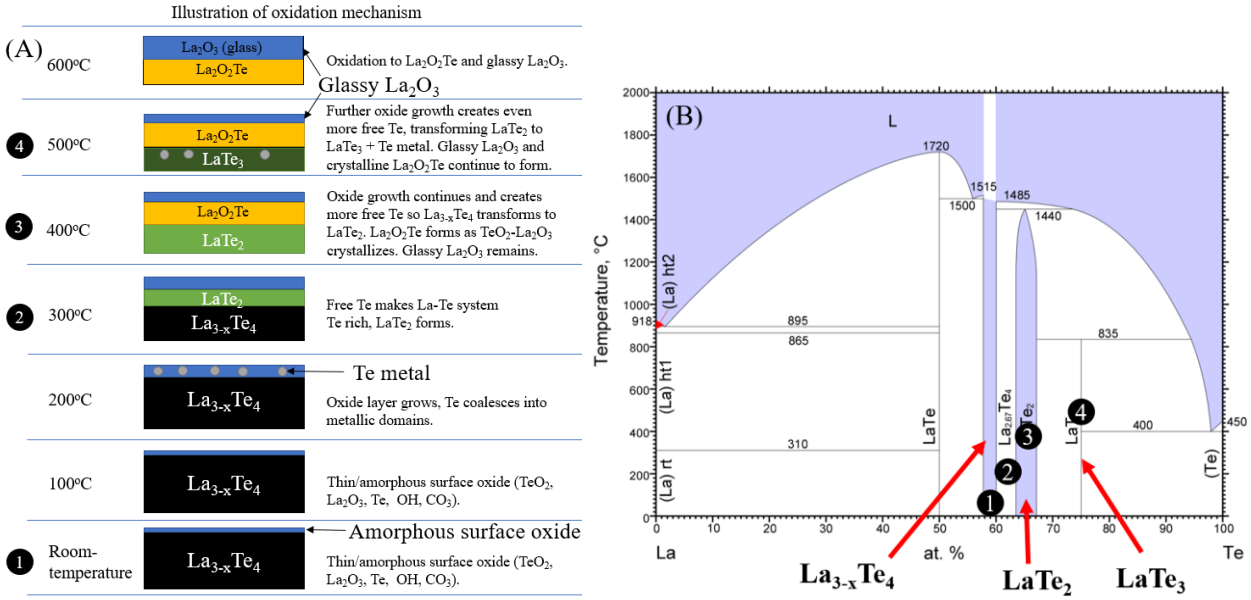

Figure 2.6. (A) Illustration of the temperature-dependent La3-xTe4 oxidation mechanism. (B) La-Te binary phase diagram (reprinted from ASM International Alloy Phase Diagram Database, Copyright 2006 [24]). Points 1-4 are used to qualitatively reference the oxidation mechanism to the phase diagram, and show how the formation of Te causes the bulk lanthanum telluride to become Te-rich. This leads to the formation of Te-rich phases as oxidation progresses.

The oxidation mechanism (Figure 2.6A and Figure 0.2) can be understood from the standpoint that oxidation of $La_{3-x}Te_4$ results in the formation of glassy La_2O_3 and elemental Te (Equation 0.2). Some of the Te eventually reacts with oxygen to form TeO_2 which subsequently joins La_2O_3 to form a glassy LaO_xTe_y phase ((Equation 0.3 and (Equation 0.4). It is apparent that the remaining elemental Te which does not react with oxygen is highly mobile and can coalesce into domains that are sufficiently large to be observed in XRD. It then incorporates into the bulk lanthanum telluride matrix, causing a change in composition ((Equation 0.5 and (Equation 0.10).

As oxidation progresses, more elemental Te is produced which, when it reacts with oxygen, grows the oxide layer and, when it incorporates into the bulk matrix, makes the lanthanum telluride composition increasingly Te-rich. This can be visualized as moving towards Te component on the phase diagram (Figure 2.6B). The bulk composition starts initially at $La_{3-x}Te_4$, moves to the two-phase region between $La_{3-x}Te_4$ and $LaTe_2$, followed by the single-phase $LaTe_2$ region, and finally to the $LaTe_3$ composition. During this oxidation progression, the starting stoichiometry of the bulk $La_{3-x}Te_4$ phase is not preserved even though there is remaining lanthanum telluride that is unreacted with oxygen. Table 2.2 shows a summary of the overall oxidation process.

Table 2.2. Summary of the stages of lanthanum telluride oxidation.

Stage of oxidation	**Phases**
Below 300ºC (initial)	Bulk: $La_{3-x}Te_4$ Surface: Te (elemental + metal), TeO_2-La_2O_3 glass (LaO_xTe_y)
300-400ºC (intermediate)	Bulk: $La_{3-x}Te_4$ and/or $LaTe_2$ Surface: Te (elemental + metal), TeO_2-La_2O_3 glass (LaO_xTe_y)
400ºC-500ºC (intermediate)	Bulk: $LaTe_2$ or $LaTe_3$ (+ Te) Surface: Te (elemental + metal), La_2O_2Te (crystalline), La_2O_3 (glass)
Above 500ºC (final)	Bulk: La_2O_2Te (crystalline) + La_2O_3 (glass)
Overall reaction	10 La_3Te_4 + 21 O_2 → 12 La_2O_3 (glass) + 3 La_2O_2Te (crystalline) + 37 Te (vapor)

The insidious nature of oxidation is two-fold since not only does deleterious La_2O_2Te form, but oxide growth also changes the composition of the underlying bulk which is harmful to the thermoelectric performance. The oxide phases are electrically insulating which drastically decreases the electronic conductivity of the material as oxidation progresses (Figure 0.4).[21] Furthermore, a change in composition of the underlying $La_{3-x}Te_4$ to Te-rich phases also makes the matrix highly resistive.[1,5] Both of these effects are detrimental since a decrease in electrical conductivity adversely affects *ZT*.

2.5 Thermodynamic Assessment of $La_{3-x}Te_4$ Oxidation

With an improved understanding of the oxide progression for $La_{3-x}Te_4$, a thermodynamic analysis was performed to supplement the experimental results and better understand the stability of the observed oxide phases. Of particular interest is the stability of $La_{3-x}Te_4$ relative to the oxide phases and the equilibrium partial pressure of oxygen for the oxidation reaction. Figure 2.7A shows the Materials Project calculated La-Te-O ternary phase diagram at 0K,[25–29] with the vertical direction showing the formation energy for each phase. A lower formation energy is associated with a more energetically favorable phase. Table 2.3 shows the formation energy for selected phases. La_3Te_4 has the lowest formation energy of the lanthanum telluride phases but is significantly higher than most of the oxide phases such as La_2O_2Te and La_2O_3. La_2O_3 is the most energetically favorable of the La-Te-O phases.

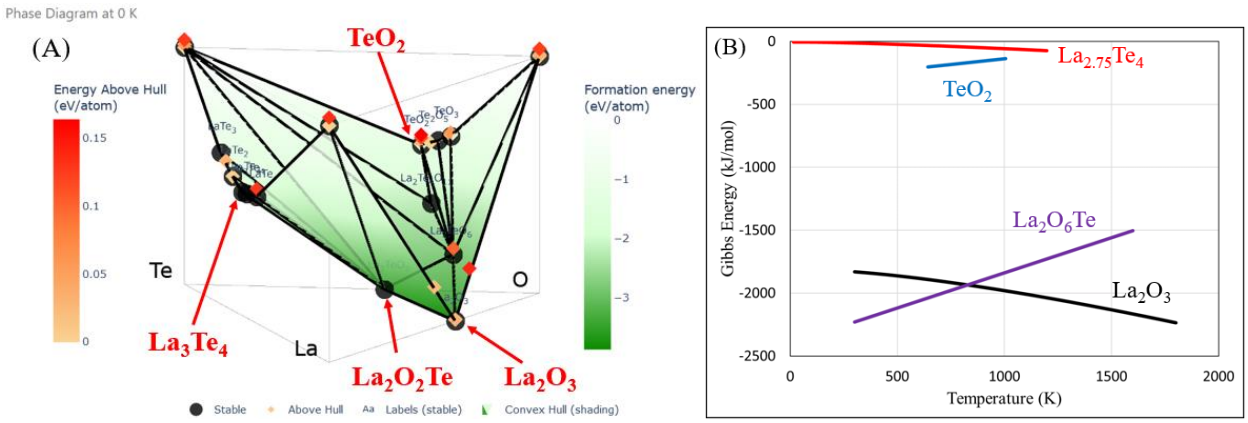

Figure 2.7. (A) La-Te-O ternary phase diagram at 0K, showing formation energy in the vertical direction (Reprinted from Materials Project Thermodynamic Stability Tool[25,27–29] with permission via Creative Commons Attribution 4.0 License. Jain *et al*, Commentary: The Materials Project: A materials genome approach to accelerating materials innovation, *APL Materials*, vol. 1 (1).[26] Copyright 2013.). (B) Calculated Gibbs energy vs. temperature for selected La-Te-O phases. There is a lack of literature data for La_2O_2Te, so data for La_2O_6Te is presented instead. $La_{2.75}Te_4$ data from Wang *et al*[30]. TeO_2 data from Aspiala *et al*[31]. La_2O_6Te data from Pankajavalli *et al*[32]. La_2O_3 data from Zinkevich *et al*[33]. The empirical relationships for TeO_2, La_2O_6Te, and La_2O_3 are shown in Table 2.4.

Table 2.3. Calculated formation energies at 0 K for select La-Te-O phases from Figure 2.7A (Materials Project [25]).

Phase	$LaTe_3$	$LaTe_2$	La_3Te_4	La_2O_2Te	La_2O_3	TeO_2
Formation Energy (kJ/mol)	-135	-162	-178	-327	-374	-144

Although lanthanum telluride oxidation is energetically favorable, formation energy alone does not adequately describe thermodynamic stability. Therefore, the Gibbs energy of formation ($\Delta G_f{}^o$) for selected La-Te-O phases was compared to provide better insight regarding their relative stabilities (Figure 2.7B). $\Delta G_f{}^o$ for $La_{2.75}Te_4$ was calculated using values for $\Delta H_f{}^o$ and ΔS^o from literature.[30] $\Delta G_f{}^o$ for TeO_2, La_2O_6Te, and La_2O_3 was calculated using empirical relationships from literature shown in Table 2.4 which were obtained from fits to experimental data. No literature could be found for La_2O_2Te thermodynamic values, so La_2O_6Te was included instead to represent a lanthanum oxytelluride phase due to the availability of thermodynamic data.

Table 2.4 Empirical relationships for standard Gibbs energy of formation used to obtain Figure 2.7B.

Phase (reference)	**Empirical relationship for standard Gibbs energy (from literature)**
TeO_2 ([31])	$\Delta G_f{}^o(\mathrm{kJ/mol}) = -317.09 + 0.180T$ (642K ≤ T < 722.15K) $\Delta G_f{}^o(\mathrm{kJ/mol}) = -317.09 + 0.180T$ (722.15K ≤ T < 1005.8K)
La_2O_6Te ([32])	$\Delta G_f{}^o(\mathrm{kJ/mol}) = -2394.4 + 0.5563T$
La_2O_3 ([33])	$\Delta G_f{}^o(\mathrm{kJ/mol}) = -1833.3 + 0.693T - 0.121Tln(T) - 6.85x10^{-3}T^2 + 808T^{-1} - 10^4T^{-2}$

In Figure 2.7B, the Gibbs energies of the oxide phases are much lower than $La_{2.75}Te_4$, particularly for lanthanum oxytelluride and lanthanum oxide. This demonstrates that the oxide phases are more thermodynamically stable than lanthanum telluride. At temperatures below ~800K, La_2O_6Te is more stable than La_2O_3 or TeO_2 which suggests that the amorphous surface oxide at lower temperatures likely exists as a glassy lanthanum oxytelluride phase (written as LaO_xTe_y since the exact stoichiometry may vary due to its amorphous nature). Upon heating to 400°C, the glassy oxide crystallizes to form La_2O_2Te which is observed in XRD. As the

temperature increases further, La_2O_3 becomes more thermodynamically favorable which promotes transformation of La_2O_2Te to La_2O_3. The co-existence of La_2O_2Te and glassy La_2O_3 may result from slow reaction kinetics of this transformation or the fact that oxygen is a limiting reagent due to its low concentration in the flowing gas.

Since lanthanum has a high affinity for oxygen, it is expected that the driving force for $La_{3-x}Te_4$ oxidation is ultimately reaction of La with oxygen to form La_2O_3:

$$2\ La\ (s) + 3/2\ O_2\ (g) \rightarrow La_2O_3\ (s) \qquad \text{(Equation 2.5)}$$

The equilibrium oxygen partial pressure describes the oxygen concentration at which the reaction in (Equation 2.5) is in equilibrium. The reactants (La and O_2) are favored below this concentration, and the product (La_2O_3) is favored above it. Figure 2.8 shows a stability diagram from the literature for La_2O_3, which represents the stable phases as a function of temperature and oxygen partial pressure (P_{O_2}) A practical method to prevent oxidation during processing or in service would be to maintain an environment with a low partial pressure of oxygen. However, as seen in Figure 2.8, the equilibrium oxygen partial pressure for (Equation 2.5 is extremely low – on the order of 10^{-50} bar at 1000ºC.[34] This partial pressure is very difficult to obtain and maintain, and demonstrates the thermodynamic favorability of $La_{3-x}Te_4$ oxidation during the tube furnace heat treatments. Figure 2.8 suggests that even the nominal oxygen content of ultra-high purity gas provided by Airgas (1ppm)[35] is thermodynamically sufficient for oxidation of $La_{3-x}Te_4$, though higher concentrations (100-1000ppm) are required for greater extents of oxidation. Additionally, the oxide phases are stable despite the presence of H_2 in the forming gas which demonstrates that H_2 is unable to mitigate oxidation by reducing the oxides. For most laboratory scale processing and service conditions, maintaining an oxygen partial pressure low enough to

minimize oxidation of La is extremely difficult and likely not likely not a practical alternative for processing this material into a thermoelectric couple.

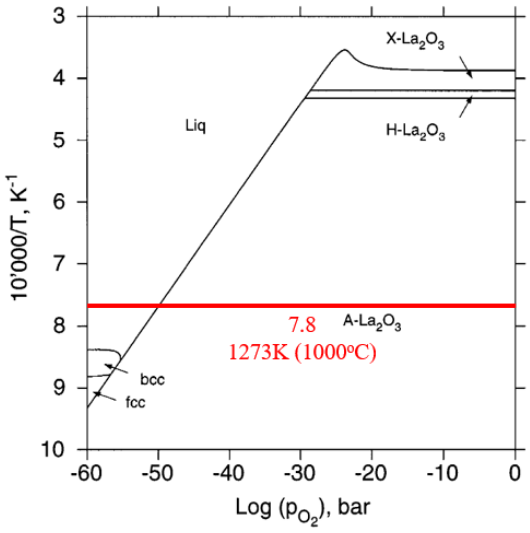

Figure 2.8. (Reprinted from Grundy *et al*. Thermodynamic Assessment of the Lanthanum-Oxygen System, *Journal of Phase Equilibria*, vol. 22 (2), 105-113[34]. Copyright 2001, Springer Nature.) Stability diagram for La_2O_3 as a function of temperature and oxygen partial pressure (P_{O_2}). The superimposed red line marks 1000°C to denote the expected processing/service temperature for $La_{3-x}Te_4$.

2.6 Discussion of Oxide Suppression Strategies for $La_{3-x}Te_4$

In light of the thermodynamic considerations, preventing oxidation of $La_{3-x}Te_4$ is nontrivial. Using fresh reactants and an inert atmosphere, avoiding extended time at high temperature, and post-processing oxide removal through polishing are necessary to mitigate oxidation during synthesis and processing of $La_{3-x}Te_4$.[8, 9, 10] This has been achieved in practice through meticulous handling of materials to minimize oxygen exposure, as well as replacing melt synthesis and conventional heat treatments with lower-temperature solid state techniques such as mechanochemical synthesis and spark plasma sintering.[8, 10, 11] $La_{3-x}Te_4$ synthesized using this diversified methodology is relatively free of oxide, though samples usually still contain a very small fraction of La_2O_2Te which does not affect the thermoelectric performance.[8, 11]

Mitigating oxidation in service conditions is more challenging due to the necessity of long-term exposure to high temperature, and research on this front is just beginning to emerge. As a first step, minimizing oxygen exposure is critical, and hermetically sealed chambers such as those developed for PbTe and BiTe thermoelectric devices can be used to maintain an inert atmosphere.[41, 42] Furthermore, maintaining a low oxygen partial pressure alone is insufficient due to the thermodynamic favorability of $La_{3-x}Te_4$ oxide formation at high temperature. A coating which acts as an oxygen diffusion barrier can add an extra measure to protect the underlying material and improve long-term reliability. This approach has been studied for Mg_2Si and skutterudite thermoelectric materials, in which oxide suppression above 500ºC has been demonstrated via the use of YSZ, enamel, silica aerogels, and composite glass coatings.[41, 43, 44]

Aerogel coatings have been proposed for thermal insulation and sublimation suppression in the design of $La_{3-x}Te_4$-based thermoelectric devices, though this concept has not yet been experimentally tested.[45] Materials-based methods to promote surface passivation are emerging as an effective strategy to slow the kinetics of oxide formation and its associated degradation. It has been observed that Ni- and Nb-based half-Heusler thermoelectrics form dense nickel stannide or niobium-rich layers at the surface when exposed to air at high temperature.[46] These layers act as a protective barrier and drastically slow the rate of oxidation.[46] A similar approach has shown promise with $La_{3-x}Te_4$-Ni composites.[12] The presence of Ni inclusions promotes the formation of a dense, well-adhered $La_2NiO_4/Ni_2Te_3O_8/NiO$ surface layer which seems to protect the underlying $La_{3-x}Te_4$ matrix from significant oxidation.[12] However, this layer does not offer complete protection as the electrical conductivity still suffers from long-term exposure to low partial pressures of oxygen (Figure 0.4).

Based on the preceding $La_{3-x}Te_4$ processing considerations and literature discussion, it is concluded that the best oxide-mitigation strategy for $La_{3-x}Te_4$ service conditions will take a multi-faceted approach in which a combination of multiple techniques is employed to manage the limitations of each individual strategy. A hermetic seal can help maintain the desired atmosphere, an oxide suppression coating can act as a diffusion barrier to further prevent oxygen exposure of the underlying material, and a composite that forms a passivating surface layer can slow or stop degradation should some oxygen exposure occur. Aerogel coatings, which have already been proposed for $La_{3-x}Te_4$ device design, could also potentially improve its oxidation resistance and should serve as the starting point for future studies into oxide suppression coatings. Additionally, $La_{3-x}Te_4$-Ni composites are already known to have superior thermoelectric performance to $La_{3-x}Te_4$ [9, 10], and the added potential for enhanced oxidation resistance[12] makes the composite even more promising for device fabrication. More research into the oxidation behavior of this composite needs to be done to achieve complete protection and inform other composite materials which may exhibit improved oxidation resistance.

2.7 Summary and Conclusions

Oxidation of $La_{3-x}Te_4$ powder was studied to develop a better understanding of the mechanisms by which thermoelectric properties degrade. As-synthesized $La_{3-x}Te_4$ powder contains a surface oxide consisting of an amorphous TeO_2-La_2O_3 lanthanum oxytelluride phase (LaO_xTe_y), elemental Te, and surface hydroxyl and carbonate species. The presence of this surface oxide does not preclude the synthesis of dense, high-*ZT* $La_{3-x}Te_4$ which suggests that the native surface oxide is not detrimental to thermoelectric performance in small amounts.[8] However, the surface oxide can become significant enough over time, even in inert storage conditions, such that densification is eventually inhibited.[11] As oxidation progresses, the

amorphous surface oxide grows, creating additional Te which is highly mobile and coalesces into domains of metallic Te which eventually incorporate into the bulk lanthanum telluride. Additionally, the amorphous LaO_xTe_y phase crystallizes to La_2O_2Te at 400ºC.

The thermoelectric properties degrade by simultaneous formation of electrically resistive oxide phases such as La_2O_2Te and electrically resistive Te-rich lanthanum telluride phases. Since the oxide is non-passivating, the remaining lanthanum telluride eventually reacts with oxygen which results in transformation of the bulk to La_2O_2Te and glassy La_2O_3. These results are significant since they show that oxidation is not only detrimental because of the formation of a brittle, electrically resistive oxide, but also because extended oxidation changes the bulk $La_{3-x}Te_4$ composition. Both effects are harmful to thermoelectric performance. Therefore, $La_{3-x}Te_4$ samples with minimal oxide need to be prepared through careful handling and processing.

The next step for $La_{3-x}Te_4$ device manufacturing is to address oxidation under service conditions. The main challenge is avoiding oxidation during prolonged exposure to high temperatures since oxide formation is thermodynamically favorable. Aerogels, which have already been proposed as a thermal and sublimation coating for $La_{3-x}Te_4$ devices[45], have been shown to improve the oxidation resistance of skutterudites[41, 44] and could have similar benefits for $La_{3-x}Te_4$. $La_{3-x}Te_4$-Ni composites show encouraging initial results for oxidation resistance via passivation[12] and provide the basis for materials-based strategies in this regard. Future research should focus on developing a multi-faceted approach in which oxygen exposure is minimized through device design, protective coatings which act as oxygen barriers, and composites to form passivating surface layers that slow or stop oxidation if exposure occurs.

2.8 References

(1) Rinehart, G. H. Design Characteristics and Fabrication of Radioisotope Heat Sources for Space Missions. *Progress in Nuclear Energy* **2001**, *39* (3–4), 305–319. https://doi.org/10.1016/S0149-1970(01)00005-1.

(2) Fleurial, J. P. Thermoelectric Power Generation Materials: Technology and Application Opportunities. *JOM* **2009**, *61* (4), 79–85. https://doi.org/10.1007/S11837-009-0057-Z/METRICS.

(3) Cook, B. Silicon-Germanium: The Legacy Lives On. *Energies (Basel)* **2022**, *15* (8), 2957.

(4) Tritt, T. M.; Subramanian, M. A. Thermoelectric Materials, Phenomena, and Applications: A Bird's Eye View. *MRS Bull* **2006**, *31* (3), 188–194. https://doi.org/10.1557/MRS2006.44/METRICS.

(5) Ma, J. M.; Clarke, S. M.; Zeier, W. G.; Vo, T.; Von Allmen, P.; Jeffrey Snyder, G.; Kaner, R. B.; Fleurial, J. P.; Bux, S. K. Mechanochemical Synthesis and High Temperature Thermoelectric Properties of Calcium-Doped Lanthanum Telluride La3−xCaxTe4. *J Mater Chem C Mater* **2015**, *3* (40), 10459–10466. https://doi.org/10.1039/C5TC01648G.

(6) Cheikh, D.; Hogan, B. E.; Vo, T.; Von Allmen, P.; Lee, K.; Smiadak, D. M.; Zevalkink, A.; Dunn, B. S.; Fleurial, J. P.; Bux, S. K. Praseodymium Telluride: A High-Temperature, High-ZT Thermoelectric Material. *Joule* **2018**, *2* (4), 698–709. https://doi.org/10.1016/J.JOULE.2018.01.013.

(7) Bennett, G. L. Space Nuclear Power. *Encyclopedia of Physical Science and Technology* **2003**, 537–553. https://doi.org/10.1016/B0-12-227410-5/00715-8.

(8) May, A. F.; Fleurial, J. P.; Snyder, G. J. Thermoelectric Performance of Lanthanum Telluride Produced via Mechanical Alloying. *Phys Rev B Condens Matter Mater Phys* **2008**, *78* (12), 125205. https://doi.org/10.1103/PHYSREVB.78.125205/FIGURES/11/MEDIUM.

(9) Ma, J. Improving the Mechanical Strength and Power Conversion Efficiency of High Temperature Thermoelectrics, UCLA, Los Angeles, 2014.

(10) Cheikh, D. Synthesis and Characterization of Rare-Earth Tellurides and Their Composites for High-Temperature Thermoelectric Applications, UCLA, Los Angeles, 2017.

(11) May, A. High-Temperature Transport in Lanthanum Telluride and Other Modern Thermoelectric Materials, California Institute of Technology, Pasadena, 2010.

(12) Li, J.; Liu, R.; Song, Q.; Gao, Z.; Huang, H.; Zhang, Q.; Shi, X.; Bai, S.; Chen, L. Enhanced Thermal Stability and Oxidation Resistance in La3-XTe4 by Compositing Metallic Nickel Particles. *Acta Mater* **2022**, *224*, 117526. https://doi.org/10.1016/J.ACTAMAT.2021.117526.

(13) *Lanthanum | XPS Periodic Table | Thermo Fisher Scientific - US*. https://www.thermofisher.com/us/en/home/materials-science/learning-center/periodic-table/lanthanide-rare-earth/lanthanum.html (accessed 2023-03-06).

(14) *Tellurium | Periodic Table | Thermo Fisher Scientific - US*. https://www.thermofisher.com/us/en/home/materials-science/learning-center/periodic-table/metalloid/tellurium.html (accessed 2023-03-06).

(15) Samal, A. K.; Pradeep, T. Pt3Te4 Nanoparticles from Tellurium Nanowires. *Langmuir* **2010**, *26* (24), 19136–19141. https://doi.org/10.1021/LA103466J/SUPPL_FILE/LA103466J_SI_001.PDF.

(16) Kong, H.; Yeo, J. Bin; Lee, H. Y. A Study on the Properties of Tellurium-Oxide Thin Films Based on the Variable Sputtering Gas Ratio. *Journal of the Korean Physical Society* **2015**, *66* (11), 1744–1749. https://doi.org/10.3938/JKPS.66.1744/METRICS.

(17) Samal, A. K.; Pradeep, T. Lanthanum Telluride Nanowires: Formation, Doping, and Raman Studies. *Journal of Physical Chemistry C* **2010**, *114* (13), 5871–5878. https://doi.org/10.1021/JP911658K/SUPPL_FILE/JP911658K_SI_001.PDF.

(18) *Oxygen | XPS Periodic Table | Thermo Fisher Scientific - US*. https://www.thermofisher.com/us/en/home/materials-science/learning-center/periodic-table/non-metal/oxygen.html (accessed 2023-03-06).

(19) Li, J. P. H.; Zhou, X.; Pang, Y.; Zhu, L.; Vovk, E. I.; Cong, L.; Van Bavel, A. P.; Li, S.; Yang, Y. Understanding of Binding Energy Calibration in XPS of Lanthanum Oxide by in Situ Treatment. *Physical Chemistry Chemical Physics* **2019**, *21* (40), 22351–22358. https://doi.org/10.1039/C9CP04187G.

(20) Fleming, P.; Farrell, R. A.; Holmes, J. D.; Morris, M. A. The Rapid Formation of La(OH)3 from La2O3 Powders on Exposureto Water Vapor. *Journal of the American Ceramic Society* **2010**, *93* (4), 1187–1194. https://doi.org/10.1111/J.1551-2916.2009.03564.X.

(21) *Carbon | XPS Periodic Table | Thermo Fisher Scientific - US*. https://www.thermofisher.com/us/en/home/materials-science/learning-center/periodic-table/non-metal/carbon.html (accessed 2023-03-06).

(22) Kotina, I. M.; Tukhkonen, L. M.; Patsekina, G. V.; Shchukarev, A. V.; Gusinskii, G. M. Study of CdTe Etching Process in Alcoholic Solutions of Bromine. *Semicond Sci Technol* **1998**, *13* (8), 890. https://doi.org/10.1088/0268-1242/13/8/011.

(23) Neudachina, V. S.; Shatalova, T. B.; Shtanov, V. I.; Yashina, L. V.; Zyubina, T. S.; Tamm, M. E.; Kobeleva, S. P. XPS Study of SnTe(1 0 0) Oxidation by Molecular Oxygen. *Surf Sci* **2005**, *584* (1), 77–82. https://doi.org/10.1016/J.SUSC.2005.01.061.

(24) Badrinarayanan, S.; Mandale, A. B.; Sinha, A. P. B. Photoelectron Spectroscopy Study of Surface Oxidation of SnTe PbTe and PbSnTe. *Mater Chem Phys* **1984**, *11* (1), 1–14. https://doi.org/10.1016/0254-0584(84)90084-1.

(25) Berchenko, N.; Vitchev, R.; Trzyna, M.; Wojnarowska-Nowak, R.; Szczerbakow, A.; Badyla, A.; Cebulski, J.; Story, T. Surface Oxidation of SnTe Topological Crystalline Insulator. *Appl Surf Sci* **2018**, *452*, 134–140. https://doi.org/10.1016/J.APSUSC.2018.04.246.

(26) Miller, D. J.; Biesinger, M. C.; McIntyre, N. S. Interactions of CO2 and CO at Fractional Atmosphere Pressures with Iron and Iron Oxide Surfaces: One Possible Mechanism for Surface Contamination? *Surface and Interface Analysis* **2002**, *33* (4), 299–305. https://doi.org/10.1002/SIA.1188.

(27) Faznny, M. F.; Halimah, M. K.; Azlan, M. N. EFFECT OF LANTHANUM OXIDE ON OPTICAL PROPERTIES OF ZINC BOROTELLURITE GLASS SYSTEM. *Journal of Optoelectronics and Biomedical Materials 8* (2), 49–59.

(28) Gupta, G.; Balaji, S.; Biswas, K.; Kalyandurg, A. Mid-IR Transparent TeO2-TiO2-La2O3 Glass and Its Crystallization Behavior for Photonic Applications. *Journal of the American Ceramic Society* **2018**, *101* (9), 3900–3916. https://doi.org/10.1111/JACE.15558.

(29) *La-Te Binary Phase Diagram (1990 Okamoto H.)*. ASM Alloy Phase Diagram Database. https://matdata.asminternational.org/apd/viewPicture.aspx?dbKey=grantami_apd&id=10713366&revision=399310# (accessed 2023-03-06).

(30) *mp-4547: La2TeO2 (Tetragonal, I4/mmm, 139)*. https://materialsproject.org/materials/mp-4547 (accessed 2023-03-06).

(31) Jain, A.; Ong, S. P.; Hautier, G.; Chen, W.; Richards, W. D.; Dacek, S.; Cholia, S.; Gunter, D.; Skinner, D.; Ceder, G.; Persson, K. A. Commentary: The Materials Project: A Materials Genome Approach to Accelerating Materials Innovation. *APL Mater* **2013**, *1* (1), 011002. https://doi.org/10.1063/1.4812323.

(32) Jain, A.; Hautier, G.; Ong, S. P.; Moore, C. J.; Fischer, C. C.; Persson, K. A.; Ceder, G. Formation Enthalpies by Mixing GGA and GGA + U Calculations. *Phys Rev B Condens Matter Mater Phys* **2011**, *84* (4), 045115. https://doi.org/10.1103/PHYSREVB.84.045115/FIGURES/5/MEDIUM.

(33) Wang, A.; Kingsbury, R.; Mcdermott, M.; Horton, M.; Jain, A.; Ong, S. P.; Dwaraknath, S.; Persson, K. A. A Framework for Quantifying Uncertainty in DFT Energy Corrections. **2021**. https://doi.org/10.26434/CHEMRXIV.14593476.V1.

(34) Aykol, M.; Dwaraknath, S. S.; Sun, W.; Persson, K. A. Thermodynamic Limit for Synthesis of Metastable Inorganic Materials. *Sci Adv* **2018**, *4* (4). https://doi.org/10.1126/SCIADV.AAQ0148/SUPPL_FILE/AAQ0148_SM.PDF.

(35) Wang, Y.; Hu, Y. J.; Chong, X.; Palma, J. P. S.; Firdosy, S. A.; Star, K. E.; Fleurial, J. P.; Ravi, V. A.; Shang, S. L.; Chen, L. Q.; Liu, Z. K. Quasiharmonic Calculations of Thermodynamic Properties for La3−xTe4 System. *Comput Mater Sci* **2018**, *142*, 417–426. https://doi.org/10.1016/J.COMMATSCI.2017.10.036.

(36) Aspiala, M.; Sukhomlinov, D.; Taskinen, P. Standard Gibbs Energy of Formation of Tellurium Dioxide Measurement by a Solid-Oxide Electrolyte EMF Technique. *Thermochim Acta* **2013**, *573*, 95–100. https://doi.org/10.1016/J.TCA.2013.08.006.

(37) Pankajavalli, R.; Jain, A.; Babu, R.; Ananthasivan, K.; Anthonysamy, S.; Ganesan, V. Thermodynamic Characterization of Lanthanum Tellurate. *Journal of Nuclear Materials* **2010**, *397* (1–3), 116–121. https://doi.org/10.1016/J.JNUCMAT.2009.12.017.

(38) Zinkevich, M. Thermodynamics of Rare Earth Sesquioxides. *Prog Mater Sci* **2007**, *52* (4), 597–647. https://doi.org/10.1016/J.PMATSCI.2006.09.002.

(39) Grundy, A. N.; Hallstedt, B.; Gauckler, L. J. Thermodynamic Assessment of the Lanthanum-Oxygen System. *Journal of Phase Equilibria* **2001**, *22* (2), 105–113. https://doi.org/10.1361/105497101770338950/METRICS.

(40) *Airgas Product Catalog*. https://www.airgas.com/airgascatalog/catalog/index.html (accessed 2023-03-06).

(41) Park, S. H.; Kim, Y.; Yoo, C. Y. Oxidation Suppression Characteristics of the YSZ Coating on Mg2Si Thermoelectric Legs. *Ceram Int* **2016**, *42* (8), 10279–10288. https://doi.org/10.1016/J.CERAMINT.2016.03.161.

(42) Kambe, M.; Jinushi, T.; Ishijima, Z. Encapsulated Thermoelectric Modules for Advanced Thermoelectric Systems. *J Electron Mater* **2014**, *43* (6), 1959–1965. https://doi.org/10.1007/S11664-013-2926-Z/METRICS.

(43) Park, Y. S.; Thompson, T.; Kim, Y.; Salvador, J. R.; Sakamoto, J. S. Protective Enamel Coating for N- and p-Type Skutterudite Thermoelectric Materials. *J Mater Sci* **2015**, *50* (3), 1500–1512. https://doi.org/10.1007/S10853-014-8711-4/METRICS.

(44) Dong, H.; Li, X.; Huang, X.; Zhou, Y.; Jiang, W.; Chen, L. Improved Oxidation Resistance of Thermoelectric Skutterudites Coated with Composite Glass. *Ceram Int* **2013**, *39* (4), 4551–4557. https://doi.org/10.1016/J.CERAMINT.2012.11.051.

(45) Fleurial, J.-P.; Johnson, K.; Mondt, J.; Sakamoto, J.; Snyder, J.; Chen-Kuo Huang; Blair, R.; Stapfer, G.; Caillat, T.; Frye, P.; Determan, W.; Heshmatpour, B.; Brooks, M.; Tuttle, K. Development of Segmented Thermoelectric Multicouple Converter Technology. *2006 IEEE Aerospace Conference* 1–10. https://doi.org/10.1109/AERO.2006.1656006.

(46) Kang, H. B.; Saparamadu, U.; Nozariasbmarz, A.; Li, W.; Zhu, H.; Poudel, B.; Priya, S. Understanding Oxidation Resistance of Half-Heusler Alloys for in-Air High Temperature Sustainable Thermoelectric Generators. *ACS Appl Mater Interfaces* **2020**, *12* (32), 36706–36714. https://doi.org/10.1021/ACSAMI.0C08413/SUPPL_FILE/AM0C08413_SI_001.PDF.

Chapter 3 Electrophoretic Deposition (EPD) of $La_{3-x}Te_4$ Films

3.1 Introduction and Motivation for Thin Film Synthesis

Synthesis of thermoelectric thin films has generated community interest in recent years as a possible route to improve thermoelectric performance compared to bulk materials as well as expand device architectures and reduce manufacturing costs, device weight, and size.[1,2] Thin film structures can decouple electronic and thermal properties such that lattice thermal conductivity is decreased without sacrificing electronic conductivity, leading to an increase in ZT.[1–5] For instance, reduced dimensionality of the material and incorporation of nano-scale features can enhance phonon scattering independently of electron scattering as well as provide desirable electronic states for improved electronic conductivity and Seebeck coefficient.[1,2,4–7] Additionally, the film-substrate interface may exhibit scattering and grain growth effects which further influence thermoelectric properties.[2] The potential for these thin film enhancements to thermoelectric properties is directly applicable to $La_{3-x}Te_4$ since the existence of nano-scale features such as La vacancies and Ni nanoparticle inclusions have already been demonstrated to reduce the lattice thermal conductivity of $La_{3-x}Te_4$ through enhanced phonon scattering.[8–10]

From a device manufacturing perspective, thin film synthesis techniques also provide added processing flexibility compared to typical bulk synthesis. Thermoelectric thin films have lower weight and size than their bulk counterparts which can improve device specific power, and thin films can take advantage of improved mechanical properties imparted by the substrate.[2,11] In the case of $La_{3-x}Te_4$-Ni composites, deposition on Ni substrates with different structures provides a potential processing route for studying the effect of Ni inclusion morphology on thermoelectric properties.[10] There are also a wide variety of processing techniques available for thin film synthesis such as chemical vapor deposition (CVD), physical vapor deposition (PVD), molecular

beam epitaxy (MBE), vapor-liquid-solid (VLS) growth, hydrothermal processing, pulsed laser deposition, and electrodeposition.[2,6,11–13]

Though many of the listed techniques are capable of producing high-performance thermoelectric thin films for fundamental study [2], they are generally expensive, complex, energy-intensive, and low throughput. These factors are disadvantageous for device fabrication in which a simple, inexpensive, and high-throughput processing scheme is desirable for practicality. For these reasons, electrodeposition, which encompasses electroplating and electrophoretic deposition (EPD), is an attractive technique for thin film synthesis due to its room-temperature operation, simple/low-energy setup, high deposition rates, and good scalability.[6,11,12]

Electroplating has been widely studied for synthesis of common thermoelectric thin films such as Bi_2Te_3 [6,12], but its application to $La_{3-x}Te_4$ is doubtful due to the complexities of rare-earth electrochemistry. Further research is necessary to achieve deposition of La metal without significant oxidation or electrolyte contamination.[14–16] By contrast, EPD is performed using starting powder of the material which, for $La_{3-x}Te_4$, avoids the limitations of rare-earth electroplating. Furthermore, EPD has garnered attention in recent years for fabrication of SiGe, Bi_2Te_3, and oxide thermoelectric thin films owing to its simplicity, reproducibility, and high deposition rates.[11,17–19] These qualities make EPD a good candidate for $La_{3-x}Te_4$ thin film synthesis.

3.2 Background and Theory of Electrophoretic Deposition (EPD)

During electrophoretic deposition (Figure 3.1), a coating is produced on a substrate by application of a voltage between two electrodes that are immersed in a colloidal suspension containing solid particles of the coating material. A key component of EPD is that, when suspended in the solvent, the solid particles develop a surface charge which causes their

migration and deposition under the influence of an applied electric field.[20,21] Since particles will deposit on the oppositely charged electrode, the sign of the surface charge dictates whether anodic EPD (deposition on the positive electrode) or cathodic EPD (deposition on the negative electrode) occurs.[20] A stable suspension is required for EPD since the particles must stay suspended uniformly in the solvent long enough to migrate and deposit on the substrate. The properties of the suspension, including surface charge, are therefore integral to EPD and control the rate, uniformity, and quality of deposition.

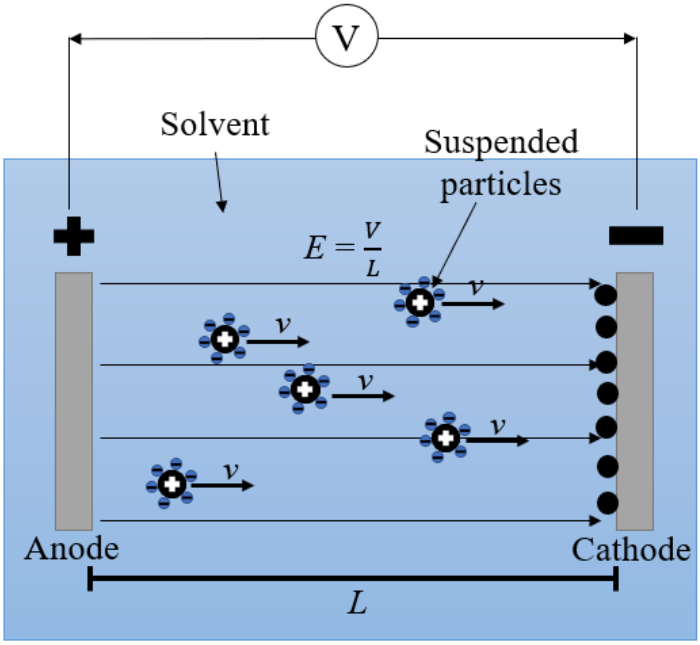

Figure 3.1: Illustration of the EPD process. This example shows cathodic EPD in which the particles develop a positive surface charge when suspended in the solvent. Application of a voltage between the electrodes causes particle migration towards and deposition on the oppositely charged cathode. Negative counterions from the solvent surround the positively charged particles.

Figure 3.2 demonstrates surface charge development on a solid particle suspended in a liquid solvent. Interaction at the particle/solvent interface can lead to surface charge by a number of proposed mechanisms such as selective adsorption of ions from the solvent onto the particle, dissociation of ions from the particle into the solvent, adsorption or orientation of solvent molecules on the particle surface, or electron transfer between the particle and solvent.[20,21] An

electrical double layer results from the particle's surface charge and consists of a tightly-bound layer of counter-ions at the particle surface surrounded by a diffuse layer of counter-ions.[20,22] Since suspension stability is largely dictated by the interaction and overlap of particles' diffuse layers, the potential at the diffuse layer is a significant parameter used to characterize EPD suspensions.[20,21] This potential is defined as the zeta potential (ζ).

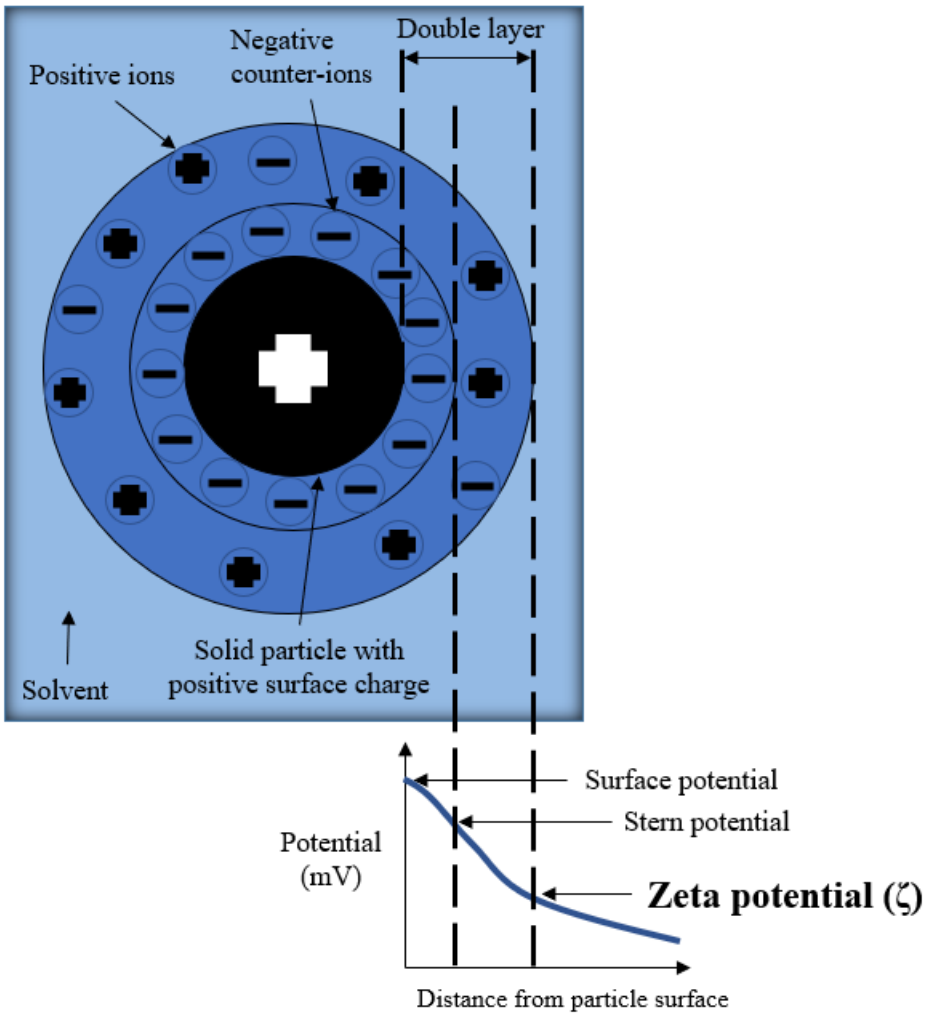

Figure 3.2: Illustration of surface charge development at the particle/solvent interface for a solid particle suspended in a liquid solvent. The change in potential across the electrical double layer surrounding the particle and the definition of zeta potential are shown.

Suspension stability for EPD is often defined in the literature within the framework of Derjaguin–Landau–Verwey–Overbeek (DLVO) theory which states that the primary forces

acting on suspended particles are van der Waals attraction between the particles and electrostatic or ionic repulsion between their double layers.[11,20,22] The van der Waals attraction is a driving force for particle agglomeration and destabilizes the suspension. The double layer repulsion opposes van der Waals attraction and counteracts agglomeration, resulting in stabilization of the suspension. Therefore, greater double layer repulsion (i.e. higher zeta potential) is associated with higher suspension stability and improved EPD deposit quality since greater repulsion prevents particle agglomeration and promotes uniform distribution of particles on the substrate during deposition.[19–22] Generally, suspensions with $|\zeta| \geq 30$ mV are considered to possess good stability for EPD.[23,24]

In addition to describing suspension stability and deposit quality, zeta potential is related to the velocity of particles under an applied electric field, a quantity known as the electrophoretic mobility (μ). The relationship between electrophoretic mobility and zeta potential is defined by the Smoluchowski equation (Equation 3.1) [21,25–27], and electrophoretic mobility is defined as the ratio of the particle velocity to the applied electric field (Equation 3.2):

$$\mu = \zeta \frac{\varepsilon_r \varepsilon_0}{4\pi\eta} \qquad \text{(Equation 3.1)}$$

$$\mu = \frac{v}{E} \qquad \text{(Equation 3.2)}$$

where μ is the electrophoretic mobility, ζ is the zeta potential, ε_r is the dielectric constant of the solvent, ε_o is the vacuum permittivity = 8.85 x 10^{-12} F/m, η is the solvent viscosity, v is the particle velocity, and E is the applied electric field.

Along with other applied deposition parameters, electrophoretic mobility quantifies the deposition rate as described by the Hamaker equation which relates deposited mass to EPD parameters[20,21]:

$$m = \int \mu \cdot E \cdot A \cdot C \cdot dt \qquad \text{(Equation 3.3)}$$

where m is the deposited mass, μ is the electrophoretic mobility, E is the applied electric field, A is the area of the substrate, C is the powder concentration, and t is the deposition time.

Assuming that the applied deposition parameters (E, A, C, and t) are constant, (Equation 3.3 predicts an increase in deposited mass with increasing electrophoretic mobility due to the larger particle velocity (Equation 3.2). Both solvent properties (viscosity and dielectric constant) and zeta potential can affect electrophoretic mobility (Equation 3.1). If the solvent viscosity and dielectric constant do not change, then an increase in zeta potential leads to an increase in electrophoretic mobility. Therefore, zeta potential is an important factor in determining deposition kinetics in addition to suspension stability and deposit quality.

An additional factor which affects EPD is the suspension conductivity. If the suspension conductivity is too high, then the electrophoretic mobility is low due to a lower electric field driving force caused by a reduced potential drop over the suspension.[20] If the suspension conductivity is too low, then the stability of the suspension can be compromised due to electronic charging of the particles.[20] As a result, there is typically a narrow conductivity range over which EPD occurs, though this range is usually at low overall conductivity values.[11,20] The dielectric constant of the solvent can play an important role in determining suspension conductivity since a higher dielectric constant indicates a higher dissociating power.[20,21] Solvents with higher dielectric constants generally produce suspensions with both higher surface charge and higher conductivity.[20]

The primary focus of EPD is thus finding an appropriate solvent which produces a suspension with the most beneficial properties for EPD. Organic solvents are most commonly used since they avoid hydrogen evolution and Joule heating that occur at high voltages in

aqueous suspensions.[20,21] For nonaqueous suspensions, a high zeta potential and electrophoretic mobility, moderate dielectric constant, and low suspension conductivity generally provide a favorable combination of properties that are conducive for EPD. In the literature, an emphasis is often placed on maximizing zeta potential, and therefore deposited mass, due to its importance in determining suspension stability and deposition quality.

3.3 Practical Considerations for EPD – Advantages and Disadvantages for $La_{3-x}Te_4$

The main advantages of EPD are its simplicity, high deposition rate, low cost, ability to deposit on effectively any conducting substrate, ability to deposit on complex geometries, and applicability to any material that can be made into a powder.[21] These properties are specifically advantageous for fabrication of $La_{3-x}Te_4$ thin films since they provide a practical, flexible, and scalable processing route. Mechanochemical synthesis of $La_{3-x}Te_4$ powder in the correct stoichiometry is well-established[28] and provides an ideal starting material for EPD. Furthermore, this stoichiometry, which is critical for thermoelectric performance, is not altered during EPD. Additionally, the use of organic solvents avoids aqueous processing which would oxidize $La_{3-x}Te_4$ and compromise its thermoelectric performance.

The primary disadvantages of EPD are that 1) finding an appropriate solvent for high-quality deposition is often non-trivial and 2) deposits, by nature, are a weakly bonded, porous powder which is not ideal for high electronic conductivity.[20] Solvent selection can be informed by choosing a solvent with the desirable combination of properties as described in section 3.2. The solvent selection criteria for $La_{3-x}Te_4$ are discussed in section 3.4. Post deposition sintering is required to increase film density and improve bonding, cohesiveness, and mechanical and electrical properties. For $La_{3-x}Te_4$, this necessitates careful selection of substrate materials and

heat treatment conditions to avoid cracking, oxidation, and reaction with the substrate. Sintering of $La_{3-x}Te_4$ EPD films is discussed in Chapter 4.

3.4 EPD of Thermoelectric Materials in the Literature and Selection of THF as Solvent

EPD of thermoelectric films has recently been reported in the literature through fabrication of SiGe[18] and Bi_2Te_3[11] films. After post-deposition heat treatments, both films achieved decent thermoelectric performance as determined by measurements of thermoelectric power factor ($S^2\sigma$) of 1.9 mW/m·K^2 for SiGe and Seebeck coefficient (S) of 126 μV/K for Bi_2Te_3.[11,18] Additionally, for Bi_2Te_3 films, Talebi *et al* performed a detailed study of various organic solvents and characterized the suspension properties that led to the highest deposition quality.[11] It was determined that Bi_2Te_3 suspended in tetrahydrofuran (THF) achieved the best green density of Bi_2Te_3 coatings with highest uniformity, thickness, and area coverage of the substrate due to the high values of zeta potential (62 mV) and electrophoretic mobility and low suspension conductivity.[11] Motivated by this desirable combination of suspension properties and demonstration of high-quality EPD results for Bi_2Te_3, we selected THF as the solvent for EPD of $La_{3-x}Te_4$ in the present work. It will be shown that $La_{3-x}Te_4$/THF suspensions possess a similarly high value of zeta potential due to effective surface charge development which leads to high-quality $La_{3-x}Te_4$ deposits.

3.5 Experimental Methods

$La_{3-x}Te_4$ powder was synthesized using established mechanochemical methods.[28] Briefly, elemental La and Te were combined in stoichiometric amounts and ball milled to achieve the alloyed powder. The elemental reactants were handled in an Ar-filled glovebox and the ball mill vial was sealed under Ar. The resulting as-synthesized $La_{3-x}Te_4$ powder was used without further treatment.

Tetrahydrofuran (THF) (anhydrous, 99.8+% AcroSeal under Ar, obtained from Alfa Aesar) was used as the solvent for EPD experiments without further treatment. All materials and chemicals were handled in an Ar-filled glovebox to avoid oxygen and moisture exposure. $La_{3-x}Te_4$/THF suspensions were prepared by suspending $La_{3-x}Te_4$ powder in THF at a concentration of 10 mg/mL followed by sonication or magnetic stirring for at least 10 minutes to uniformly disperse the powder. EPD was performed immediately after sonication/stirring ceased. Constant voltage was applied between two parallel electrodes immersed in the suspension using a Keithley 228A programmable voltage/current source. Deposition voltage and time were 100 V and 10 minutes, respectively. Deposition occurred on the cathode (negative electrode) which served as the substrate material. The variety of substrate materials are listed in Table 3.1. The counter/positive electrode (anode) was Ni foil in all cases. Since boron nitride (BN) is electrically insulating, deposition was achieved by attaching Ni mesh to the side facing the counter electrode to facilitate electric field development.

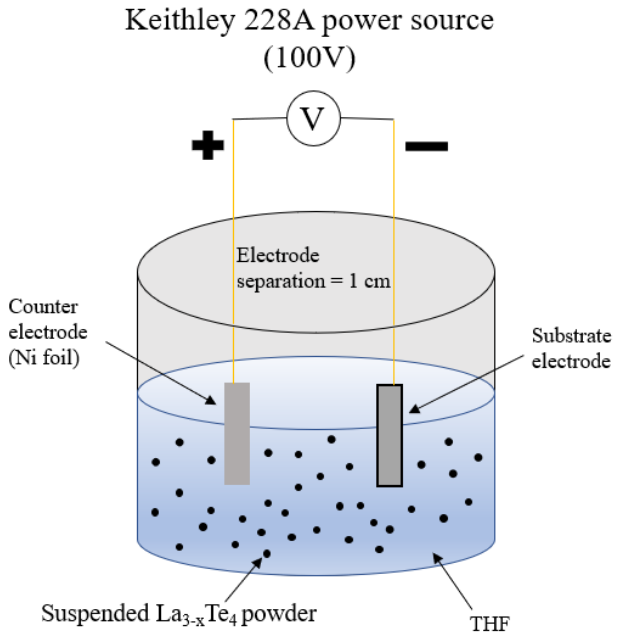

Figure 3.3: Illustration of the experimental setup for EPD of $La_{3-x}Te_4$. As-synthesized $La_{3-x}Te_4$ powder was suspended in THF at 10 mg/mL. Cathodic EPD was performed at 100V for 10 minutes.

Table 3.1: Description of substrates (cathodes) used for EPD of $La_{3-x}Te_4$.

Planar substrates	Ni foil, grafoil, BN plate, Cu foil, Mo foil
Non-planar substrates	Cu wire, Ni mesh, Ni foam

3.6 EPD of $La_{3-x}Te_4$ on Planar Substrates

Figure 3.4 shows photos and SEM images for $La_{3-x}Te_4$ deposited on various foil substrates (Ni foil, grafoil, BN, Cu foil, and Mo foil). The $La_{3-x}Te_4$ coating is visible as a grey film on the lower half of the substrate with 100% coverage of the immersed area. For all substrate materials, SEM images show the deposited $La_{3-x}Te_4$ film is uniform with no cracking or exposed substrate. The microstructure is independent of the substrate, with the films being composed of nanometer to micron-sized subangular particles and having a porosity between 30-35% (calculated by ImageJ area analysis). Cross-sectional SEM of $La_{3-x}Te_4$ on Ni (Figure 3.5K) indicates that the film is between 10-15 μm thick. The films have the same morphology as the starting powder (Figure 3.4L), though the starting powder has large agglomerates which are absent in the EPD films. The lack of agglomeration in the EPD films provides evidence of good particle repulsion and highlights the excellent dispersion of $La_{3-x}Te_4$ powder in THF. Additionally, cathodic deposition indicates that $La_{3-x}Te_4$ particles have a positive surface charge when suspended in THF. XRD scans (Figure 3.5) show that the films are phase-pure $La_{3-x}Te_4$, and EDX analysis (Figure 3.5) confirms La and Te in the correct atomic percentages (between 57-60 at% Te) with a calculated value of $x = 0.25$. This is within error of the optimized value of $x = 0.23$ [28–30] and indicates EPD does not detectably alter the stoichiometry of the starting powder.

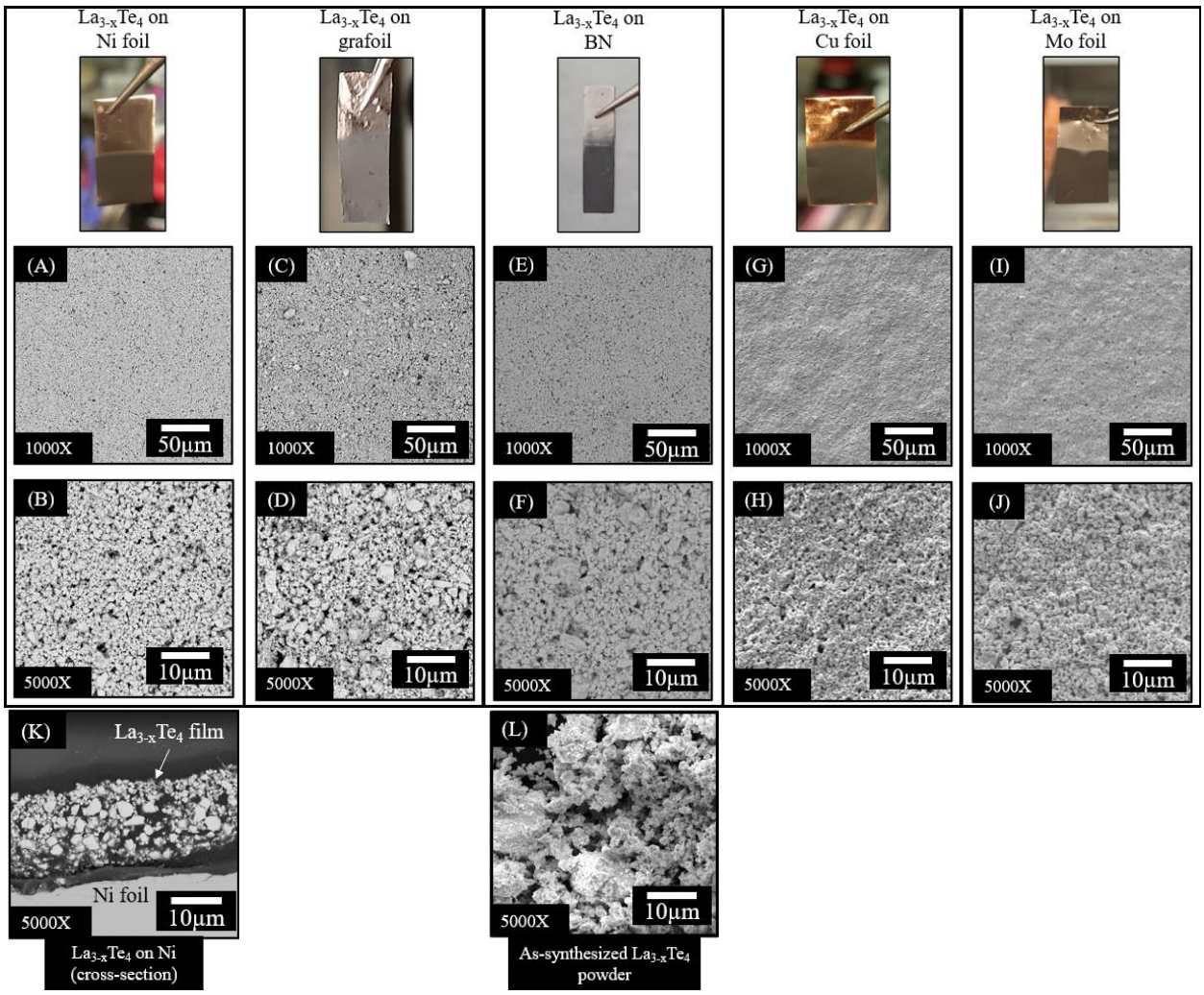

Figure 3.4: Pictures and SEM images of $La_{3-x}Te_4$ films deposited on (A, B) Ni foil, (C, D) grafoil, (E, F) BN, (G, H) Cu foil, and (I, J) Mo foil substrates via EPD. In all cases, EPD was performed at 100 V for 10 min using $La_{3-x}Te_4$ powder suspended in THF at a concentration of 10 mg/mL. Deposition on BN was achieved by attaching Ni mesh during deposition. The pictures show uniform coverage of the immersed area on the substrate. (A), (C), (E), (G) and (I) are all taken at 1000X magnification. (B), (D), (F), (H), and (J) are all taken at 5000X magnification. (K) is a cross-sectional SEM image of $La_{3-x}Te_4$ on Ni foil, showing that the film is between 10-15 µm thick. (L) is an SEM image of as-synthesized $La_{3-x}Te_4$ powder taken at 5000X magnification for comparison to the morphology of EPD films.

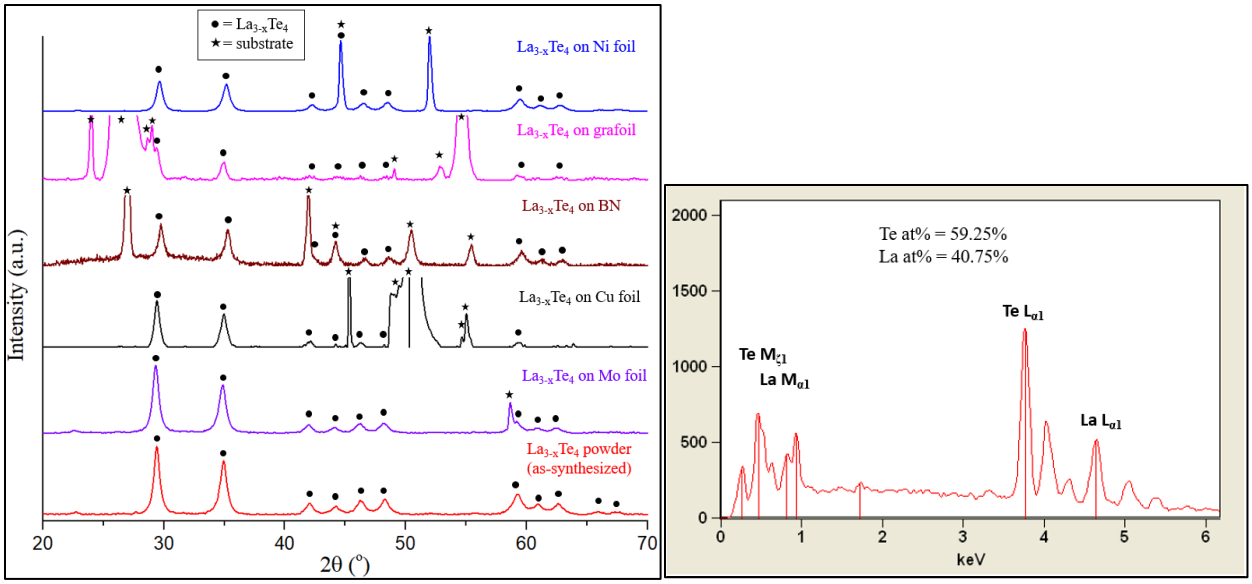

Figure 3.5: (Left) XRD scans for $La_{3-x}Te_4$ deposited via EPD on Ni foil, grafoil, BN, Cu foil, and Mo foil. In all cases, EPD was performed at 100 V for 10 min using $La_{3-x}Te_4$ powder suspended in THF at a concentration of 10 mg/mL. The bottom XRD scan is of as-synthesized $La_{3-x}Te_4$ powder. All samples are phase-pure $La_{3-x}Te_4$. (Right) EDX scan for $La_{3-x}Te_4$ deposited on Ni foil, showing the atomic percentages of La and Te are within the solid-solution range of 57-60 at% Te (43-40 at% La) for $La_{3-x}Te_4$.

The ability to deposit phase-pure $La_{3-x}Te_4$ films on chemically diverse substrates without a change in microstructure is a significant achievement. The EPD technique preserves the starting powder stoichiometry, which is crucial for maintaining optimum thermoelectric performance, and consistently deposits uniform microstructures which demonstrates good reproducibility. These properties show that EPD of $La_{3-x}Te_4$ can be extended to a variety of substrate materials without requiring a change in deposition parameters. This flexibility has considerable implications for both device and composite fabrications. The ability to deposit $La_{3-x}Te_4$ on various metals without a binder material or bonding layer can simplify manufacturing of device metallization layers. It also expands opportunities for exploration of potential composite systems beyond $La_{3-x}Te_4$-Ni. Additionally, the ability to deposit $La_{3-x}Te_4$ on electrically insulating substrates is significant for characterization of thin film thermoelectric performance since insulating substrates are generally preferred for such measurements.

3.7 EPD of $La_{3-x}Te_4$ on Non-planar Substrates

To further demonstrate the processing versatility of EPD, $La_{3-x}Te_4$ was deposited on non-planar substrates to validate deposition on complex geometries. Figure 3.6 shows photos and SEM images of $La_{3-x}Te_4$ deposited on Ni mesh, Ni foam, and Cu wire. The $La_{3-x}Te_4$ coating is uniform and conformal for all substrate geometries. For deposition on Ni foam (Figure 3.6D-F), the $La_{3-x}Te_4$ coating infiltrates several layers into the substrate. The particulate morphology of the coatings is identical to deposits on planar substrates with porosity values around 30-35% (calculated by ImageJ analysis). Cross-sectional SEM images (Figure 3.6C, F, and I) show that the deposit coats uniformly around the substrates and conforms to complex geometries. As with the planar substrates, coating thicknesses are 10-15 μm. XRD scans (Figure 3.7) demonstrate the phase purity of the deposits.

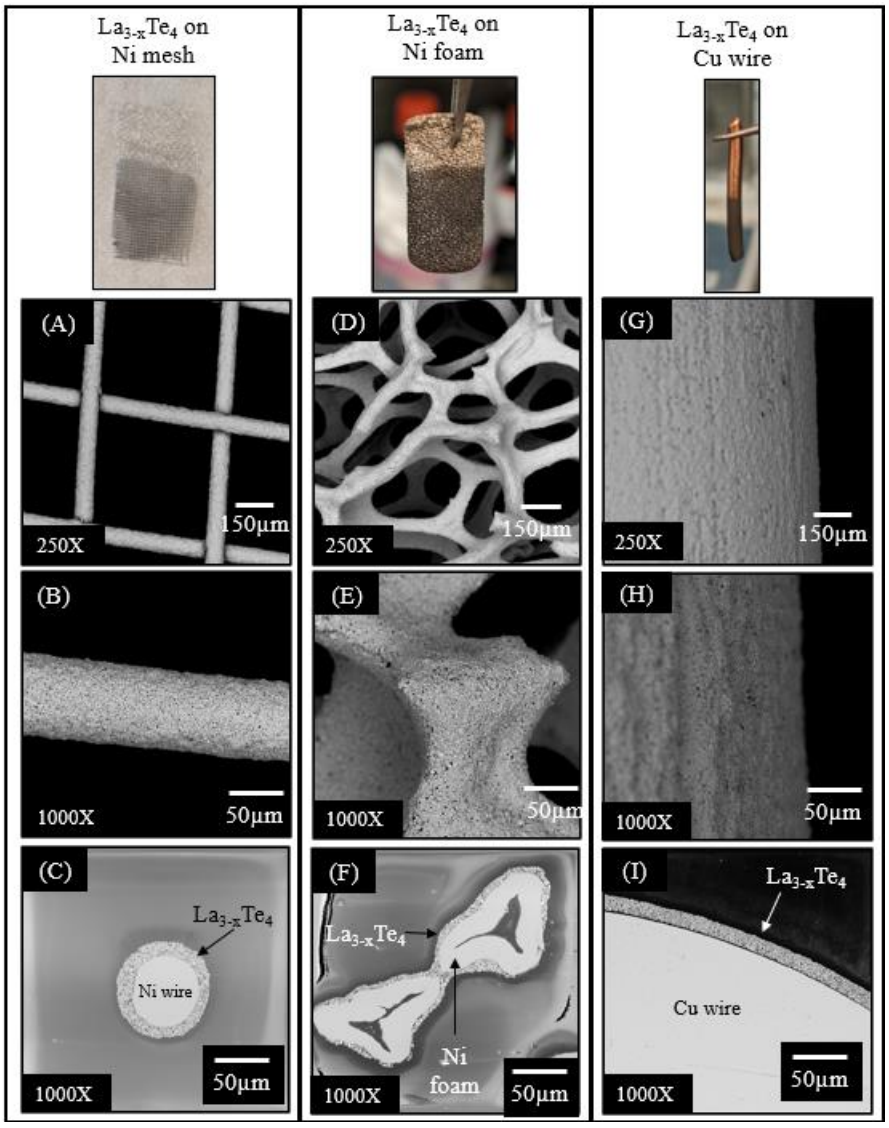

Figure 3.6: Pictures and SEM images of $La_{3-x}Te_4$ deposited on (A-C) Ni mesh, (D-F) Ni foam, and (G-I) Cu wire. In all cases, EPD was performed at 100 V for 10 min using $La_{3-x}Te_4$ powder suspended in THF at a concentration of 10 mg/mL. The pictures show uniform coverage of the immersed area on the substrate. (A), (D), and (E) are all taken at 250X magnification. (B), (C), (E), (F), (H), and (I) are all taken at 1000X magnification. (C), (F), and (I) are cross-sectional images for $La_{3-x}Te_4$ on Ni mesh, Ni foam, and Cu wire, respectively.

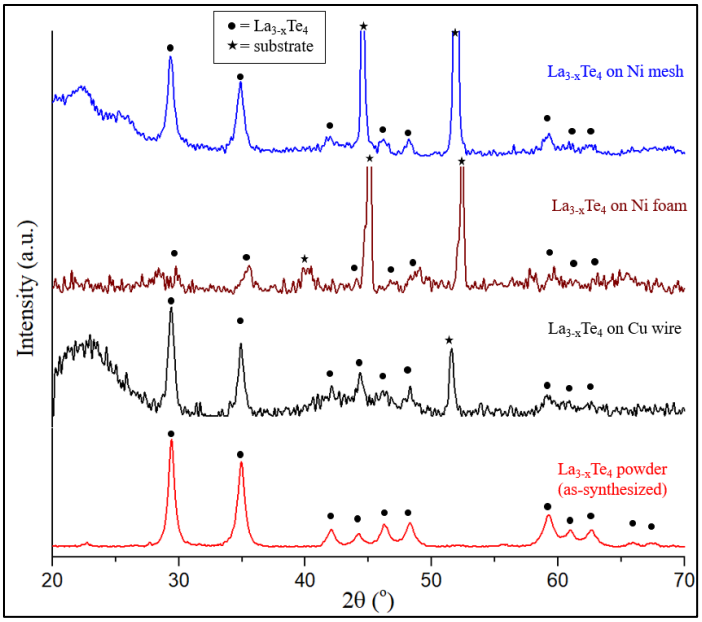

Figure 3.7: XRD scans of $La_{3-x}Te_4$ deposited on Ni mesh, Ni foam, and Cu foil. In all cases, EPD was performed at 100 V for 10 min using $La_{3-x}Te_4$ powder suspended in THF at a concentration of 10 mg/mL. The bottom XRD scan is of as-synthesized $La_{3-x}Te_4$ powder. All samples are phase-pure $La_{3-x}Te_4$.

The uniformity and good infiltration of $La_{3-x}Te_4$ deposits on these irregular substrates indicate good throwing power of the $La_{3-x}Te_4$/THF suspension, which is defined in the literature as the ability of a suspension to deposit uniform coatings onto non-uniform substrates.[21,31] This property allows for deposition of uniform coating thicknesses on complex substrates and infiltration of the coating into interior/recessed areas of the substrate. Therefore, these results demonstrate that the $La_{3-x}Te_4$/THF suspension is well-suited for uniform deposition on both planar and non-planar substrates due to excellent dispersion and stability of the $La_{3-x}Te_4$ particles as well as high throwing power of the suspension.

EPD of $La_{3-x}Te_4$ on non-planar substrates is significant for device fabrication because it expands the possible architectures into which $La_{3-x}Te_4$ can be incorporated. This approach achieves uniform, complex shapes for $La_{3-x}Te_4$ while avoiding machining of the bulk material which is desirable due to its poor mechanical properties. Furthermore, in the case of $La_{3-x}Te_4$-Ni

composites, deposition of $La_{3-x}Te_4$ on varying Ni geometries provides a foundation for studying the effect of different Ni inclusion morphologies on thermoelectric performance.

3.8 Co-EPD of $La_{3-x}Te_4$ and Ni to Fabricate $La_{3-x}Te_4$-Ni Composite Films

As an extension of $La_{3-x}Te_4$-Ni composite fabrication, $La_{3-x}Te_4$-Ni composite films were deposited via co-EPD of $La_{3-x}Te_4$ and Ni powder. The Ni powder (80-150 nm average particle size, obtained from Alfa Aesar) was used as-received without further treatment. Anhydrous $NiCl_2$ was added as to THF as a charging agent since it dissociates into Ni^{2+} ions which are hypothesized to adsorb on the surface of the Ni particles and provide a positive surface charge.[32–35] The EPD suspension was prepared by adding 1 mM $NiCl_2$ to THF and suspending Ni powder at a concentration of 1 mg/mL. Ni films are synthesized when only Ni powder is added to the suspension, and $La_{3-x}Te_4$-Ni films are synthesized when both $La_{3-x}Te_4$ powder and Ni powder are added to the suspension. Deposition was performed at 100 V. Due to limited stability of the Ni particles in suspension, deposition time was limited to 3 minutes.

Figure 3.8 shows photos and SEM images of Ni powder and $La_{3-x}Te_4$-Ni films deposited on Cu and Ni foil substrates. Ni films (Figure 3.8A-B) have good area coverage of the substrates with similar morphology to the starting powder (Figure 3.8G), though there is some aggregation of the Ni particles due to their non-optimized surface charge. For co-deposited $La_{3-x}Te_4$-Ni films (Figure 3.8C-D), clusters of Ni particles (visible as darker grey particles) are distributed throughout the $La_{3-x}Te_4$ matrix. The distribution of Ni particles is more evident in the EDX mapping in Figure 3.9. Ni powder may also be deposited on top of an $La_{3-x}Te_4$ film (Figure 3.8E)

which demonstrates the possibility of synthesizing an $La_{3-x}Te_4$-Ni layered structure. Gaps in the Ni film are visible in both the top-down image (Figure 3.8E) and the cross-section (Figure 3.8F).

XRD scans (Figure 3.9) of $La_{3-x}Te_4$-Ni deposited on Cu foil verify successful co-deposition of phase-pure $La_{3-x}Te_4$ and Ni powder. Cl signal in the EDX mapping (Figure 3.9) is attributed to $NiCl_2$ contamination. $NiCl_2$ is sparingly soluble in THF [32], so some undissolved $NiCl_2$ particles co-EPD alongside Ni. The $NiCl_2$ particles, which are particularly visible in the Ni films (Figure 3.8A-B), are flat and acicular. Further optimization of Ni EPD is necessary to improve the suspension stability and deposit uniformity and avoid $NiCl_2$ contamination.

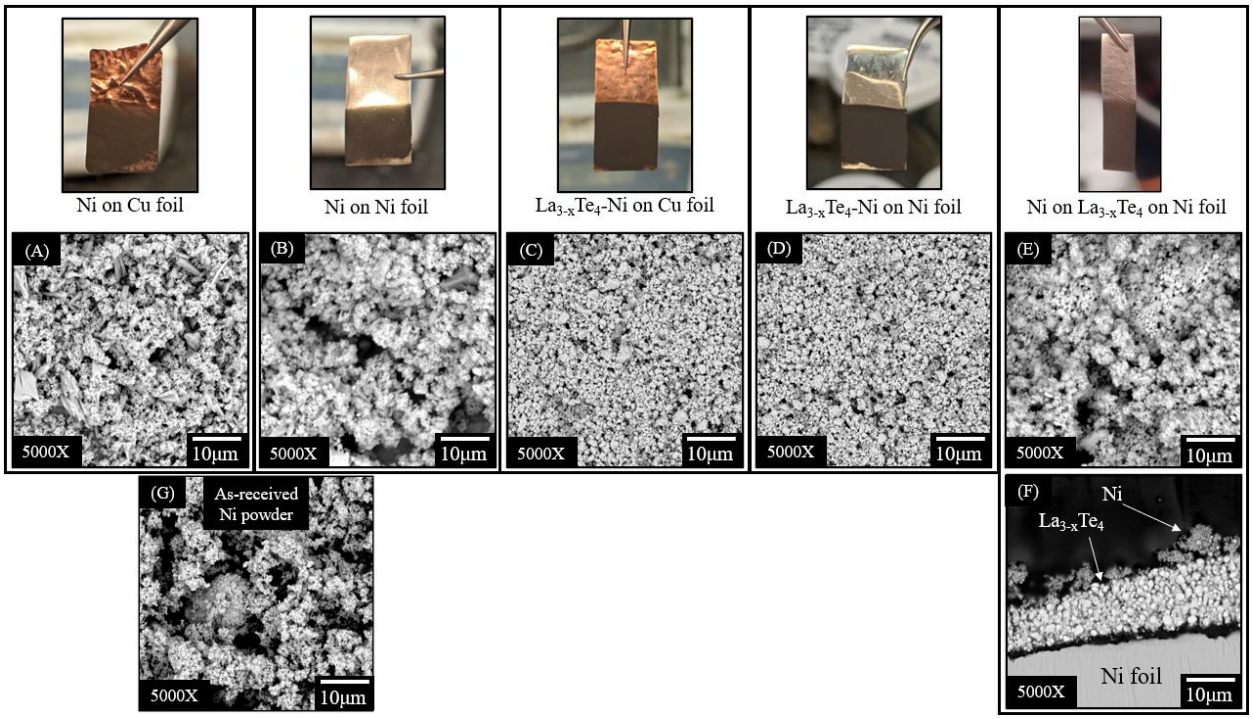

Figure 3.8: SEM images of (A-F) Ni and $La_{3-x}Te_4$-Ni deposits on Cu and Ni foil at 100V for 3min (solvent = THF+1 mM $NiCl_2$). $La_{3-x}Te_4$ powder concentration = 10 mg/mL and Ni powder concentration = 1 mg/mL. (G) As-received Ni powder (80-150 nm average particle size). All images are at 5000X magnification.

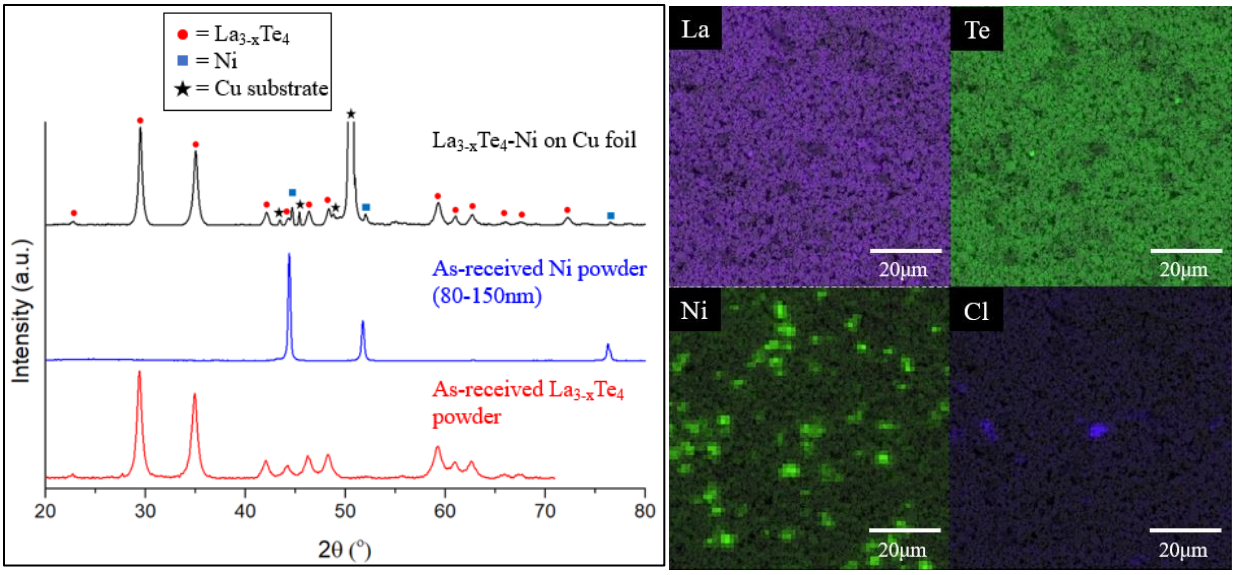

Figure 3.9: (Left) XRD scan for $La_{3-x}Te_4$-Ni deposited on Cu foil at 100V for 3min (solvent = THF+1mM $NiCl_2$), with as-received Ni and $La_{3-x}Te_4$ powders for reference. (Right) EDX mapping for $La_{3-x}Te_4$-Ni deposited on Cu foil. Clusters of Ni particles are distributed throughout the $La_{3-x}Te_4$ film. Cl signal indicates co-deposition of $NiCl_2$ particles.

3.9 Effect of EPD Voltage and Time on $La_{3-x}Te_4$ Microstructure and Film Thickness

To characterize the effect of deposition parameters on $La_{3-x}Te_4$ film microstructure, EPD was performed at different voltages (Figure 3.10) and times (Figure 3.11). Regardless of deposition parameters, a thickness gradient occurs between the upper and lower portions of the film because of the vertical orientation of the substrate during deposition. Due to particle sedimentation, the films are thicker in the direction of gravity and thus have greater thickness in the lower portions compared to the upper portions.

At deposition voltages below 100 V (Figure 3.10), the films have poor uniformity with <100% area coverage of the substrate (Table 3.2). Deposited mass (Figure 3.12A) increases linearly with applied voltage with the main effect of applied voltage being an improvement in uniformity and homogeneity of the film. Below 100 V, there is sparse coverage of the substrate and a small film thickness in the upper portion of the film, both of which improve with applied voltage. In the lower portions of the film, the coverage and thickness are relatively constant with

applied voltage. Since the driving force for particle migration and deposition increases with electric field strength ((Equation 3.2) and (Equation 3.3), the higher applied voltages counteract sedimentation and promote uniform distribution of particles on the substrate. At higher voltages, the particles migrate to the substrate prior to significant sedimentation and, once arrived, incoming particles experience a high driving force to distribute evenly on the substrate to obtain the densest configuration.[20,21] Deposition voltage is therefore critical in controlling deposit uniformity and substrate coverage. For the $La_{3-x}Te_4$/THF system, these results demonstrate that a deposition voltage of 100 V provides the necessary driving force to mitigate sedimentation and achieve good film uniformity and substrate coverage.

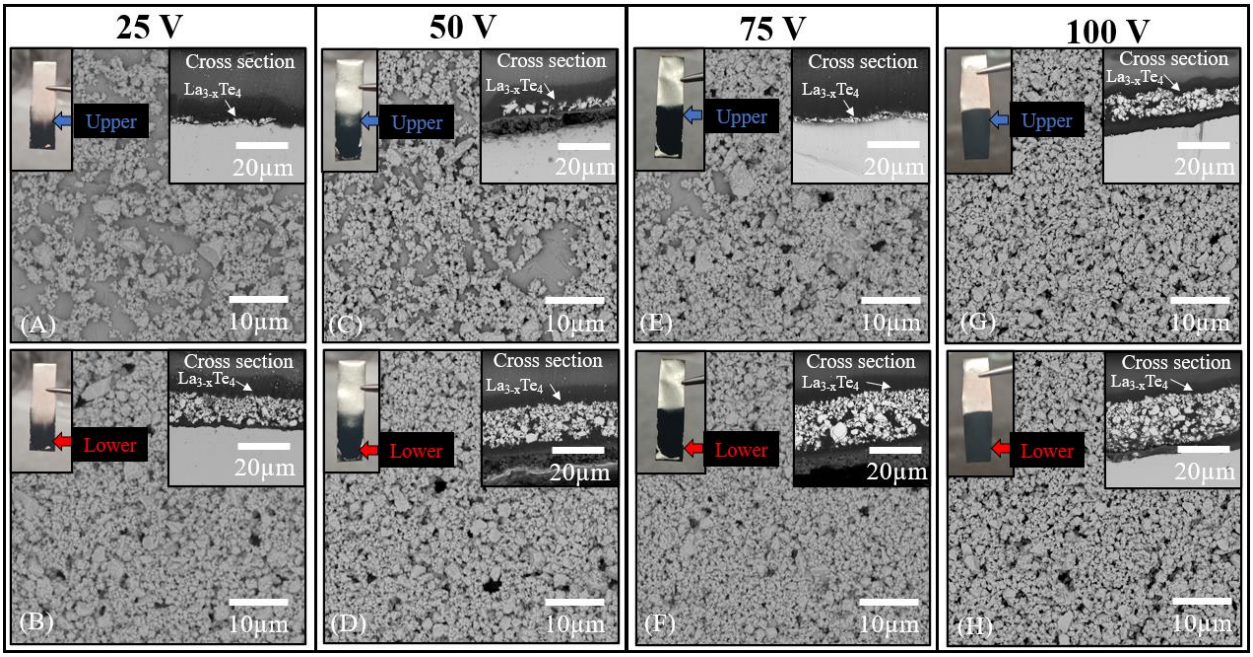

Figure 3.10: Photos and SEM images of $La_{3-x}Te_4$ on deposited Ni foil for 10 minutes at 25, 50, 75, and 100 V. Solvent = THF and $La_{3-x}Te_4$ powder concentration = 10 mg/mL. All SEM images are at 5000X magnification. The inset with the blue or red arrow indicates the relative vertical position on the film at which the corresponding images were taken.

Table 3.2: Percentage coverage of the immersed substrate for EPD of $La_{3-x}Te_4$ as a function of voltage.

Deposition voltage	25 V	50 V	75 V	100 V
Percentage of the immersed area covered by the deposit	54 %	84 %	89 %	100 %

While deposition voltage primarily affects uniformity, deposition time affects both film thickness and uniformity (Figure 3.11). Up to 20 minutes, film thickness (Figure 3.12B) increases with deposition time for both the upper and lower portions of the film, reaching as high as 33 μm for the 20- and 25-minute samples. However, the disparity between the upper and lower thicknesses also increases significantly with time. As deposition time increases above 20 minutes, film thickness becomes constant and eventually decreases. This behavior is also observed in the deposited mass (Figure 3.12B), which increases linearly up to 20 minutes before decreasing at 25 and 30 minutes.

Again, sedimentation effects are responsible for the increase in thickness gradient between the upper and lower portions of the sample with deposition time. The $La_{3-x}Te_4$ particles gradually sediment during EPD, with an increasing fraction of particles flocculating as time increases. This leads to a higher concentration of particles towards the bottom of the suspension and causes the films to become extremely thick in the lower portions of the substrate. The plateau and subsequent decrease in thickness at times >20 minutes is likely due to poor film adhesion, spalling, and cracking which are known issues for large EPD film thicknesses.[36] These issues are evident in Figure 3.11I-L as the films deposited for ≥20 minutes exhibit significant surface roughness and large variations in thickness. Agglomerated particles (Figure 3.11H), gaps (Figure 3.11J), and valleys (Figure 3.11L) are present in the films which highlights an overall degradation in film quality at long deposition times. Therefore, even though deposit thickness can be controlled and increased with deposition time, longer times sacrifice film quality due to sedimentation effects in the suspension and adhesion issues with thicker films.

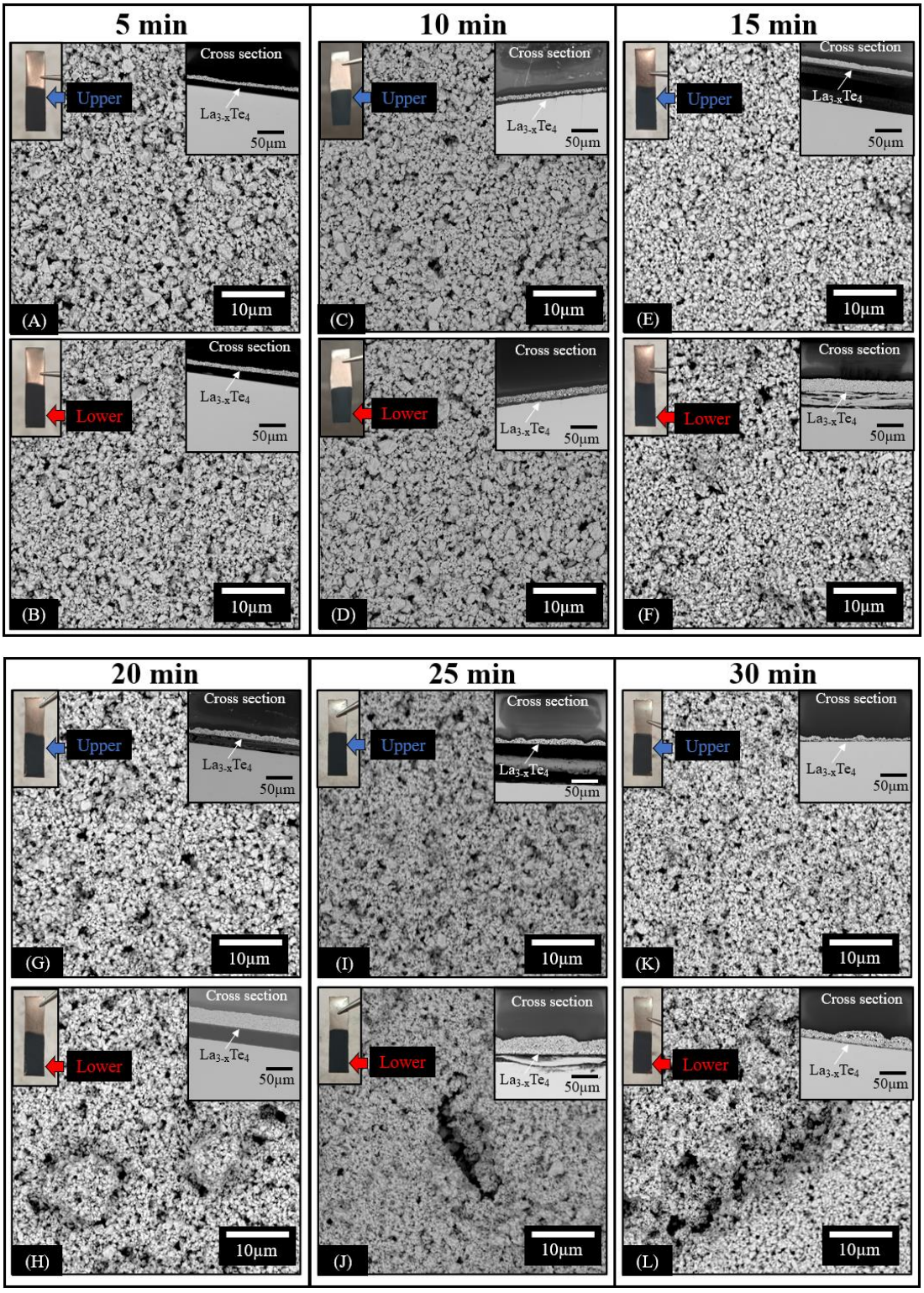

Figure 3.11: Photos and SEM images of $La_{3-x}Te_4$ deposited on Ni foil at 100V for 5, 10, 15, 20, 25, and 30 minutes. Solvent = THF and $La_{3-x}Te_4$ powder concentration = 10 mg/mL. All top-down images are at 5000X magnification. All cross-section images are at 1000X magnification. The inset with the blue or red arrow indicates the relative vertical position on the film at which the corresponding images were taken.

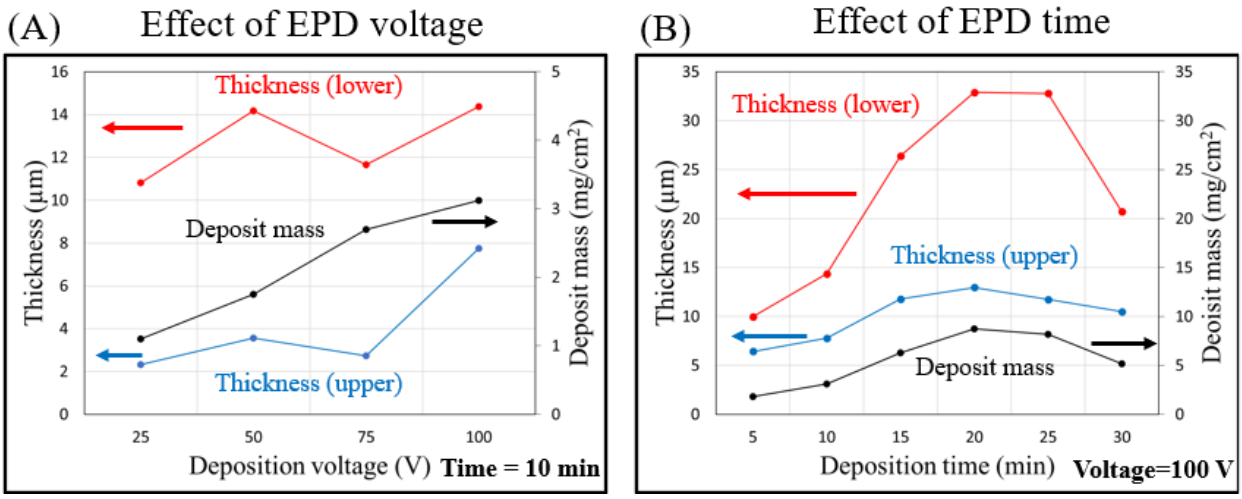

Figure 3.12: Plots showing the measured thicknesses and deposited mass for $La_{3-x}Te_4$ films on Ni foil as a function of (A) EPD voltage and (B) EPD time. For all samples, the solvent is THF and $La_{3-x}Te_4$ powder concentration is 10 mg/mL. The upper and lower thickness designations refer to relative vertical location on the samples as indicated in Figure 3.10 and Figure 3.11.

These results demonstrate that EPD voltage and time have significant effects on $La_{3-x}Te_4$ film microstructure, thickness, and quality. Applied voltage primarily affects film uniformity and deposited mass, but not film thickness. Higher voltages mitigate sedimentation effects and increase the driving force for uniform particle distribution on the substrate. 100 V provides the necessary driving force for uniform deposition as lower voltages exhibit <100% area coverage of the substrate. Conversely, deposition time affects both film uniformity and thickness. Thickness increases with deposition time up to 20 minutes before plateauing and subsequently decreasing at 25 and 30 minutes. The thickness gradient between the upper and lower portions of the film becomes more substantial with increasing deposition time. Long deposition times cause a decrease in overall film quality due to associated sedimentation effects in the suspension as well as poor adhesion, cracking, and spalling issues that are common in thick EPD films. Future optimization of the $La_{3-x}Te_4$/THF suspension and deposition cell design can mitigate sedimentation and improve overall film quality to allow for synthesis of thicker $La_{3-x}Te_4$ films.

3.10 Determination of Zeta Potential and Investigation of Surface Charge Development for the $La_{3-x}Te_4$/THF Suspension

Calculation of Zeta Potential

Characterization of the $La_{3-x}Te_4$/THF suspension properties is critical for a fundamental understanding of the excellent suspension stability, high-quality EPD coatings, and nature of surface charge development. The Hamaker equation ((Equation 3.3) and Smoluchowski equation (Equation 3.1) are valuable models for determining electrophoretic mobility and zeta potential from experimental data. Assuming the EPD parameters (μ, E, A and C) are constant with time, (Equation 3.3 predicts a linear increase in deposit mass as a function of deposition voltage and time. Therefore, (Equation 3.3 can be used to calculate electrophoretic mobility from the slope of a linear fit to data for deposit mass as a function of EPD voltage (constant time) or EPD time (constant voltage). Zeta potential can then be calculated by substituting the value of electrophoretic mobility and solvent parameters (viscosity and dielectric constant) into the Smoluchowski equation (Equation 3.1).

Figure 3.13 shows the results of this analysis for the $La_{3-x}Te_4$/THF suspension, where electrophoretic mobility and zeta potential were calculated from experimental measurements of deposit mass as a function of EPD voltage (Figure 3.13A) and time (Figure 3.13B). These results are presented in Table 3.3 where they are compared to literature values for the Bi_2Te_3/THF suspension[11]. The zeta potential for the $La_{3-x}Te_4$/THF suspension is calculated to be 48.6 mV and 59.8 mV based on fits of deposit mass as a function of EPD voltage and time, respectively. The discrepancy in values between the two methods may be due to <100% substrate coverage and non-uniformity of the films for applied voltages <100 V, leading to an underestimation of zeta

potential calculated from deposit mass as a function of voltage. Regardless, the excellent stability of the $La_{3-x}Te_4$/THF suspension is highlighted by the value of zeta potential ≥30 mV.[23,24]

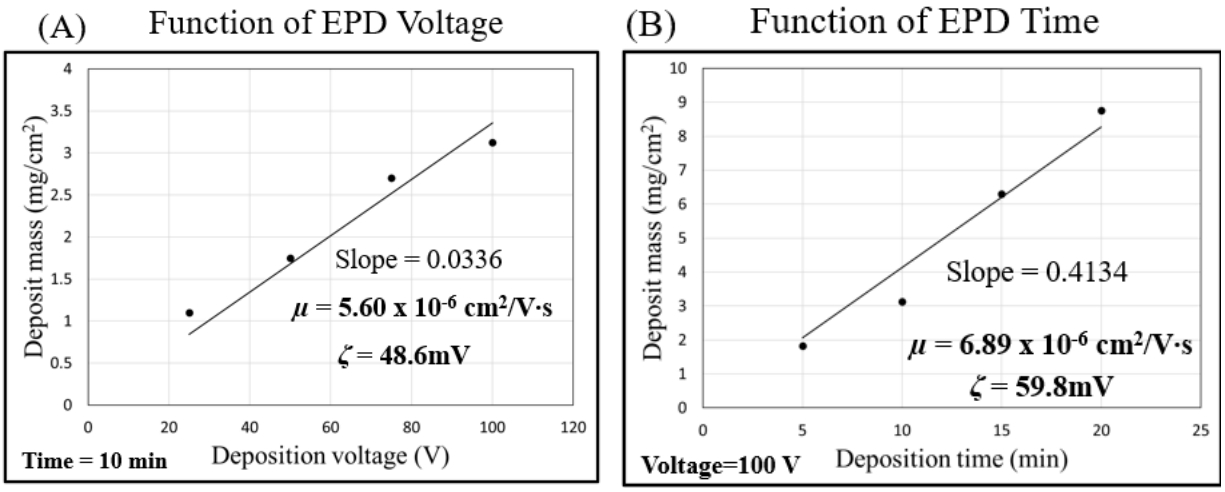

Figure 3.13: Calculation of electrophoretic mobility (μ) and zeta potential (ζ) for the $La_{3-x}Te_4$/THF suspension. The plots show a linear fit fit to experimental measurements for deposit mass as a function of (A) EPD voltage and (B) EPD time. Electrophoretic mobility was calculated from the slope of the line by integration and rearrangement of (Equation 3.3, where E = 100 V/cm, and C = 10 mg/mL. Zeta potential was calculated by substituting the calculated value of electrophoretic mobility into (Equation 3.1 and solvent parameters for THF (η = 0.46cP at 25°C, ε_r = 7.52)[37].

Table 3.3: Calculated values for μ and ζ for $La_{3-x}Te_4$ suspended in THF.

Suspension	Electrophoretic mobility (μ)	Zeta potential (ζ)
$La_{3-x}Te_4$ suspended in THF (calculated from EPD mass vs voltage)	**5.60 x 10^{-6} cm^2/V·s**	**48.6 mV**
$La_{3-x}Te_4$ suspended in THF (calculated from EPD mass vs time)	**6.89 x 10^{-6} cm^2/V·s**	**59.8 mV**
Bi_2Te_3 suspended in THF (Talebi *et al*) ([11])	1.25x10^{-4} cm^2/V·s	62mV

The high value of zeta potential is responsible for the excellent stability and dispersion of the $La_{3-x}Te_4$ particles suspended in THF. These qualities achieve uniform, high-quality $La_{3-x}Te_4$ deposits with good green density as well as good throwing power which allows for uniform deposition on non-planar substrates. Furthermore, the zeta potential value of 59.8 mV calculated for $La_{3-x}Te_4$ suspended in THF is within ~3.5% of the 62 mV zeta potential obtained in the

literature for Bi_2Te_3 suspended in THF. This similarity corroborates the favorable combination of solvent properties associated with THF that were observed by Talebi *et al* and supports its selection as the solvent for EPD of $La_{3-x}Te_4$.

Investigation of the Surface Charge Mechanism for $La_{3-x}Te_4$ Suspended in THF

A fundamental understanding of the associated surface charging mechanisms for $La_{3-x}Te_4$ suspended in THF provides beneficial insights into the nature of high zeta potential and positive surface charge for the $La_{3-x}Te_4$/THF suspension. Since the interaction between the $La_{3-x}Te_4$ surface and THF plays a critical role in these mechanisms, XPS was employed to characterize the surface chemistry of $La_{3-x}Te_4$ powder after suspension in THF. Figure 3.14 shows XPS scans for $La_{3-x}Te_4$ powder after it was suspended in THF followed by vacuum drying for 24 hours. All surface species and valence states are the same as those for as-synthesized $La_{3-x}Te_4$ powder (discussed in Chapter 2). However, compared to the as-synthesized powder, there is an increase in intensity for the components associated with Te^0, Te^{4+}, and -OH groups after suspension of the powder in THF. The relative percentages for the various components in the Te 3d region and O 1s region are compared in Table 3.4 for as-synthesized $La_{3-x}Te_4$ powder and after suspension in THF. There is an increase of about 10.1% and 16.4% in the concentration of Te^0 and Te^{4+} valence states, respectively, and an increase of about 5.3% in hydroxyl group (-OH) concentration after suspension in THF.

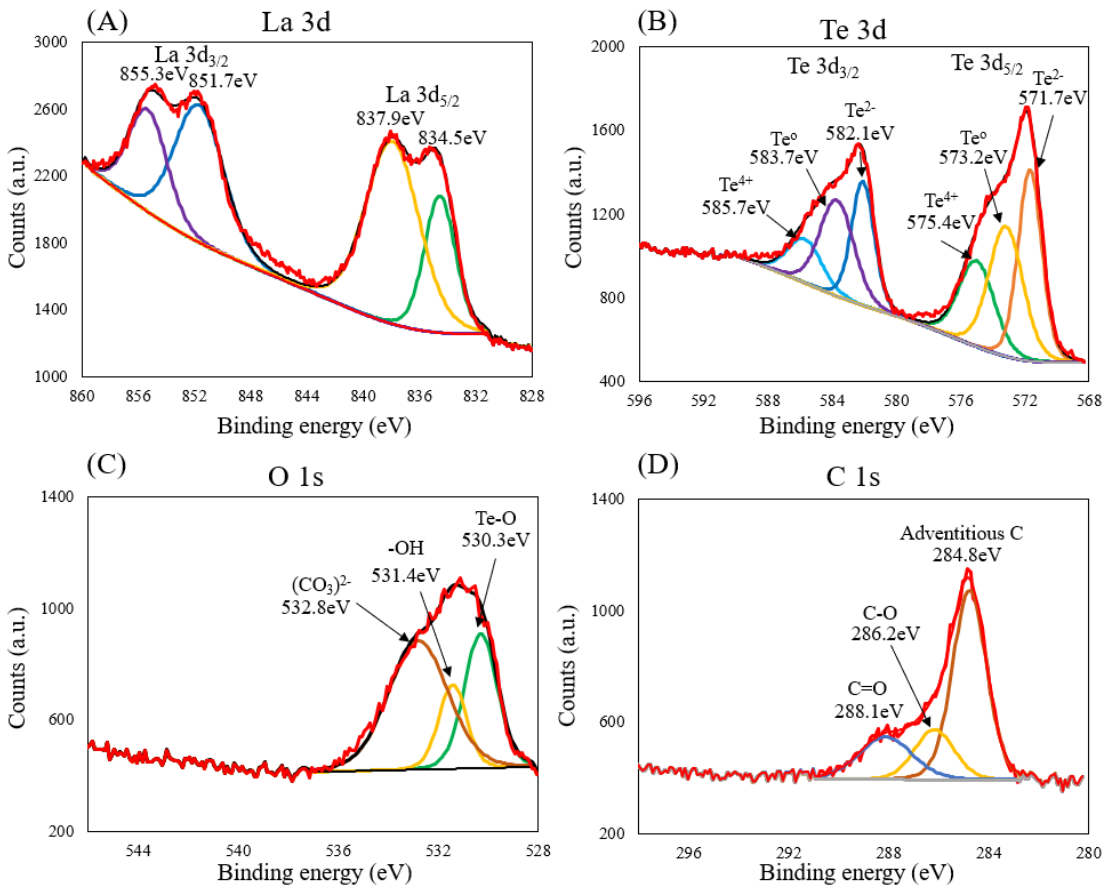

Figure 3.14: XPS scans for $La_{3-x}Te_4$ powder after suspension in THF at a concentration of 10 mg/mL followed by vacuum drying for 24 hours. (A) La 3d, (B) Te 3d, (C) O 1s, and (D) C 1s regions. The binding energies and associated valence states or chemical bonds for fitted components are listed. (A) In the La 3d region, the two pairs of peaks are fit with four components corresponding to La^{3+}. (B) In the Te 3d region, there are a pair of peaks that are comprised of three components, with each component corresponding to Te^{2-} (La-Te), Te^0 (Te metal), and Te^{4+} (Te-O). (C) The broad O 1s peak is fit with three components corresponding to hydroxyl groups (-OH), carbonate groups $(CO_3)^{2-}$, and Te-O bonding. (D) In the C 1s region, the adventitious carbon component is used for binding energy reference to 284.8eV. The other two components are associated with C-O and C=O bonding.

Table 3.4: Relative percentages of Te 3d valence states and O 1s species for $La_{3-x}Te_4$ powder.

	Te 3d			**O 1s**		
	Te^{2-}	Te^0	Te^{4+}	Te-O	-OH	$(CO_3)^{2-}$
$La_{3-x}Te_4$ powder (as-synthesized)	64.09%	22.87%	13.04%	32.90%	10.96%	56.14%
$La_{3-x}Te_4$ powder (suspended in THF)	37.59%	39.28%	23.13%	30.70%	16.26%	53.03%

The changes in surface states provide strong evidence for surface charge development on $La_{3-x}Te_4$ particles by an increase in both Te^0 and Te^{4+} as well as surface hydroxyl concentrations. In the literature, surface charge development on solid powders in EPD suspensions is proposed to occur by two general mechanisms[20,21]: 1) electron transfer between the solid particles and liquid solvent (in the absence of water) and 2) interaction of surface hydroxyl groups with the solvent based on pH (in the presence of water) (Equation 3.4 and (Equation 3.5). In the first mechanism, electron transfer occurs due to differences in electron donicity between the solid and liquid[20,21,38], and particles develop a positive or negative charge if they donate electrons or accept electrons, respectively. In the second mechanism, the pH determines whether the surface charge is positive or negative[20]:

<u>Positive surface charge</u>: $M\text{-}OH + H^+ \rightarrow M\text{-}(OH_2)^+$ (for $pH < pH_{pzc}$) (Equation 3.4)

<u>Negative surface charge</u>: $M\text{-}OH \rightarrow M\text{-}O^- + H^+$ (for $pH > pH_{psz}$) (Equation 3.5)

The increase in concentration of Te^0 and Te^{4+} after exposure of the powder to THF indicates that the first charging mechanism associated with electron transfer is active in surface charge development for the $La_{3-x}Te_4$/THF suspension. The increase in Te valence state suggests that the $La_{3-x}Te_4$ surface has a higher electron donicity than the solvent such that tellurium donates electrons to the solvent. This mechanism is consistent with the positive surface charge observed experimentally for $La_{3-x}Te_4$ powder suspended in THF. The magnitude of surface charging is likely enhanced by the multiple valence states of Te which allow for donation of several electrons per Te atom and enables the large value of zeta potential.

Additionally, the increased surface hydroxyl concentration in the O 1s region (Figure 3.14C) after exposure to THF provides evidence that the second charging mechanism (associated

with interaction of surface hydroxyl groups with water) is also active. Despite the fact that the THF is anhydrous, it contains about 12 ppm water (~0.001 vol% H_2O) as indicated by the certificate of analysis provided by ThermoFisher Scientific. Trace amounts of water in the solvent are responsible for the increase in surface hydroxylation after suspension of $La_{3-x}Te_4$ in THF. The tendency of THF to act as a mild Lewis base[39] is hypothesized to cause water to act as an acid and provide protons which are available to interact with the $La_{3-x}Te_4$ surface hydroxyl groups via (Equation 3.4. Like the electron donor mechanism, this mechanism also yields a positive surface charge on the $La_{3-x}Te_4$ surface. Since the water concentration is low, the development of surface charge on $La_{3-x}Te_4$ suspended in THF is therefore due to both electron transfer with the solvent and interaction of trace water with $La_{3-x}Te_4$ surface hydroxyl groups. The high value of zeta potential is aided by the combined surface charge resulting from each mechanism.

Effects of Water Concentration on EPD of $La_{3-x}Te_4$

To study the effects of water content on these charging mechanisms, XPS scans were performed on $La_{3-x}Te_4$ powder suspended in THF with increasing water concentration (Figure 3.15). The suspensions were prepared by adding deionized water to the $La_{3-x}Te_4$/THF suspension followed by drying in vacuum for 24 hours. The listed water concentration includes the deionized water added to the suspension and trace water content (~0.001 vol%) in the as-received THF.

As the water concentration in THF increases above the nominal 0.001 vol% to 0.006 vol%, the relative -OH concentration increases from 16.26% to 43.16% (Figure 3.15A) which indicates a significant increase in surface hydroxylation. The concentrations of Te^0 and Te^{4+} (Figure 3.15C) are much lower at 0.006 vol% H_2O than at 0.001 vol% H_2O, though they are still

elevated above those of the as-synthesized powder. The significant increase in -OH concentration after the addition of water to the suspension supports the hypothesis that trace water is responsible for increased surface hydroxylation of $La_{3-x}Te_4$ suspended in as-received THF (Figure 3.14). Additionally, as evidenced by the reduced concentration of Te^0 and Te^{4+}, an increase in water concentration promotes a shift in $La_{3-x}Te_4$ surface charging mechanism from one dominated by electron transfer to one dominated by interaction of surface hydroxyl groups with the solvent.

As the water concentration increases further to 0.01 vol%, additional components appear in the O 1s (Figure 3.15A) and C 1s (Figure 3.15B) spectra at 529.2 eV and 281.5 eV, respectively, which are both attributed to surface oxycarbonate species.[40,41] The lack of signal in the Te 3d or La 3d regions indicates that the surface is dominated by the organic species. It is evident that high water content in the suspension leads to reactions that form surface oxycarbonates, so the water concentration during EPD should be minimized to avoid formation of these undesirable species. However, trace water in the as-received THF on the order of 10 ppm is beneficial for surface charge development through its interaction with surface hydroxyl groups and does not affect the bulk composition of the material.

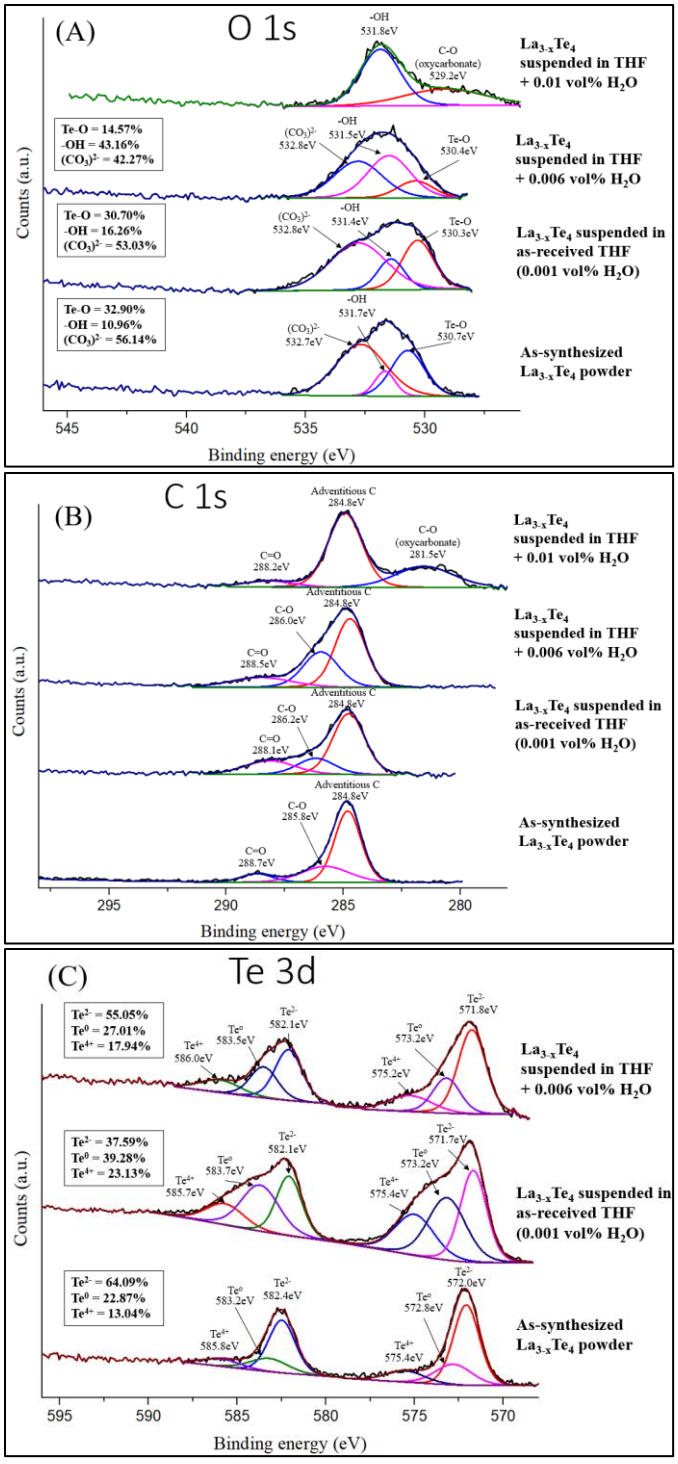

Figure 3.15: XPS scans of the (A) O 1s region, (B) C 1s region, and (C) Te 3d region for as-synthesized $La_{3-x}Te_4$ powder, $La_{3-x}Te_4$ powder suspended in THF (which contains 0.001 vol% residual H_2O) and vacuum dried for 24 hours, $La_{3-x}Te_4$ suspended in THF + 0.006 vol% H_2O and vacuum dried for 24 hours, and $La_{3-x}Te_4$ powder suspended in THF + 0.01 vol% H_2O and vacuum dried for 24 hours. Fitted components, associated bonds and valence states, and binding energy values are shown. The La 3d spectrum is omitted for all samples since it does not provide additional information for analysis or comparison. No Te 3d or La 3d signal were obtained for $La_{3-x}Te_4$ powder suspended in THF + 0.01 vol% H_2O due to oxycarbonate species forming at the surface.

To further study the influence of water on $La_{3-x}Te_4$ surface charge, the microstructure (Figure 3.16) and deposit thickness/mass (Figure 3.17) of $La_{3-x}Te_4$ EPD deposits were characterized as a function of water concentration in THF. Deposition always occurred on the negative electrode which indicates that the $La_{3-x}Te_4$ surface charge is positive regardless of water concentration. The film morphology is relatively unchanged as water concentration increases up to 0.01 vol% H_2O (Figure 3.16A-C and G-I). As it increases further to 0.1 vol% H_2O (Figure 3.16D and J), large pores and depressions dispersed throughout the film provide evidence of hydrogen evolution caused by the increased water content. Above 0.1 vol% H_2O (Figure 3.16E-F and K-L), the films are extremely patchy with poor adhesion to the substrate and the $La_{3-x}Te_4$ particles are embedded in an organic matrix due to reaction with the solvent.

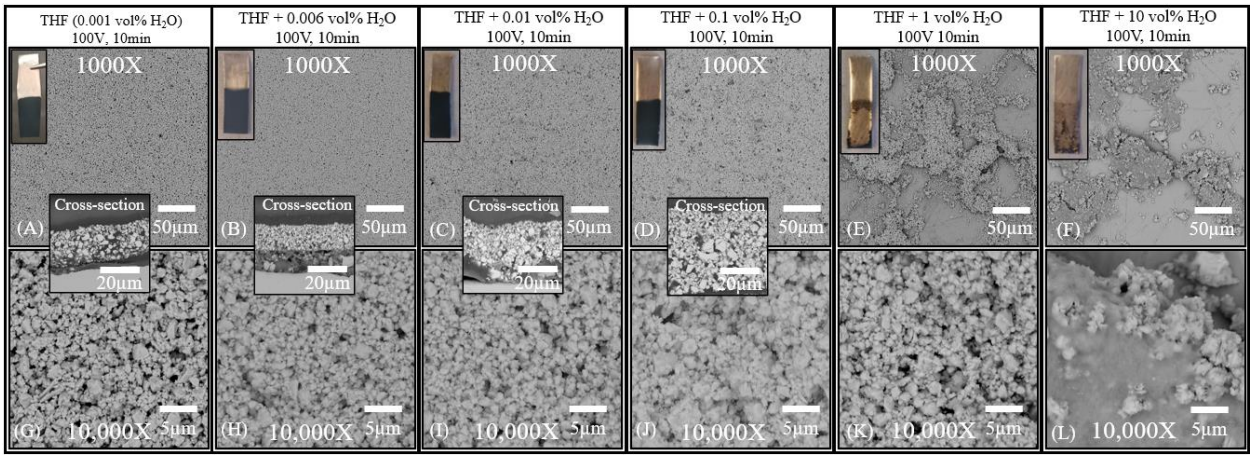

Figure 3.16: Photos and SEM images of $La_{3-x}Te_4$ deposited on Ni foil via EPD of $La_{3-x}Te_4$ powder suspended in THF with increasing water concentration. Deposition voltage = 100V, deposition time = 10 minutes, and $La_{3-x}Te_4$ powder concentration = 10 mg/mL for all samples. Images (A-F) are taken at 1000X magnification and (G-L) taken at 10,000X magnification. The cross-sectional images are taken at 5000X magnification.

Significant changes in film thickness and deposit mass (Figure 3.17) occur with increasing water concentration. Initially, there is minimal change in film thickness and deposit mass as water concentration increases from 0.001 and 0.006 vol% H_2O, followed by a large increase in both metrics as water concentration increases to 0.01 and 0.1 vol% H_2O. Thickness

measurements were not obtained for 1 and 10 vol% H_2O due to the poor film quality which is also reflected in the low deposited mass. For deposition from the suspension containing 0.1 vol% H_2O, film thickness exceeds 50 µm in the lower portion of the film and 20 µm in the upper portion. Since deposition voltage and time are unchanged, these results indicate a significant increase in electrophoretic mobility with water concentration that likely results from enhanced surface charging of the $La_{3-x}Te_4$. This trend supports the hypothesis that positive surface charge development for $La_{3-x}Te_4$ suspended in THF is a result of increased surface hydroxylation due to interactions of surface hydroxyl groups with water. However, water concentrations >0.01 vol% are associated with adverse effects such as formation of organic compounds and hydrogen evolution which are detrimental to overall film quality.

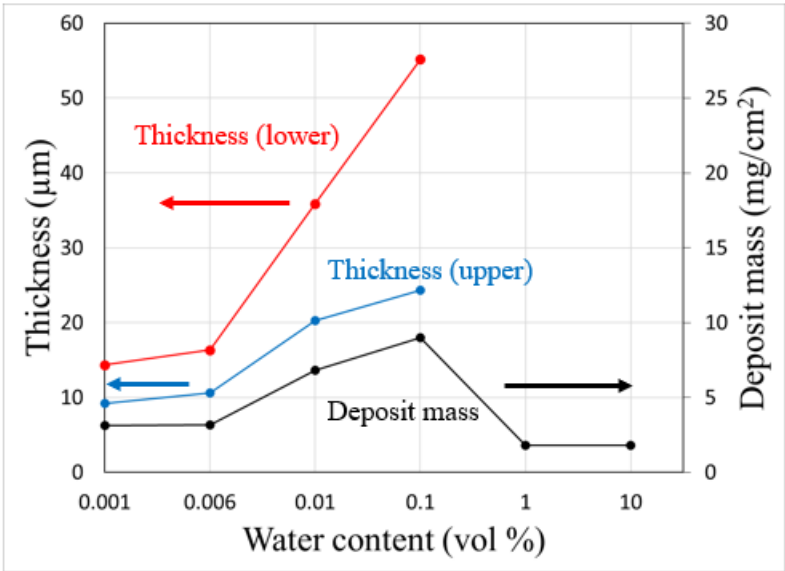

Figure 3.17: Plots of thickness and deposit mass as a function of water content in THF for EPD of $La_{3-x}Te_4$ on Ni foil. Deposition voltage = 100V, deposition time = 10 minutes, and $La_{3-x}Te_4$ powder concentration = 10 mg/mL for all samples.

The preceding results and analysis demonstrate that development of a positive surface charge on $La_{3-x}Te_4$ particles suspended in THF is due to a combination of electron transfer with the solvent and interaction of surface hydroxyl groups with residual water in THF. The $La_{3-x}Te_4$

surface has higher electron donicity than THF which promotes electron transfer from Te to the solvent and results in a positive surface charge. The multiple valence states of Te allow for transfer of several electrons per Te atom which contributes to the high value of zeta potential. Trace water in the as-received THF provides additional surface charging through increased surface hydroxylation. The magnitude of $La_{3-x}Te_4$ surface charge is enhanced by addition of water to the suspension and yields significant increases in electrophoretic mobility and deposit mass/thickness, though water concentrations >0.01 vol% H_2O lead to adverse reactions and formation of oxycarbonate species.

3.11 Summary and Conclusions

Electrophoretic deposition (EPD) of $La_{3-x}Te_4$ powder suspended in THF was demonstrated as a simple, effective, and versatile technique for depositing uniform $La_{3-x}Te_4$ films on various planar and non-planar substrates. A typical deposition voltage and time of 100V and 10 minutes, respectively, produce films that are 10-15 μm thick with an average porosity of about 35%. $La_{3-x}Te_4$ particles are evenly distributed without agglomeration, and film morphology is independent of substrate. Deposition voltage affects film uniformity and area coverage of the substrate, with 100 V providing the necessary driving force to achieve 100% area coverage. Deposition time can be used to control film thickness, though film quality degrades at times >20 minutes due to an increased vertical thickness gradient and cracking, spalling, and adhesion issues that are common with thick EPD films. $La_{3-x}Te_4$ and Ni powders can be co-deposited with the addition of $NiCl_2$ to THF to create a positive surface charge on the Ni powder, though the suspension requires further optimization to improve the stability of Ni particles and avoid $NiCl_2$ contamination in the deposit.

The stability and high-quality deposits obtained for the $La_{3-x}Te_4$/THF suspension are a consequence of the excellent surface charging indicated by the value of zeta potential ≥30 mV. The calculated value of zeta potential for the $La_{3-x}Te_4$/THF suspension of ~60 mV is similar to that of Bi_2Te_3/THF suspensions in the literature and supports the selection of THF as an appropriate solvent for EPD. Its moderate dielectric constant and tendency to act as a mild Lewis base give THF a favorable combination of solvent properties for EPD. The development of a positive surface charge results from two mechanisms: 1) electron transfer from Te to the solvent due to higher electron donicity of the $La_{3-x}Te_4$ surface, and 2) interaction of surface hydroxyl groups with residual water in THF. Both mechanisms contribute to the high value of zeta potential for $La_{3-x}Te_4$/THF suspensions.

Successful application of EPD to $La_{3-x}Te_4$ is a breakthrough processing achievement for the material and demonstrates reproducible synthesis of $La_{3-x}Te_4$ films with high deposition rate. This technique expands the processing routes available for synthesis of $La_{3-x}Te_4$ and $La_{3-x}Te_4$-Ni composites. Furthermore, it can simplify metallization steps during device fabrication since the material can be directly deposited on various metals without binder additives or bonding layers. The ability to deposit on non-planar substrates increases possible device architectures for $La_{3-x}Te_4$ by allowing for synthesis into complex geometries while avoiding machining of the bulk material. Characterization of the surface charging mechanism for $La_{3-x}Te_4$ in THF provides the foundation for understanding the suspension and solvent properties that lead to high-quality deposition. The versatility and scalability of EPD provide the potential for future optimization related to $La_{3-x}Te_4$ processing development and device manufacturing, as well as extension to other thermoelectric materials. Post-deposition sintering of $La_{3-x}Te_4$ EPD films is presented in Chapter 4.

3.12 References

(1) Chen, X.; Dai, W.; Wu, T.; Luo, W.; Yang, J.; Jiang, W.; Wang, L. Thin Film Thermoelectric Materials: Classification, Characterization, and Potential for Wearable Applications. *Coatings 2018, Vol. 8, Page 244* **2018**, *8* (7), 244. https://doi.org/10.3390/COATINGS8070244.

(2) Chen, X.; Zhou, Z.; Lin, Y. H.; Nan, C. Thermoelectric Thin Films: Promising Strategies and Related Mechanism on Boosting Energy Conversion Performance. *Journal of Materiomics* **2020**, *6* (3), 494–512. https://doi.org/10.1016/J.JMAT.2020.02.008.

(3) Gayner, C.; Kar, K. K. Recent Advances in Thermoelectric Materials. *Prog Mater Sci* **2016**, *83*, 330–382. https://doi.org/10.1016/J.PMATSCI.2016.07.002.

(4) Snyder, G. J.; Toberer, E. S. Complex Thermoelectric Materials. *Nature Materials 2008 7:2* **2008**, *7* (2), 105–114. https://doi.org/10.1038/nmat2090.

(5) Dresselhaus, M. S.; Chen, G.; Tang, M. Y.; Yang, R.; Lee, H.; Wang, D.; Ren, Z.; Fleurial, J. P.; Gogna, P. New Directions for Low-Dimensional Thermoelectric Materials. *Advanced Materials* **2007**, *19* (8), 1043–1053. https://doi.org/10.1002/ADMA.200600527.

(6) Xiao, F.; Hangarter, C.; Yoo, B.; Rheem, Y.; Lee, K. H.; Myung, N. V. Recent Progress in Electrodeposition of Thermoelectric Thin Films and Nanostructures. *Electrochim Acta* **2008**, *53* (28), 8103–8117. https://doi.org/10.1016/J.ELECTACTA.2008.06.015.

(7) Chi, S. C.; Farias, S. L.; Cammarata, R. C. A Novel Approach to Synthesize Lanthanum Telluride Thermoelectric Thin Films in Ambient Conditions. *Materials Research Society Symposium Proceedings* **2013**, *1543* (1), 113–118. https://doi.org/10.1557/OPL.2013.929/METRICS.

(8) Delaire, O.; May, A. F.; Mcguire, M. A.; Porter, W. D.; Lucas, M. S.; Stone, M. B.; Abernathy, D. L.; Ravi, V. A.; Firdosy, S. A.; Snyder, G. J. Phonon Density of States and Heat Capacity of La 3−x Te 4. https://doi.org/10.1103/PhysRevB.80.184302.

(9) Cheikh, D. Synthesis and Characterization of Rare-Earth Tellurides and Their Composites for High-Temperature Thermoelectric Applications, UCLA, Los Angeles, 2017.

(10) Chi, S. chih. Novel Syntheses of Thermoelectric and Nanostructured Materials and a System for Purifying and Sorting Metallic and Semiconducting Single Walled Carbon Nanotubes in a Mixed Tube Suspension, Johns Hopkins, 2014. https://jscholarship.library.jhu.edu/handle/1774.2/37038 (accessed 2023-04-05).

(11) Talebi, T.; Ghomashchi, R.; Talemi, P.; Aminorroaya, S. Suspension Characteristics and Electrophoretic Deposition of p -Type Bi 2 Te 3 Films for Thermoelectric Applications . *J Electrochem Soc* **2018**, *165* (9), D364–D369. https://doi.org/10.1149/2.0301809JES/XML.

(12) Yoo, I. J.; Myung, N. V.; Lim, D. C.; Song, Y.; Jeong, Y. K.; Kim, Y. Do; Lee, K. H.; Lim, J. H. Electrodeposition of BixTey Thin Films for Thermoelectric Application. *Thin Solid Films* **2013**, *546*, 48–52. https://doi.org/10.1016/J.TSF.2013.05.036.

(13) Abegunde, O. O.; Akinlabi, E. T.; Oladijo, O. P.; Akinlabi, S.; Ude, A. U.; Abegunde, O. O.; Akinlabi, E. T.; Oladijo, O. P.; Akinlabi, S.; Ude, A. U. Overview of Thin Film Deposition Techniques. *AIMS Materials Science 2019 2:174* **2019**, *6* (2), 174–199. https://doi.org/10.3934/MATERSCI.2019.2.174.

(14) Bourbos, E.; Giannopoulou, I.; Karantonis, A.; Paspaliaris, I.; Panias, D. Electrodeposition of Rare Earth Metals from Ionic Liquids. *Rare Earths Industry: Technological, Economic, and Environmental Implications* **2016**, 199–207. https://doi.org/10.1016/B978-0-12-802328-0.00013-9.

(15) Zhou, J.; Meng, X.; Zhang, R.; Liu, H.; Liu, Z. Progress on Electrodeposition of Rare Earth Metals and Their Alloys. *Electrocatalysis* **2021**, *12* (6), 628–640. https://doi.org/10.1007/S12678-021-00688-1/TABLES/3.

(16) Legeai, S.; Diliberto, S.; Stein, N.; Boulanger, C.; Estager, J.; Papaiconomou, N.; Draye, M. Room-Temperature Ionic Liquid for Lanthanum Electrodeposition. *Electrochem commun* **2008**, *10* (11), 1661–1664. https://doi.org/10.1016/J.ELECOM.2008.08.005.

(17) Okamoto, T.; Horii, S.; Uchikoshi, T.; Suzuki, T. S.; Sakka, Y.; Funahashi, R.; Ando, N.; Sakurai, M.; Shimoyama, J. I.; Kishio, K. Fabrication of Multilayered Oxide Thermoelectric Modules by Electrophoretic Deposition under High Magnetic Fields. *Appl Phys Lett* **2006**, *89* (8), 81912. https://doi.org/10.1063/1.2338749/165753.

(18) Nozariasbmarz, A.; Tahmasbi Rad, A.; Zamanipour, Z.; Krasinski, J. S.; Tayebi, L.; Vashaee, D. Enhancement of Thermoelectric Power Factor of Silicon Germanium Films Grown by Electrophoresis Deposition. *Scr Mater* **2013**, *69* (7), 549–552. https://doi.org/10.1016/J.SCRIPTAMAT.2013.06.025.

(19) Amrollahi, P.; Krasinski, J. S.; Vaidyanathan, R.; Tayebi, L.; Vashaee, D. Electrophoretic Deposition (EPD): Fundamentals and Applications from Nano- to Micro-Scale Structures. *Handbook of Nanoelectrochemistry* **2015**, 1–27. https://doi.org/10.1007/978-3-319-15207-3_7-1.

(20) Besra, L.; Liu, M. A Review on Fundamentals and Applications of Electrophoretic Deposition (EPD). *Prog Mater Sci* **2007**, *52* (1), 1–61. https://doi.org/10.1016/J.PMATSCI.2006.07.001.

(21) Van Der Biest, O. O.; Vandeperre, L. J. ELECTROPHORETIC DEPOSITION OF MATERIALS. *https://doi.org/10.1146/annurev.matsci.29.1.327* **2003**, *29*, 327–352. https://doi.org/10.1146/ANNUREV.MATSCI.29.1.327.

(22) Sarkar, P.; Nicholson, P. S. Electrophoretic Deposition (EPD): Mechanisms, Kinetics, and Application to Ceramics. *Journal of the American Ceramic Society* **1996**, *79* (8), 1987–2002. https://doi.org/10.1111/J.1151-2916.1996.TB08929.X.

(23) Raja, P. M. V.; Barron, A. R. Zeta Potential Analysis. In *Physical Methods in Chemistry and Nanoscience*; 2023.

(24) Koelmans, H.; Overbeek, J. T. G. Stability and Electrophoretic Deposition of Suspensions in Non-Aqueous Media. *Discuss Faraday Soc* **1954**, *18* (0), 52–63. https://doi.org/10.1039/DF9541800052.

(25) Wiersema, P. H.; Loeb, A. L.; Overbeek, J. T. G. Calculation of the Electrophoretic Mobility of a Spherical Colloid Particle. *J Colloid Interface Sci* **1966**, *22* (1), 78–99. https://doi.org/10.1016/0021-9797(66)90069-5.

(26) Williams, D. J. A.; Williams, K. P. Electrophoresis and Zeta Potential of Kaolinite. *J Colloid Interface Sci* **1978**, *65* (1), 79–87. https://doi.org/10.1016/0021-9797(78)90260-6.

(27) Zhitomirsky, I.; Gal-Or, L. Electrophoretic Deposition of Hydroxyapatite. *J Mater Sci Mater Med* **1997**, *8* (4), 213–219. https://doi.org/10.1023/A:1018587623231.

(28) May, A. F.; Fleurial, J. P.; Snyder, G. J. Thermoelectric Performance of Lanthanum Telluride Produced via Mechanical Alloying. *Phys Rev B Condens Matter Mater Phys* **2008**, *78* (12), 125205. https://doi.org/10.1103/PHYSREVB.78.125205/FIGURES/11/MEDIUM.

(29) May, A. High-Temperature Transport in Lanthanum Telluride and Other Modern Thermoelectric Materials, California Institute of Technology, Pasadena, 2010.

(30) Ma, J. Improving the Mechanical Strength and Power Conversion Efficiency of High Temperature Thermoelectrics, UCLA, Los Angeles, 2014.

(31) Anné, G.; Neirinck, B.; Vanmeensel, K.; Van Der Biest, O.; Vleugels, J.; Leuven, K. U. Throwing Power during Electrophoretic Deposition. **2006**. https://doi.org/10.4028/www.scientific.net/KEM.314.187.

(32) Gorbunov, A. O.; Tsyrul'nikov, N. A.; Tikhomirova, A. A.; Bogachev, N. A.; Skripkin, M. Y.; Nikolskii, A. B.; Pestova, O. N. Solubility of D-Element Salts in Organic and Aqueous–Organic Solvents: II. Effect of Halocomplex Formation on Solubility of Cobalt Bromide and Chloride and Nickel Chloride. *Russ J Gen Chem* **2016**, *86* (4), 771–777. https://doi.org/10.1134/S1070363216040022/METRICS.

(33) Neuróhr, K.; Pogány, L.; Tóth, B. G.; Révész, Á.; Bakonyi, I.; Péter, L. Electrodeposition of Ni from Various Non-Aqueous Media: The Case of Alcoholic Solutions. *J Electrochem Soc* **2015**, *162* (7), D256–D264. https://doi.org/10.1149/2.0381507JES/XML.

(34) Lau, K.-T.; Sorrell, C. C. Effect of Charging Agents on Electrophoretic Deposition of Titanium Particles. *Journal of The Australian Ceramic Society* **2013**, *49* (2), 104–112.

(35) Luo, K.; Shi, N.; Cong, H.; Sun, C. Electrophoretic Deposition of Nickel, Iron and Aluminum Nanoparticles on Carbon Fibers. *Journal of Solid State Electrochemistry* **2006**, *10* (12), 1003–1007. https://doi.org/10.1007/S10008-005-0044-4/FIGURES/3.

(36) Wang, C.; Ma, J.; Cheng, W.; Zhang, R. Thick Hydroxyapatite Coatings by Electrophoretic Deposition. *Mater Lett* **2002**, *57* (1), 99–105. https://doi.org/10.1016/S0167-577X(02)00706-1.

(37) *Tetrahydrofuran | Fisher Scientific*. https://www.fishersci.com/us/en/scientific-products/selection-guides/chemicals/tetrahydrofuran.html (accessed 2023-05-03).

(38) Labib, M. E.; Williams, R. An Experimental Comparison between the Aqueous PH Scale and the Electron Donicity Scale. *Colloid Polym Sci* **1986**, *264* (6), 533–541. https://doi.org/10.1007/BF01422007/METRICS.

(39) Gritzner, G.; Sperker, S. Donor and Acceptor Properties of the Solvents Tetrahydrofuran and Tetrahydrothiophene. *J Solution Chem* **1988**, *17* (12), 1133–1144. https://doi.org/10.1007/BF00662924/METRICS.

(40) Zhou, X.; Vovk, E. I.; Liu, Y.; Guan, C.; Yang, Y. An In Situ Temperature-Dependent Study of La2O3 Reactivation Process. *Front Chem* **2021**, *9*, 373. https://doi.org/10.3389/FCHEM.2021.694559/BIBTEX.

(41) Yan, X.; Ji, Q.; Wang, C.; Xu, J.; Wang, L. In Situ Construction Bismuth Oxycarbonate/Bismuth Oxybromide Z-Scheme Heterojunction for Efficient Photocatalytic Removal of Tetracycline and Ciprofloxacin. *J Colloid Interface Sci* **2021**, *587*, 820–830. https://doi.org/10.1016/J.JCIS.2020.11.043.

Chapter 4 Ultrafast High Temperature Sintering (UHS) of $La_{3-x}Te_4$

4.1 Background on Sintering and Considerations for $La_{3-x}Te_4$

Though EPD produces uniform $La_{3-x}Te_4$ coatings with a good green density ~65%, the films are composed of individual particles that are weakly bonded by Van der Waals forces. Post-deposition sintering is necessary to improve bonding and reduce porosity in the film (Figure 4.1) since electron scattering at particle/particle or particle/pore interfaces will negatively impact electronic conduction.[1] Ideally, the films should attain >90% theoretical density for comparable densification to bulk $La_{3-x}Te_4$ pellets sintered via hot pressing or spark plasma sintering.[2–4]

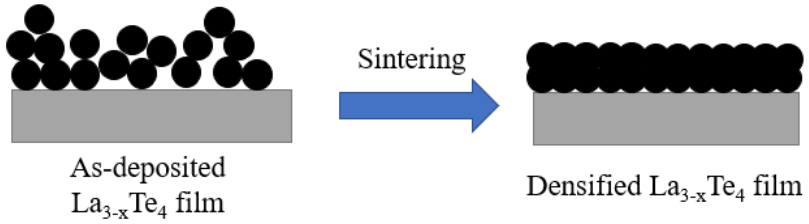

Figure 4.1: Illustration of sintering to densify as-deposited $La_{3-x}Te_4$ films.

Sintering is a solid-state process during which the formed green body is heat treated to temperatures approaching, but below, the melting point to promote densification of the powder into a compacted body.[5–7] The driving force for sintering is a reduction in free energy caused by the replacement of higher-energy particle surface area with lower-energy grain boundary area.[6,7] In addition to densification, coarsening also occurs during sintering heat treatments and is driven by differences in curvature at grain boundaries due to differences in grain size.[6,8] Since the surface-area-to-volume ratio decreases with increasing particle size, the driving force for sintering is maximized when particles have small radii.[8] Coarsening prior to sintering, which leads to an increase in particle/grain size, is undesirable because it decreases the driving force for sintering.

The initial stages of sintering (Figure 4.2) begin through the formation of sinter bonds (or necks) between particles. As intermediate stages of sintering are reached, pores rearrange to form a network at grain boundaries and, during final stages of sintering, rapid grain growth occurs via coarsening.[6] The most common mass transport mechanisms are surface diffusion and grain boundary diffusion, though bulk lattice diffusion may also occur.[6–9] In general, surface diffusion produces coarsening without densification since it is not effective in producing pore shrinkage, whereas grain boundary diffusion leads to densification via neck growth and pore migration to the surface.[6,7] Bulk lattice diffusion also enables densification, though its contribution is usually less than that of grain boundary diffusion due to its higher activation energy and slower kinetics. Since surface diffusion usually has a low activation energy and fast kinetics, coarsening is inherent during sintering.[6] An appropriate heat treatment for sintering is therefore one that minimizes coarsening prior to sintering in order to avoid its negative impact on the driving force for densification.

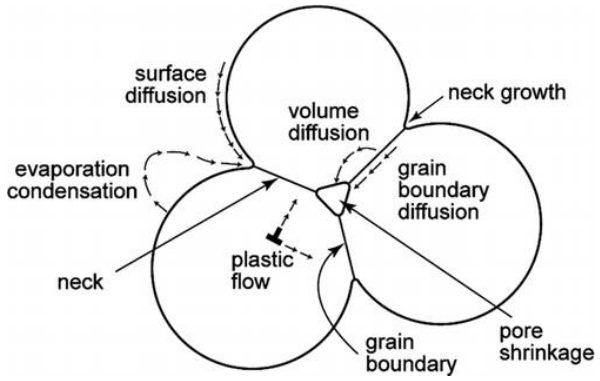

Figure 4.2 (reprinted from German [6]): Illustration of mass transport mechanisms between three particles during sintering. Sintering leads to densification via the formation of sinter bonds (or necks) and pore shrinkage.

In addition to determining appropriate sintering conditions, a materials challenge for densifying $La_{3-x}Te_4$ films is that sintering temperatures must exceed 1000°C due to the high melting temperature of $La_{3-x}Te_4$ [2,10]. However, the oxidation study presented in Chapter 2

indicates that oxidation of the material can occur <600ºC even with limited oxygen exposure, so avoiding oxidation during sintering is a primary concern. In the literature, conventional furnace heat treatments are often employed for post-deposition sintering of EPD films[11–13], but such heat treatments are not well-suited for processing $La_{3-x}Te_4$ since they require long exposure to high temperatures and have difficulty in reliably maintaining a sufficiently low oxygen concentration.

Hot pressing and spark plasma sintering are well-established for producing dense compacts of bulk $La_{3-x}Te_4$ with minimal oxidation[2–4], but require the use of specialized equipment with complicated sample loading procedures. Additionally, they may encounter difficulties densifying films on a substrate, particularly for more complex geometries, due to uniaxial pressure exerted during heat treatment. It is therefore desirable to expand the processability of $La_{3-x}Te_4$ by developing sintering techniques which achieve high theoretical density and minimize sample oxidation without the use of complex equipment. Doing so will reduce fabrication cost, time, and complexity, and allow for synthesis of additional $La_{3-x}Te_4$ geometries with high density for optimum thermoelectric performance.

4.2 Introduction to Ultrafast High-Temperature Sintering (UHS)

Recently, Wang *et al* developed a sintering technique termed ultrafast high-temperature sintering (UHS) which has been demonstrated to sinter bulk refractory ceramics in a matter of seconds.[14] The UHS setup is simple, making use of resistive carbon paper heating strips and an external power source. The applied current causes rapid Joule-heating of the carbon paper which enables temperature control up to 3000ºC and heating rates up to 10^4 ºC/min.[14] Furthermore, UHS is easily configured for use inside a glovebox so that heat treatments can be performed in high-purity inert atmospheres. This technique is attractive for sintering $La_{3-x}Te_4$ because of the simple equipment involved and ability to heat treat samples quickly in an inert atmosphere.

Additionally, UHS has been used to sinter complex three-dimensional samples[14] which is applicable to $La_{3-x}Te_4$ coatings on non-uniform substrates.

In this chapter, UHS is employed to sinter both $La_{3-x}Te_4$ films and pellets in seconds. The effects of sintering time and temperature on microstructure are characterized and the mechanisms of rapid densification and grain growth are studied. The technique is versatile and readily applied to densify both $La_{3-x}Te_4$ EPD films and bulk pellets. Initial stages of sintering are controlled by surface diffusion while later stages are controlled by grain boundary diffusion. Rapid densification results from the high heating rate achieved by UHS which minimizes low-temperature coarsening and maintains a high driving force for densification.

4.3 Experimental Methods

EPD films were synthesized as described in Chapter 3. For all EPD samples presented in this chapter, the solvent was THF and deposition voltage, time, and particle concentration were 100 V, 10 min, and 10 mg/mL, respectively. All $La_{3-x}Te_4$ pellets presented in this chapter were prepared by loading as-synthesized $La_{3-x}Te_4$ powder into a stainless-steel pellet die and cold-pressing at 1000 psi. Pellets had a thickness of 1 mm and diameter of 1 cm.

Figure 4.3 shows the UHS configuration for sintering of EPD $La_{3-x}Te_4$ films and cold-pressed $La_{3-x}Te_4$ pellets. The samples were placed between two parallel carbon paper heating elements with the sample resting on the bottom one. A small gap was maintained between the sample and the top carbon paper strip to maintain appropriate resistive heating of the carbon paper and prevent electrical current from passing through the sample itself.

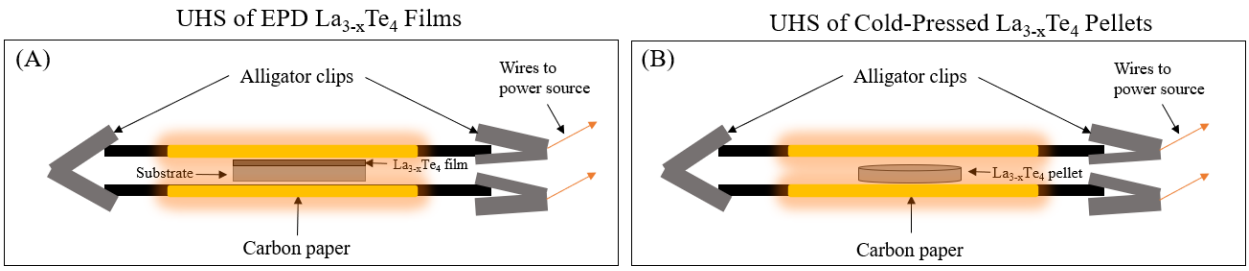

Figure 4.3: Illustration of the side view of the UHS configuration for sintering of (A) EPD $La_{3-x}Te_4$ films and (B) cold-pressed $La_{3-x}Te_4$ pellets. In both cases, the sample is placed between the Joule-heating carbon paper strips and rests on the bottom one. A small gap between the sample and the top carbon paper strip ensures that electrical current does not pass through the sample itself, which would short the carbon paper strips together and prevent appropriate heating.

All UHS heat treatments were performed in a custom-fabricated chamber inside an Ar-filled glovebox. This minimizes potential oxygen exposure by allowing for direct loading of samples after preparation without transfer outside of the glovebox. The chamber was evacuated and refilled with ultra-high purity (UHP) argon several times prior to sintering. A constant flow of UHP argon was maintained during sintering. Strips of Ti or Zr metal were also added to the chamber as O_2 getters to further minimize oxygen.

The temperature of the UHS heating elements was controlled by the applied current and electrical resistance of the carbon paper. The current/temperature relationship was calibrated by measuring the temperature with a Digi-Sense high-temperature infrared thermometer. The general applied current vs. time profile for UHS heat treatments is shown in Figure 4.4. The applied current was rapidly increased to the value associated with the sintering/dwell temperature, held for the sintering/dwell time, then rapidly reduced to zero. The sample was allowed to cool prior to removal from the UHS chamber.

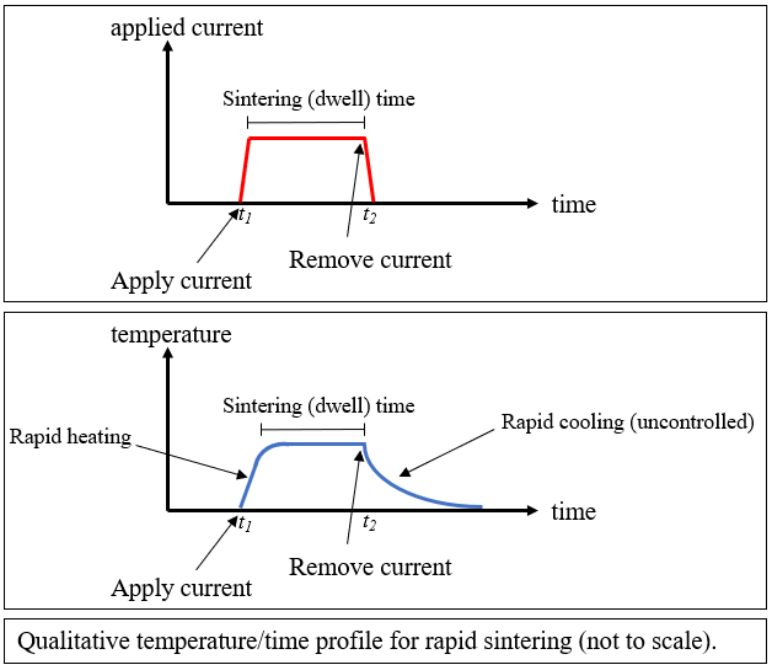

Figure 4.4: General applied current vs. time profile and temperature vs. time profile for UHS heat treatments (not to scale). For the listed sintering parameters for a given sample, temperature refers to the temperature associated with the dwell current, and time refers to the length of time for which the dwell current was maintained. The dwell current/temperature were typically achieved within 10-60 seconds.

4.4 UHS of EPD $La_{3-x}Te_4$ Films and Coatings

Figure 4.5 and Figure 4.6 show SEM images for UHS $La_{3-x}Te_4$ samples. Sintered planar EPD films are shown in Figure 4.5A-F and a sintered bulk pellet is shown in Figure 4.5G-H. Sintered non-planar EPD coatings are shown in Figure 4.6. All samples achieve significant densification with distinct grain structures and a reduction in porosity to <15% (Table 4.1). The sintered EPD samples have an average grain size in the range of about 0.8-1.8 µm while the sintered bulk pellet has an average grain size of about 2.4 µm. The smaller grain size for the sintered EPD films compared to that of the pellet might be caused by the EPD films being constrained by the substrate as they densify, which partially limits grain growth.

Significant cracking is observed in the EPD samples for which grafoil (Figure 4.5C) and boron nitride (Figure 4.5E) are the substrate material. Since this cracking is absent when Ni is the substrate material (Figure 4.5A and Figure 4.6), the primary cause of cracking is likely mismatch

in the coefficient of thermal expansion (CTE) between $La_{3-x}Te_4$ and the substrate material (Table 4.2). $La_{3-x}Te_4$ and Ni have similar CTE values while those of grafoil and boron nitride are significantly different. Cracking is somewhat less prevalent when boron nitride is the substrate material compared to grafoil which is likely due to the slightly larger CTE of boron nitride.

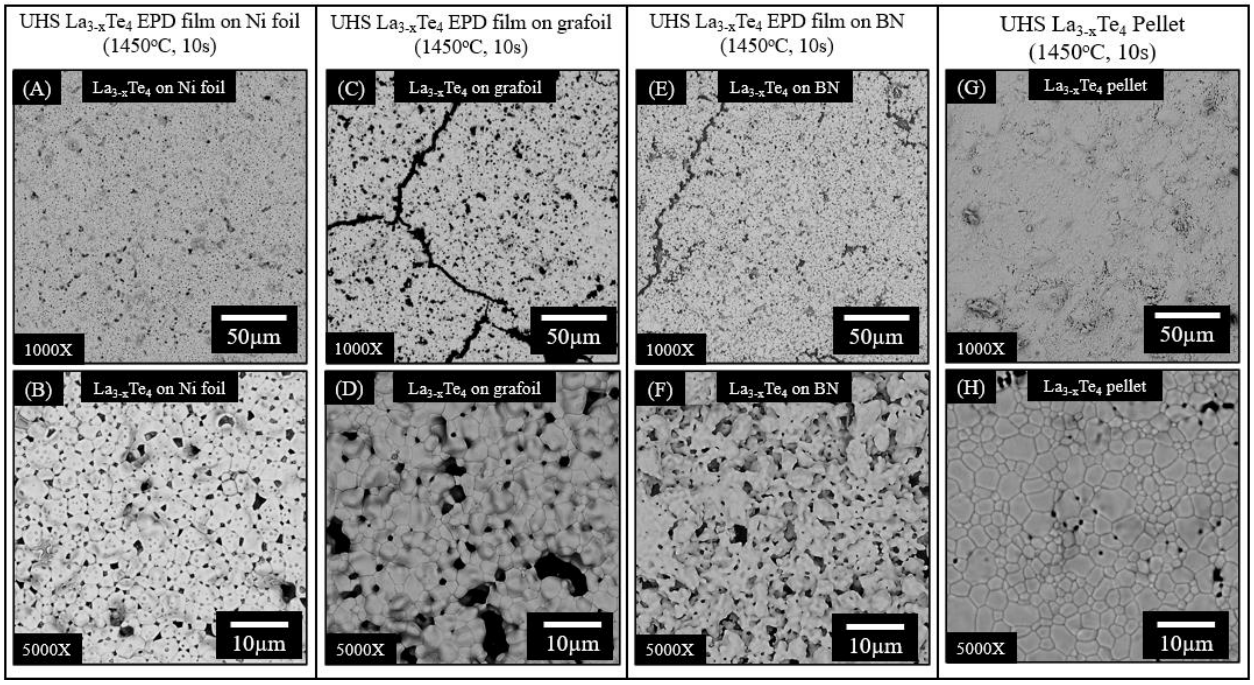

Figure 4.5: SEM images of UHS $La_{3-x}Te_4$ samples. (A, B) EPD $La_{3-x}Te_4$ film on Ni foil, (C, D) EPD $La_{3-x}Te_4$ film on grafoil,(E, F) EPD $La_{3-x}Te_4$ film on boron nitride. (G, H) cold-pressed $La_{3-x}Te_4$ pellet. All samples were sintered at 1450°C for 10 seconds in flowing Ar atmosphere.

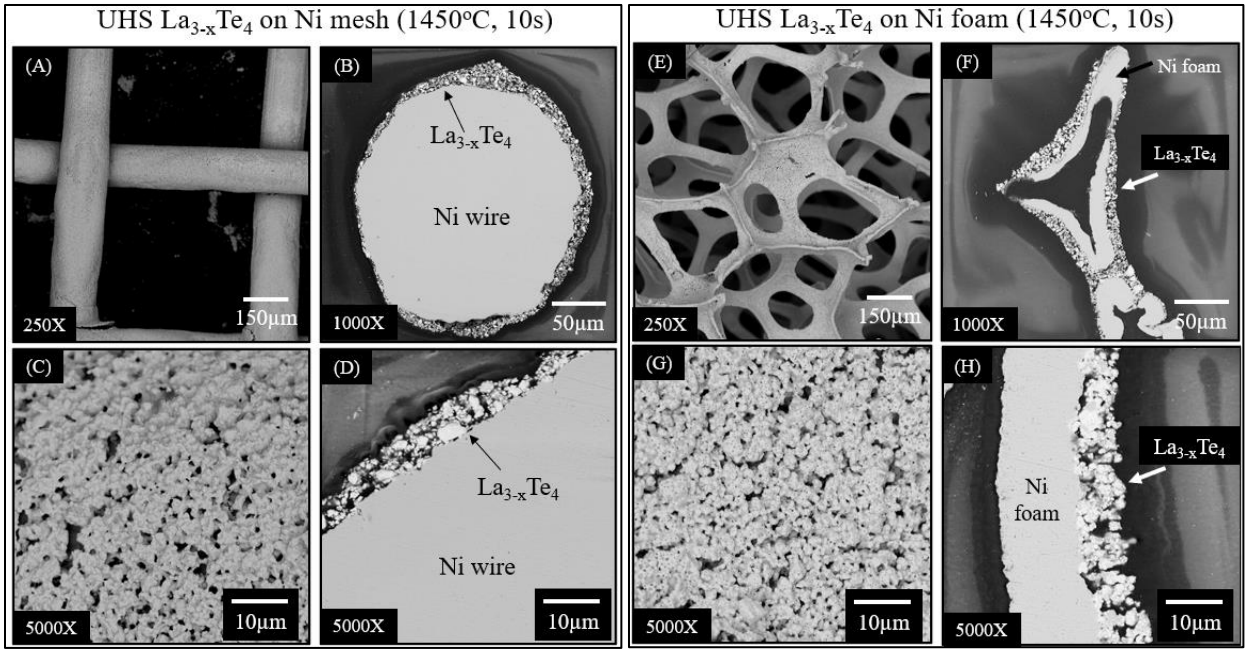

Figure 4.6: SEM images of UHS $La_{3-x}Te_4$ coatings on non-planar substrates. (A-D) $La_{3-x}Te_4$ on Ni mesh. (E-H) $La_{3-x}Te_4$ on Ni foam. Both samples were sintered at 1450°C for 10 seconds in flowing Ar atmosphere.

Table 4.1: Average grain size and porosity for UHS $La_{3-x}Te_4$ samples.

Sample (sintered at 1450°C, 10s)	**Average grain size**	**Porosity**
UHS $La_{3-x}Te_4$ EPD film on Ni foil	1.76 µm	9.6% (ImageJ analysis)
UHS $La_{3-x}Te_4$ EPD film on grafoil	1.63 µm	10.1% (ImageJ analysis)
UHS $La_{3-x}Te_4$ EPD film on BN	1.21 µm	13.2% (ImageJ analysis)
UHS $La_{3-x}Te_4$ pellet	2.44 µm	7.4% (Archimedes method)
UHS $La_{3-x}Te_4$ EPD film on Ni mesh	0.833 µm	14.6% (ImageJ analysis)
UHS $La_{3-x}Te_4$ EPD film on Ni foam	0.860 µm	12.6% (ImageJ analysis)

Table 4.2: CTE comparison of $La_{3-x}Te_4$ with different substrate materials used for EPD films.

Material	Cracking of sintered $La_{3-x}Te_4$ EPD coating?	CTE (>800K) (reference)
$La_{3-x}Te_4$	N/A	12-16 x 10^{-6} K^{-1} ([15])

Ni	No	13 x 10^{-6} K^{-1} ([16])
Grafoil	Yes	0.9 x 10^{-6} K^{-1} ([17])
Boron nitride	Yes	1-2.5 x 10^{-6} K^{-1} ([18])

XRD scans for the UHS $La_{3-x}Te_4$ samples (Figure 4.7) indicate a high degree of phase purity with minimal oxidation. For the EPD samples, films on grafoil or boron nitride exhibited minimal oxidation which suggests that these substrate materials may mitigate oxidation by functioning as effective oxygen getters or reducing agents for any oxides that form. Regardless, these results establish UHS as an effective sintering method for producing dense $La_{3-x}Te_4$ EPD films, non-planar coatings, and bulk pellets with minimal oxidation in as little as 10 seconds. The samples achieve >85% theoretical density which is comparable to bulk $La_{3-x}Te_4$ processed via hot pressing or spark plasma sintering in the literature. Furthermore, this is the first demonstration of pressure-less sintering of $La_{3-x}Te_4$. This achievement is significant since it establishes that pressure sintering techniques such as hot pressing and spark plasma sintering are not required for densification of the material.

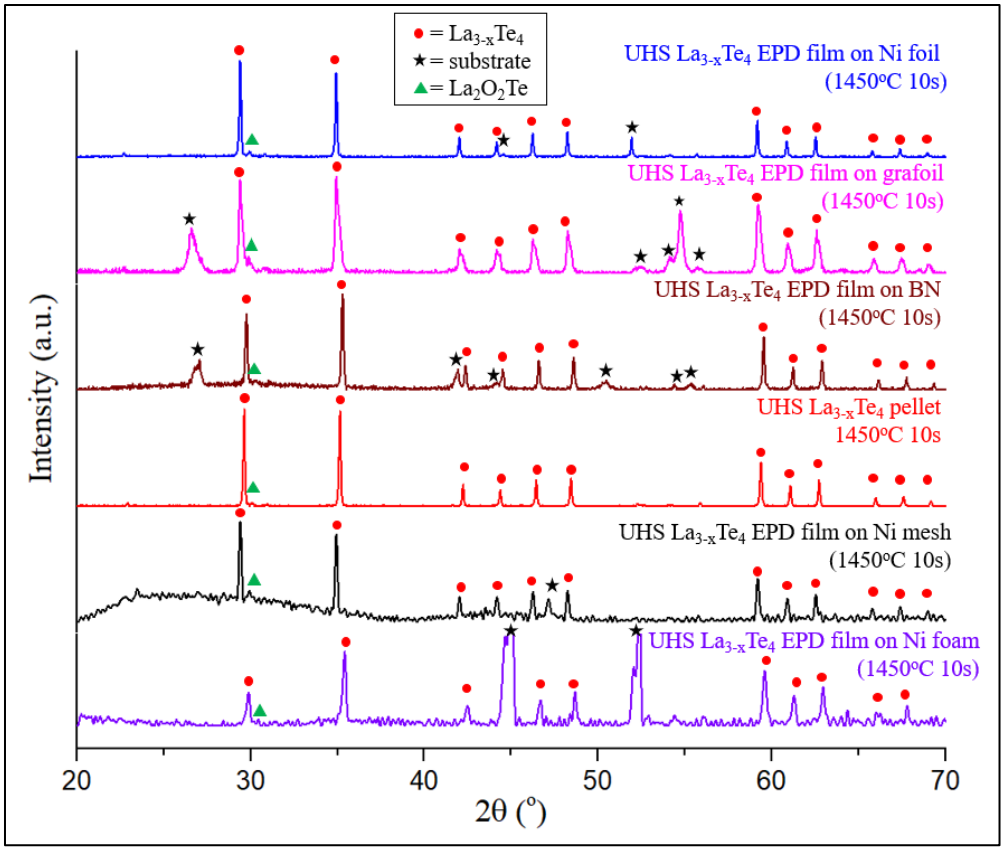

Figure 4.7: XRD scans for UHS $La_{3-x}Te_4$ samples. All samples were sintered at 1450°C for 10 seconds in flowing Ar atmosphere. The angle of the strongest La_2O_2Te peak (~30.5°) is marked with the triangle symbol and is very weak or absent for all samples indicating minimal oxidation after sintering.

4.5 Effect of UHS Parameters on $La_{3-x}Te_4$ Microstructure

The effect of sintering temperature (Figure 4.8) and time (Figure 4.9) on grain size and porosity were characterized to establish the relationship between UHS parameters and $La_{3-x}Te_4$ microstructure. These analyses were performed for UHS $La_{3-x}Te_4$ EPD films on grafoil substrate since grafoil provided the best reproducibility for obtaining sintered films with minimal oxidation and the local microstructure was not affected by cracking in the film. When sintering temperature is increased at constant sintering time (Figure 4.8), there is primarily particle coarsening without densification when the temperature is ≤1050°C. Sinter necks begin to form at 1150°C which indicates the onset of initial stages of sintering. Homogenization of the microstructure occurs at 1250°C as more sinter necks form and grains become rounded and

equiaxed. Intermediate stages of sintering are reached at 1350°C as sinter necks are replaced by distinct grain boundaries accompanied by a more significant increase in density and grain size. The final stages of sintering occur at 1450°C as indicated by a dramatic increase in grain size and reduction in porosity which result in a dense, large-grained microstructure.

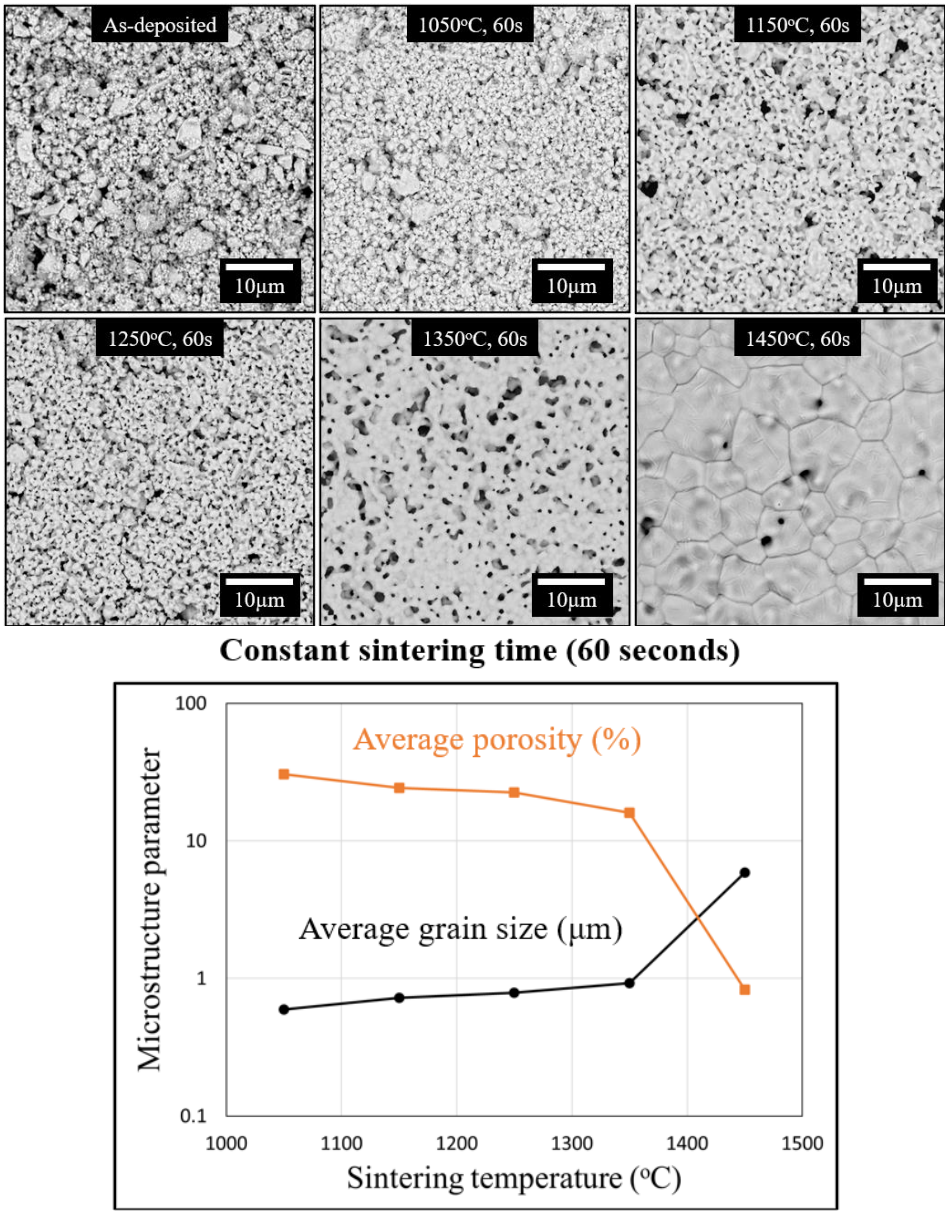

Figure 4.8: SEM images of $La_{3-x}Te_4$ EPD films on grafoil substrate showing the microstructure evolution as a function of UHS sintering temperature at a constant sintering time of 60 seconds. All heat treatments were performed in flowing Ar atmosphere. All images are at 5000X magnification. The graph plots average grain size and porosity (obtained from the SEM images) as a function of sintering temperature.

The results of the temperature-dependent UHS study (Figure 4.8) indicate that the initial, intermediate, and final stages of sintering occur between 1250-1450ºC for the heat treatment times employed. Therefore, the UHS microstructure evolution as a function of time was characterized at 1250ºC, 1350ºC, and 1450ºC (Figure 4.9). At 1250ºC, initial stages of sintering are apparent for times ≤60 seconds where there is sinter neck formation, slight grain growth, and minimal reduction in porosity. A transition to intermediate stages of sintering occurs for times >60 seconds as sinter necks are replaced by distinct grain boundaries with additional reduction in porosity. Similar behavior is observed at 1350ºC, though the transition from initial to intermediate stages of sintering occurs earlier at ~30 seconds. Furthermore, the dense structure at 180 seconds is similar to microstructures obtained at 1450ºC and indicates a transition to final stages of sintering. At 1450ºC, intermediate and final stages of sintering are achieved as early as 10 seconds as indicated by distinct grain boundaries and significant densification. Simultaneous coarsening and reduction in porosity occur rapidly as sintering time increases until very dense, large-grained structures are achieved at times ≥60 seconds.

It is clear from these results that both UHS time and temperature have a significant impact on the microstructure of sintered $La_{3-x}Te_4$ films. For the short time scale of UHS heat treatments, temperatures ≤1050ºC lead to particle coarsening without densification. As temperature increases to 1150-1250ºC, densification initiates with the formation of sinter necks and progresses with the formation of grain boundaries and elimination of porosity as sintering time increases. Sintering kinetics are enhanced as temperature increases to 1350ºC, with an earlier transition from sinter neck formation to densification and grain growth. At 1450ºC, sintering kinetics are so rapid that the final stages of sintering occur almost immediately with extremely fast densification and grain growth. A remarkable feature of UHS is its ability to

densify $La_{3-x}Te_4$ in less than 1 minute via pressure-less sintering. An analysis of the grain growth and sintering mechanisms is provided in the next section to develop an understanding of the mechanisms underlying rapid densification.

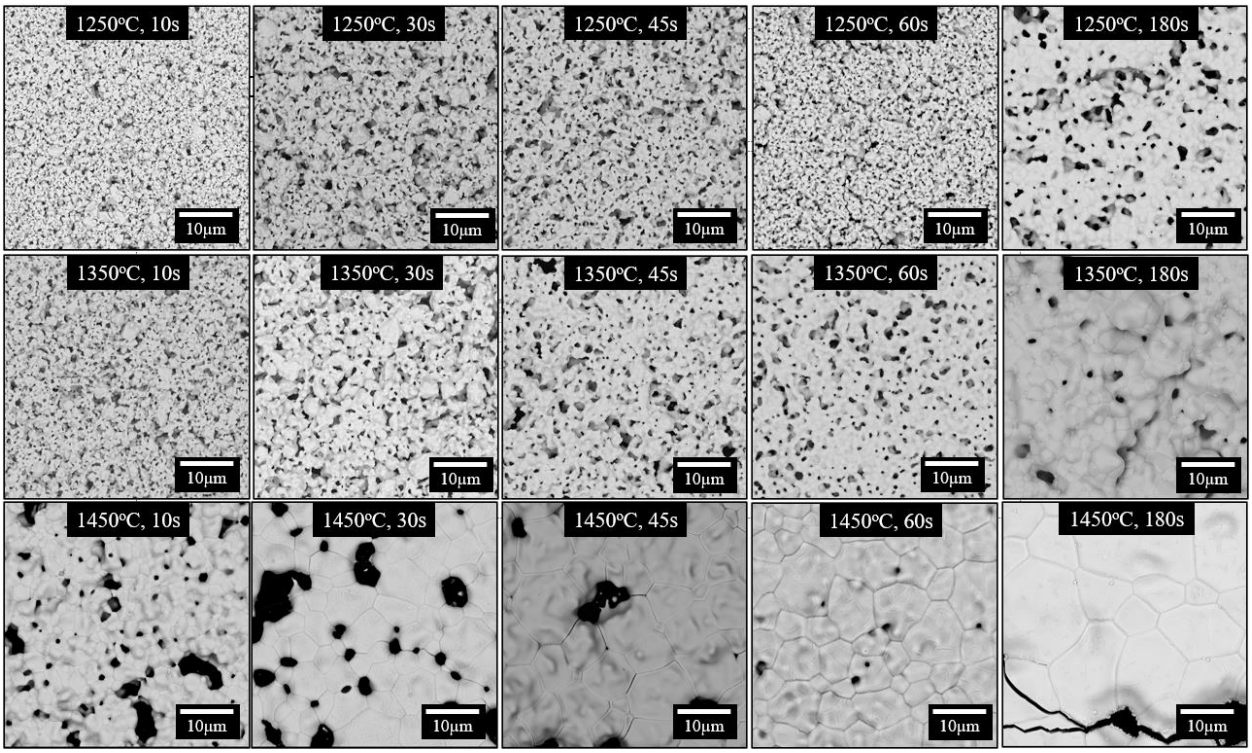

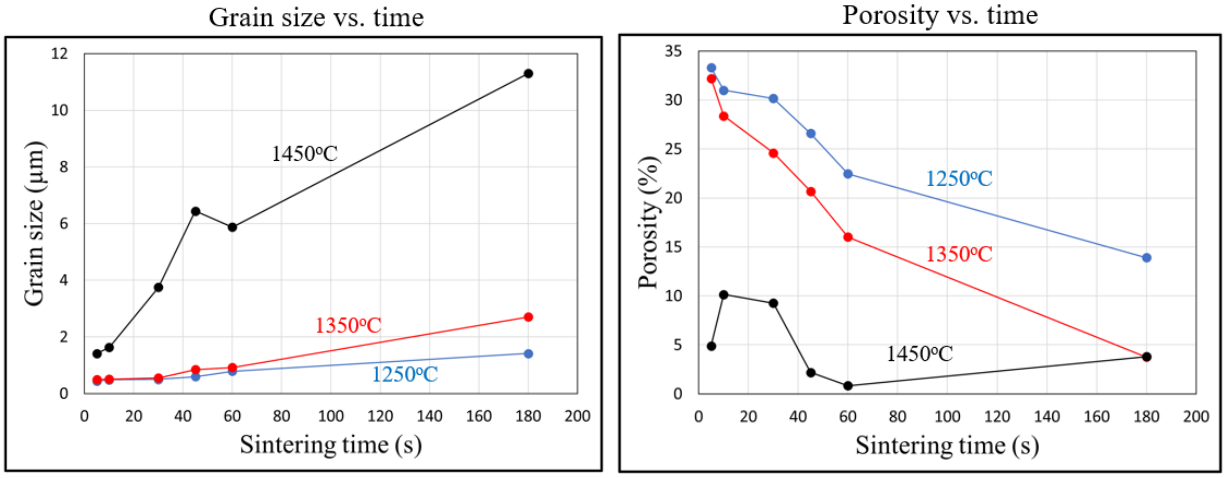

Figure 4.9: SEM images of $La_{3-x}Te_4$ EPD films on grafoil substrate showing the microstructure evolution as a function of UHS parameters (sintering temperature and time). All heat treatments were performed in flowing Ar atmosphere. All images are at 5000X magnification. The graphs plot average grain size and porosity (obtained from the SEM images) as a function of sintering time and temperature.

4.6 Analysis of Grain Growth Kinetics and Activation Energy

Given the unique ability of UHS to sinter $La_{3-x}Te_4$ in seconds, the mechanisms underlying its rapid sintering kinetics and their relationship to UHS parameters are of fundamental interest. A quantitative analysis of the kinetics and activation energies of grain growth was performed to characterize the mechanisms of extremely fast densification that occur during UHS. In the literature, grain growth is modeled by a power-law relationship[8,9]:

$$G^n - G_0^n = kt \qquad \text{(Equation 4.1)}$$

where G is average grain size, G_0 is the average starting grain size of the material, n is the grain growth exponent, k is the grain growth rate constant, and t is time.

The grain growth rate constant, k, varies with temperature via an Arrhenius relationship[8]:

$$k = k_0 e^{-Q/RT} \qquad \text{(Equation 4.2)}$$

where k is the grain growth rate constant, k_0 is a pre-exponential constant, Q is the activation energy for grain boundary migration, R is the ideal gas constant, and T is temperature.

In (Equation 3.3, the grain growth exponent, n, provides information on the diffusion mechanisms responsible for grain growth and is typically assigned an idealized integer value for the related mechanism, though experimental values are usually not exact integers.[8,19,20] Most often, $n = 2$ corresponds to grain boundary diffusion and $n = 3$ corresponds to bulk lattice diffusion.[9] Many researchers have found that experimental values of n sometimes exceed these values, with $n = 4$ and $n = 5$ being reported.[19–23] Both $n = 4$ and $n = 5$ are associated with surface diffusion-controlled grain growth, though a value of $n = 5$ can suggest that grain growth is hindered due to pores or precipitates pinning grain boundaries.[19–23] Therefore, experimental determination of the grain growth exponent can help identify the dominant diffusion mechanism controlling grain growth.

Figure 4.10 plots ln (*G*) vs ln (*t*) at different temperatures for UHS $La_{3-x}Te_4$ EPD films on grafoil substrate. The slope of the line is equal to the reciprocal of the grain growth exponent which allows for determination of the grain growth exponent from a linear fit to the data. For 1250ºC and 1350ºC (Figure 4.10A and B), the data is best fit with two lines where the first one encompasses the first four data points (5-45 seconds) and the second encompasses the last four data points (30-180 seconds). The data for 1450ºC (Figure 4.10C) is best fit with a single line for all data points.

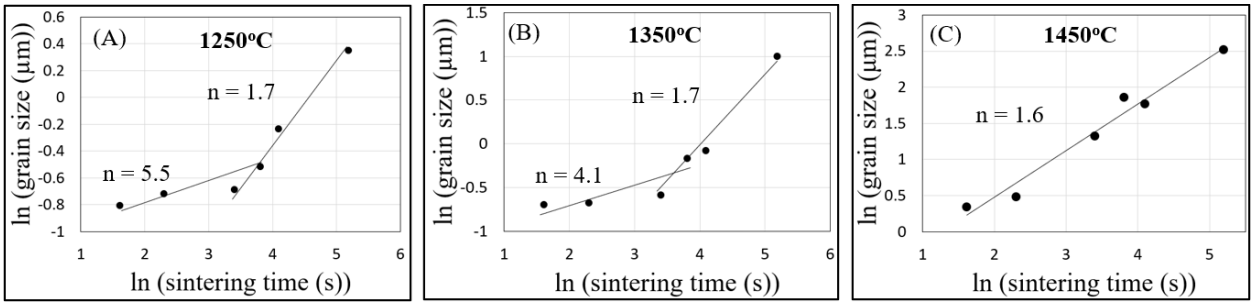

Figure 4.10: Isothermal ln-ln plots of grain size vs sintering temperature for UHS $La_{3-x}Te_4$ EPD films on grafoil substrate. (A) 1250ºC, (B) 1350ºC, (C) 1450ºC. All heat treatments were performed in flowing Ar atmosphere. The grain growth exponent, *n* (Equation 3.3), was calculated from the reciprocal slope of the linear fit to the data. The data for 1250ºC and 1350ºC were best fit with two lines which reflect the transition from surface diffusion to grain boundary diffusion mechanism at longer sintering times. The data for 1450ºC was best fit with a single line which indicates that grain boundary diffusion is the primary active mechanism for all sintering times at this temperature.

The slopes in the first regions for 1250ºC and 1350ºC correspond to $n = 5.5$ and $n = 4.1$, respectively, indicating that grain growth is controlled by surface diffusion. For 1250ºC, the value close to $n = 5$ suggests that grain growth might be partially inhibited by the presence of pores which, prior to significant densification, are present in a high enough concentration to pin the grain boundaries. The slopes in the second regions for both 1250ºC and 1350ºC correspond to $n = 1.7$ and are close to the idealized value of $n = 2$ associated with grain growth controlled by grain boundary diffusion. Similarly, the slope for the 1450ºC data set corresponds to $n = 1.6$ which is again associated with grain growth controlled by grain boundary diffusion. Grain

growth is therefore initially controlled by surface diffusion and transitions to grain boundary diffusion control in the later stages.

The activation energy for grain growth (Equation 4.3) was also analyzed to provide additional investigation into these diffusion mechanisms. Values of the grain growth rate constant, k, were calculated at each temperature from the slope of G^n vs t for each grain growth mechanism. For consistency of the model, $n = 2$ was chosen for grain boundary diffusion and $n = 4$ was chosen for surface diffusion. Activation energy was then calculated from a plot of ln (k) vs $1/T$ (Figure 4.11) for each diffusion mechanism, where the slope is equal to $-Q/R$.

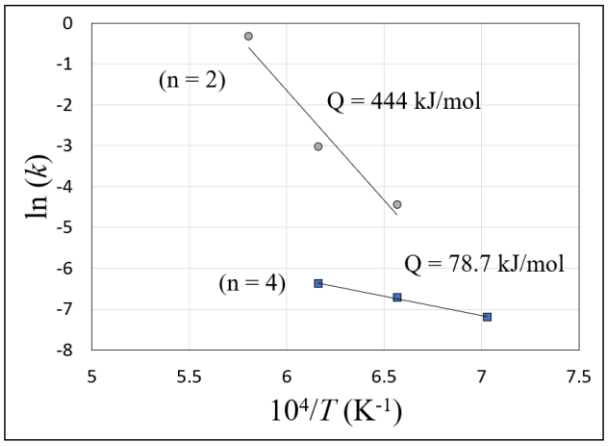

Figure 4.11: Plot of ln (k) vs $1/T$ for UHS $La_{3-x}Te_4$ EPD films on grafoil substrate, where k is the grain growth kinetic constant ((Equation 3.3(Equation 4.2). Values of k were obtained at each temperature from the slope of D^n vs t.The activation energy for grain growth, Q, was calculated from the slope of a linear fit to the data for each value of grain growth exponent, n.

The activation energy of 78.7 kJ/mol for grain growth controlled by surface diffusion is significantly less than that of 444 kJ/mol for grain growth controlled by grain boundary diffusion. Owing to its lower activation energy, surface diffusion is the dominant mass transport mechanism in the initial stages of grain growth. Grain boundary diffusion has a higher activation energy and is delayed until the later stages of grain growth. This observation is consistent with sintering trajectories in the literature, where surface diffusion is the main mechanism of

coarsening in the beginning stages of sintering.[7–9] Furthermore, surface diffusion necessarily occurs first during grain growth since, initially, the microstructure of the green body contains predominantly surface area with minimal grain boundary area. Particles grow by surface diffusion until sufficient grain boundary area is formed for grain boundary diffusion to be significant.[7] Additionally, grain boundary diffusion is activated by higher temperatures which are achieved later in the sintering process depending on the heating rate employed.

This behavior is clear during the UHS process in which the transition from surface diffusion to grain boundary diffusion occurs earlier as sintering temperature increases. The faster transition between diffusion mechanisms at higher temperature is due to both overcoming the activation energy for grain boundary diffusion and the enhanced kinetics of grain boundary formation. The extremely high heating rate of UHS also aids in rapidly providing sufficient thermal energy to activate grain boundary diffusion. The fast transition to grain boundary diffusion is beneficial for rapid densification since it avoids significant coarsening without densification via surface diffusion. Additionally, simultaneous grain growth and pore elimination via grain boundary diffusion in late stages of sintering are associated with an exponential increase in sample density.[6] Therefore, the ability of UHS to quickly activate grain boundary diffusion is valuable for promoting rapid densification.

4.7 Analysis of Sintering Activation Energy

It is evident from the preceding analysis that, during UHS, surface diffusion controls grain growth in the early stages of sintering with a transition to grain boundary diffusion in the later stages. The fast transition to grain boundary diffusion is thought to enable rapid densification via simultaneous pore elimination and grain growth. To verify this hypothesis, the mechanisms of densification were quantitatively assessed through analysis of activation energies

for densification. In the literature, densification is generally modeled by an Arrhenius relationship where the densification rate depends on both temperature and microstructure (density and grain size)[24–27]:

$$\frac{d\rho}{dt} = A\frac{exp\,(-\frac{Q}{RT})}{T}\frac{f(\rho)}{G^m} \qquad \text{(Equation 4.3)}$$

where ρ is density, t is sintering time, A is a material parameter independent of microstructure, Q is sintering activation energy, T is sintering temperature, G is grain size, and m is the grain size dependence on sintering rate.

Using the Arrhenius model from (Equation 4.3, sintering activation energy can be determined from a plot of ln $(\frac{d\rho}{dt}T)$ vs $1/T$, where the slope is equal to $-Q/R$. This relationship is plotted in Figure 4.12 for UHS $La_{3-x}Te_4$ EPD films on grafoil substrate. At fractional densities ≤0.80, the activation energy varies between 146 kJ/mol (ρ = 0.70), 75.8 kJ/mol (ρ = 0.75), and 99.4 kJ/mol (ρ = 0.80) with an average value of 107 kJ/mol. At fractional densities ≥0.87, the activation energy increases significantly to about 337 kJ/mol. The change in activation energy as sample density increases suggests there is a change in densification mechanism between the initial and later stages of sintering as porosity is eliminated.

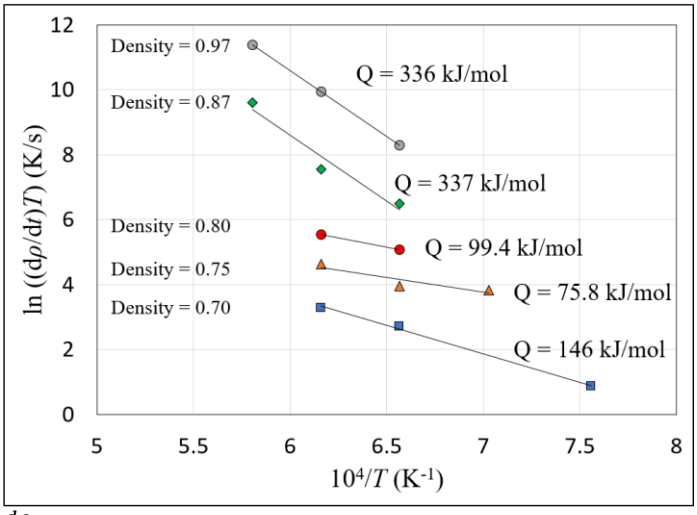

Figure 4.12: Plot of ln $(\frac{d\rho}{dt}T)$ vs $1/T$ at different theoretical densities for UHS $La_{3-x}Te_4$ EPD films on grafoil substrate. The activation energy for sintering, Q (Equation 4.3), was obtained from the slope of a linear fit to the data at each value of density.

The low average activation energy ~107 kJ/mol for fractional densities ≤0.80 is similar to values in the range of 50-100 kJ/mol reported in the literature for the initial stages of sintering in nanomaterials, where the densification mechanism is attributed to surface diffusion.[8] The initial decrease in activation energy from 146 kJ/mol to 75.8 kJ/mol between fractional densities of 0.70 and 0.75 may be due to the formation of sinter necks which provide more efficient transport for surface diffusion.

In the literature, the activation energy for densification via grain boundary diffusion is typically a factor of 2-3 greater than that of surface diffusion for the same material.[8,28–30] For UHS of $La_{3-x}Te_4$, the sintering activation energy similarly increases by a factor of 3 at densities ≥0.87. This comparison facilitates the conclusion that grain boundary diffusion is the primary mechanism for densification during the later stages of sintering. Therefore, similarly to grain growth, the initial stages of sintering during UHS are controlled by surface diffusion with a transition to grain boundary diffusion as density increases. This result affirms that rapid densification is achieved through grain boundary diffusion which allows for simultaneous grain growth and elimination of porosity.

4.8 Discussion of Densification Mechanisms and Implications for $La_{3-x}Te_4$ Processing

The mechanisms of extremely fast densification during UHS are critical to understanding the ability of this technique to sinter refractory materials in under one minute. Despite the short time scale of heat treatment, the final microstructure of the material is sensitive to both sintering temperature and time. This behavior highlights the rapid kinetics and microstructural evolution involved with the UHS process. The initial stages of grain growth and sintering are controlled by surface diffusion which, particularly for nanomaterials, is a common feature of conventional sintering. As time and temperature increase, grain growth and sintering transition to grain boundary diffusion control which yields rapid and significant densification. Similarly, in the literature, the transition to densification and grain growth via grain boundary diffusion is accompanied by a rapid increase in density and grain size.

A key feature of UHS is therefore the fast activation of grain boundary diffusion. This characteristic is important because it limits the time spent under surface diffusion-controlled grain growth and sintering. Surface diffusion is primarily responsible for coarsening which produces grain growth without densification. As a result of limited coarsening, a high driving force for sintering is maintained when grain boundary diffusion, the primary densification mechanism, is activated.

Even though surface diffusion does not directly produce densification, it is still crucial in the initial stages of sintering and is the dominant mass transport mechanism when density is low. The development of sinter necks, which establish bonding and grain boundaries between particles, occurs by surface diffusion. Additionally, surface diffusion leads to microstructural changes that facilitate densification such as changes in pore coordination which creates favorable changes in surface tension that drive a reduction in pore size.[8,9] Other beneficial microstructural

changes that occur via surface diffusion are homogenization of grain shape into spheres, elimination of particle agglomerates via coalescence, and formation an interconnected pore network. Through these changes, surface diffusion indirectly contributes to sintering by establishing a microstructure that is advantageous for densification.

These analyses provide insight into the extremely fast densification achieved by UHS. The low activation energy for surface diffusion facilitates the formation of sinter bonds via surface diffusion prior to significant grain growth. Grain boundary diffusion, which has a higher activation energy, is then responsible for the significant densification and grain growth at later stages. Rapid densification is thus a consequence of the high heating rate enabled by UHS. Temperatures quickly increase above those at which surface diffusion produces coarsening without densification and reach those at which grain boundary diffusion is activated, allowing for rapid sintering and grain growth. In the literature, the extreme heating rate associated with UHS has similarly been proposed enable rapid densification for refractory ceramics by minimizing coarsening prior to densification.14,31–33 Recently, Raj *et al* have identified another possible mechanism of fast densification from the similarities between UHS and flash sintering.[34] The high heating rates involved in UHS may induce a non-equilibrium state of the material similar to flash sintering by creating a large concentration of defects that enables extremely high diffusitivity.[34] The existence of this mechanism in $La_{3-x}Te_4$ would have interesting implications for both sintering and the thermoelectric properties of the material and should be studied in future work.

The application of UHS to densify $La_{3-x}Te_4$ represents a significant processing achievement for synthesis and device fabrication. The material sinters in less than one minute and achieves high density and large grain sizes. The ability to quickly densify $La_{3-x}Te_4$ not only

reduces processing time but also helps mitigate oxidation by minimizing exposure to high temperature. The UHS technique is versatile and can readily sinter bulk $La_{3-x}Te_4$ pellets as well as $La_{3-x}Te_4$ films produced by EPD on planar and three-dimensional substrates. These results exhibit the viability of processing advanced architectures by UHS. Furthermore, densification of $La_{3-x}Te_4$ via free sintering demonstrates that pressure sintering techniques such as hot pressing and spark plasma sintering are not required to densify $La_{3-x}Te_4$. Sintering the material without the use of such complex equipment is important for reducing synthesis costs and simplifying the overall processing procedures. Lastly, the large grain sizes achieved through UHS are 1-3 orders of magnitude larger than those normally attained for sintered $La_{3-x}Te_4$.[10] UHS $La_{3-x}Te_4$ samples provide an exciting opportunity to investigate the effects of grain size and grain boundary scattering on the thermoelectric properties of the material and will be studied in future work at JPL.

4.9 Summary and Conclusions

Ultra-fast high temperature sintering (UHS) achieves rapid, pressure-less sintering of both $La_{3-x}Te_4$ EPD films and bulk $La_{3-x}Te_4$ pellets in as little as 10 seconds. Samples have high phase purity with minimal oxidation and achieve >85% theoretical density, with some samples approaching or exceeding 90% density. Grain sizes range from 0.8-1.8 μm for UHS EPD samples and achieve 2.44 μm for a UHS $La_{3-x}Te_4$ pellet. The free sintering technique is versatile and readily applicable to $La_{3-x}Te_4$ samples with non-uniform geometries such as $La_{3-x}Te_4$ EPD coatings on Ni mesh and Ni foam substrates. For EPD samples, a good CTE match between $La_{3-x}Te_4$ and the substrate material is necessary to avoid extensive film cracking during sintering.

The influence of UHS temperature and time on the microstructure evolution of $La_{3-x}Te_4$ EPD films on grafoil substrate was studied. Despite the short sintering times <3 minutes, both

temperature and time have a significant impact on microstructure which highlights the fast kinetics that occur during UHS. For constant sintering time of 60 seconds, particle coarsening without densification occurs for temperatures ≤1050°C. Initial stages of sintering occur at 1150-1250°C with the formation of sinter necks. Intermediate stages of sintering are evident at 1350°C with the presence of distinct grain boundaries and a reduction in porosity. Final stages of sintering occur at 1450°C where there is significant and rapid densification/grain growth.

The mechanisms, kinetics, and thermodynamics of the UHS process were characterized by studying the isothermal microstructure evolution as a function of time at 1250, 1350, and 1450°C. The initial stages of grain growth, which occur for times <60 seconds at 1250 and 1350°C, are controlled by surface diffusion as indicated by the grain growth exponents n = 5.5 (1250°C) and n = 4.1 (1350°C). Later stages of grain growth, which occur at 1450°C or for times ≥60 seconds at 1250 and 1350°C, are controlled by grain boundary diffusion as indicated by the grain growth exponent n = ~1.7. The activation energy for surface diffusion-controlled grain growth is 78.7 kJ/mol and that of grain boundary-controlled grain growth is 444 kJ/mol. Sintering is controlled by the same diffusion mechanisms, with the early stages of sintering controlled by surface diffusion as evidenced by low value of activation energy ~107 kJ/mol for fractional densities ≤0.80. Later stages of sintering are controlled by grain boundary diffusion which has an activation energy of ~337 kJ/mol for fractional densities ≥0.87.

Extremely fast densification achieved by UHS is a result of the high heating rate which avoids low temperatures at which surface diffusion causes coarsening without densification and quickly activates grain boundary diffusion which yields rapid increases in density and grain size. Surface diffusion indirectly contributes to densification in the initial stages of sintering by establishing beneficial microstructure rearrangements such as changes in pore coordination and

formation of sinter bonds between particles. These changes along with a lack of significant coarsening maintain a high driving force for densification once grain boundary diffusion is activated, leading to rapid densification. The possibility that the high heating rate induces a flash sintering state of the material should also be investigated as another potential mechanism for fast densification.

The ability of UHS to sinter $La_{3-x}Te_4$ is a significant breakthrough and facilitates future development of simplified processing methods, fabrication of novel device geometries, and study of grain size effects on thermoelectric properties. Establishment of free sintering of the material demonstrates that pressure sintering techniques such as hot pressing and spark plasma sintering are not required for densification of $La_{3-x}Te_4$ and allows for the use of much simpler and cheaper equipment for synthesis and processing. Furthermore, the large grain sizes achieved through UHS are orders of magnitude larger than those traditionally obtained for $La_{3-x}Te_4$ which presents a unique synthesis opportunity for studying the effects of grain size and grain boundary scattering on thermoelectric performance.

4.10 References

(1) Goldsmid, H. J. Porous Thermoelectric Materials. *Materials* **2009**, *2* (3), 903. https://doi.org/10.3390/MA2030903.

(2) May, A. F.; Fleurial, J. P.; Snyder, G. J. Thermoelectric Performance of Lanthanum Telluride Produced via Mechanical Alloying. *Phys Rev B Condens Matter Mater Phys* **2008**, *78* (12), 125205. https://doi.org/10.1103/PHYSREVB.78.125205/FIGURES/11/MEDIUM.

(3) Cheikh, D. Synthesis and Characterization of Rare-Earth Tellurides and Their Composites for High-Temperature Thermoelectric Applications, UCLA, Los Angeles, 2017.

(4) Ma, J. Improving the Mechanical Strength and Power Conversion Efficiency of High Temperature Thermoelectrics, UCLA, Los Angeles, 2014.

(5) Rojek, J.; Nosewicz, S.; Maździarz, M.; Kowalczyk, P.; Wawrzyk, K.; Lumelskyj, D. Modeling of a Sintering Process at Various Scales. *Procedia Eng* **2017**, *177*, 263–270. https://doi.org/10.1016/J.PROENG.2017.02.210.

(6) German, R. M. Coarsening in Sintering: Grain Shape Distribution, Grain Size Distribution, and Grain Growth Kinetics in Solid-Pore Systems. *http://dx.doi.org/10.1080/10408436.2010.525197* **2010**, *35* (4), 263–305. https://doi.org/10.1080/10408436.2010.525197.

(7) German, R. M. Sintering Trajectories: Description on How Density, Surface Area, and Grain Size Change. *JOM* **2016**, *68* (3), 878–884. https://doi.org/10.1007/S11837-015-1795-8/FIGURES/10.

(8) Fang, Z. Z.; Wang, H. Densification and Grain Growth during Sintering of Nanosized Particles. *International Materials Reviews* **2008**, *53* (6), 326–352. https://doi.org/10.1179/174328008X353538.

(9) Fang, Z. Z.; Wang, H.; Kumar, V. Coarsening, Densification, and Grain Growth during Sintering of Nano-Sized Powders—A Perspective. *Int J Refract Metals Hard Mater* **2017**, *62*, 110–117. https://doi.org/10.1016/J.IJRMHM.2016.09.004.

(10) May, A. High-Temperature Transport in Lanthanum Telluride and Other Modern Thermoelectric Materials, California Institute of Technology, Pasadena, 2010.

(11) Nozariasbmarz, A.; Tahmasbi Rad, A.; Zamanipour, Z.; Krasinski, J. S.; Tayebi, L.; Vashaee, D. Enhancement of Thermoelectric Power Factor of Silicon Germanium Films Grown by Electrophoresis Deposition. *Scr Mater* **2013**, *69* (7), 549–552. https://doi.org/10.1016/J.SCRIPTAMAT.2013.06.025.

(12) Okamoto, T.; Horii, S.; Uchikoshi, T.; Suzuki, T. S.; Sakka, Y.; Funahashi, R.; Ando, N.; Sakurai, M.; Shimoyama, J. I.; Kishio, K. Fabrication of Multilayered Oxide Thermoelectric Modules by Electrophoretic Deposition under High Magnetic Fields. *Appl Phys Lett* **2006**, *89* (8), 81912. https://doi.org/10.1063/1.2338749/165753.

(13) Talebi, T.; Ghomashchi, R.; Talemi, P.; Aminorroaya, S. Suspension Characteristics and Electrophoretic Deposition of p -Type Bi 2 Te 3 Films for Thermoelectric Applications . *J Electrochem Soc* **2018**, *165* (9), D364–D369. https://doi.org/10.1149/2.0301809JES/XML.

(14) Wang, C.; Ping, W.; Bai, Q.; Cui, H.; Hensleigh, R.; Wang, R.; Brozena, A. H.; Xu, Z.; Dai, J.; Pei, Y.; Zheng, C.; Pastel, G.; Gao, J.; Wang, X.; Wang, H.; Zhao, J. C.; Yang, B.; Zheng, X.; Luo, J.; Mo, Y.; Dunn, B.; Hu, L. A General Method to Synthesize and Sinter Bulk Ceramics in Seconds. *Science (1979)* **2020**, *368* (6490), 521–526. https://doi.org/10.1126/SCIENCE.AAZ7681/SUPPL_FILE/AAZ7681S2.MP4.

(15) Delaire, O.; May, A. F.; Mcguire, M. A.; Porter, W. D.; Lucas, M. S.; Stone, M. B.; Abernathy, D. L.; Ravi, V. A.; Firdosy, S. A.; Snyder, G. J. Phonon Density of States and Heat Capacity of La 3−x Te 4. https://doi.org/10.1103/PhysRevB.80.184302.

(16) Material Expansion Coefficients. https://psec.uchicago.edu/thermal_coefficients/cte_metals_05517-90143.pdf (accessed 2023-05-07).

(17) Flexible Graphite TYPICAL GRAFOIL SHEET PROPERTIES. https://www.gasketing.net/pdf/GHP.pdf (accessed 2023-05-07).

(18) *Boron Nitride Product of BN-A grade*. https://www.advaluetech.com/products/boron-nitride/bn-a (accessed 2023-05-07).

(19) Kapadia, C. M.; Leipold, M. H.; Assistant, R. THE MECHANISM OF GRAIN GROWTH IN CERAMICS. *NASA Contractor Report* **1972**

(20) Moravec, J. Determination of the Grain Growth Kinetics as a Base Parameter for Numerical Simulation Demand. *MM Science Journal* **2015**, *2015* (OCTOBER), 649–653. https://doi.org/10.17973/MMSJ.2015_10_201523.

(21) Nichols, F. A. Theory of Grain Growth in Porous Compacts. *J Appl Phys* **2004**, *37* (13), 4599. https://doi.org/10.1063/1.1708102.

(22) Bourgeois, L.; Dehaudt, P.; Lemaignan, C.; Fredric, J. P. Pore Migration in UO2 and Grain Growth Kinetics. *Journal of Nuclear Materials* **2001**, *295* (1), 73–82. https://doi.org/10.1016/S0022-3115(01)00502-5.

(23) Baumann, V.; Popa, K.; Cologna, M.; Rivenet, M.; Walter, O. Grain Growth of NpO2 and UO2 Nanocrystals. *RSC Adv* **2023**, *13* (10), 6414–6421. https://doi.org/10.1039/D3RA00487B.

(24) Wang, J.; Raj, R. Activation Energy for the Sintering of Two-Phase Alumina/Zirconia Ceramics. *Journal of the American Ceramic Society* **1991**, *74* (8), 1959–1963. https://doi.org/10.1111/J.1151-2916.1991.TB07815.X.

(25) Fang, T. T.; Shiue, J. T.; Shiau, F. S. On the Evaluation of the Activation Energy of Sintering. *Mater Chem Phys* **2003**, *80* (1), 108–113. https://doi.org/10.1016/S0254-0584(02)00373-5.

(26) Ye, C. C.; Wei, W. Q.; Fu, X.; Wang, C. H.; Ru, H. Q. Effect of Sintering Activation Energy on Si3N4 Composite Ceramics. *Ceram Int* **2022**, *48* (4), 4851–4857. https://doi.org/10.1016/J.CERAMINT.2021.11.021.

(27) Jana, D. C.; Sundararajan, G.; Chattopadhyay, K. Effective Activation Energy for the Solid-State Sintering of Silicon Carbide Ceramics. *Metall Mater Trans A Phys Metall Mater Sci* **2018**, *49* (11), 5599–5606. https://doi.org/10.1007/S11661-018-4884-9/FIGURES/8.

(28) Wang, J.; Raj, R. Estimate of the Activation Energies for Boundary Diffusion from Rate-Controlled Sintering of Pure Alumina, and Alumina Doped with Zirconia or Titania. *Journal of the American Ceramic Society* **1990**, *73* (5), 1172–1175. https://doi.org/10.1111/J.1151-2916.1990.TB05175.X.

(29) Panigrahi, B. B. Sintering and Grain Growth Kinetics of Ball Milled Nanocrystalline Nickel Powder. *Materials Science and Engineering: A* **2007**, *460–461*, 7–13. https://doi.org/10.1016/J.MSEA.2007.01.035.

(30) Panigrahi, B. B.; Godkhindi, M. M.; Das, K.; Mukunda, P. G.; Ramakrishnan, P. Sintering Kinetics of Micrometric Titanium Powder. *Materials Science and Engineering: A* **2005**, *396* (1–2), 255–262. https://doi.org/10.1016/J.MSEA.2005.01.016.

(31) Lin, Z.; Zhao, X.; Wang, C.; Dong, Q.; Qian, J.; Zhang, G.; Brozena, A. H.; Wang, X.; He, S.; Ping, W.; Chen, G.; Pei, Y.; Zheng, C.; Callie Clifford, B.; Hong, M.; Wu, Y.; Yang, B.; Luo, J.; Albertus, P.; Hu, L.; Lin, Z.; Zhao, X.; Wang, C.; Dong, Q.; Qian, J.; Brozena, A. H.; Wang, X.; He, S.; Ping, W.; Chen, G.; Clifford, B. C.; Hong, M.; Hu, L.; Zhang, G.; Wu, Y.; Pei, Y.; Zheng, C.; Yang, B. Rapid Pressureless Sintering of Glasses. *Small* **2022**, *18* (17), 2107951. https://doi.org/10.1002/SMLL.202107951.

(32) Mishra, T. P.; Wang, S.; Lenser, C.; Jennings, D.; Kindelmann, M.; Rheinheimer, W.; Broeckmann, C.; Bram, M.; Guillon, O. Ultra-Fast High-Temperature Sintering of Strontium Titanate. *Acta Mater* **2022**, *231*, 117918. https://doi.org/10.1016/J.ACTAMAT.2022.117918.

(33) Guo, R. F.; Mao, H. R.; Zhao, Z. T.; Shen, P. Ultrafast High-Temperature Sintering of Bulk Oxides. *Scr Mater* **2021**, *193*, 103–107. https://doi.org/10.1016/J.SCRIPTAMAT.2020.10.045.

(34) Raj, R.; Wolf, D. E.; Yamada, C. N.; Jha, S. K.; Lebrun, J. M. On the Confluence of Ultrafast High-Temperature Sintering and Flash Sintering Phenomena. *Journal of the American Ceramic Society* **2023**, *106* (7), 3983–3998. https://doi.org/10.1111/JACE.19070.

Chapter 5 Thermoelectric Properties of UHS $La_{3-x}Te_4$

5.1 Introduction and Background on Thermoelectric Performance of $La_{3-x}Te_4$

Lanthanum telluride ($La_{3-x}Te_4$) has generated interest as a thermoelectric material due to its ZT value of 1.1 at 1275 K which makes it one of the best-performing bulk n-type materials.[1,2] The high ZT is a consequence of the material's complex crystal structure (Figure 5.1). The cubic structure is composed of distorted La_6Te octahedra in which there are four shorter and four longer La-Te bonds.[3] The structure allows for a defect stoichiometry ($0 \leq x \leq 1/3$) through the formation of La vacancies and can accommodate vacancies on up to 1/9 of the La sites. La vacancies play a critical role in determining the thermal and electronic properties of the material and the thermoelectric performance is therefore determined by the La vacancy concentration, *x*.

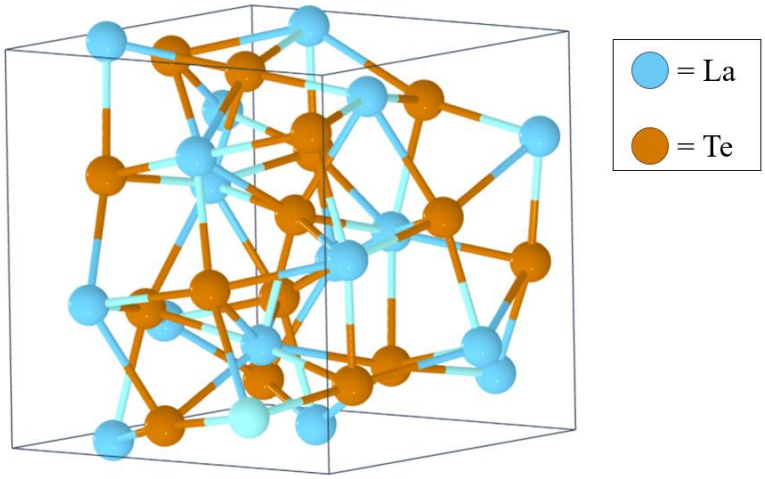

Figure 5.1: The crystal structure of La_3Te_4. Te atoms occupy octahedral sites of La atoms to form distorted La_6Te octahedra. The structure can accommodate vacancies on the La sites, with up to 1/9 of La atoms being absent. (*Data retrieved from the Materials Project for La_3Te_4 (mp-879) from database version v2022.10.28.)*[3,4]

Introducing La vacancies into the structure causes significant phonon scattering that contributes to a lattice thermal conductivity as low as 0.4-0.8 W/m·K.[2,5] The intrinsically low thermal conductivity of $La_{3-x}Te_4$ is a contributing factor to its high thermoelectric performance. Additionally, the concentration of La vacancies controls the electronic properties of the material by altering the free carrier concentration[2]:

$$n = n_{max}(1 - 3x) \qquad \text{(Equation 5.1)}$$

where n is the free carrier concentration, $n_{max} = 4.5 \times 10^{21}$ cm^{-3} is the maximum carrier concentration, and x is the La vacancy concentration which varies between 0 and 1/3.

$La_{3-x}Te_4$ ranges from a degenerate semiconductor with metallic-type conduction when there are no La vacancies ($x = 0$) to an electronic insulator at the maximum La vacancy concentration ($x = 1/3$).[2] The electronic and thermal properties of the material are optimized for thermoelectric performance at $x = 0.23$.[2] The exact stoichiometry of $La_{3-x}Te_4$ samples with different La vacancy concentrations is typically expressed in terms of the Te/La ratio (Table 5.1).

Table 5.1: Stoichiometry and general electronic properties of $La_{3-x}Te_4$ samples with different *x* values.

La vacancy concentration	**$La_{3-x}Te_4$ stoichiometry**	**Electronic properties**
x = 0	$LaTe_{1.33}$	Conducting
x = 0.23	$LaTe_{1.46}$	Optimized for thermoelectric performance
x = 0.33	$LaTe_{1.50}$	Insulating

To date, reports on the thermoelectric performance of $La_{3-x}Te_4$ are for samples prepared through mechanochemical synthesis followed by densification via hot pressing or spark plasma sintering (SPS).[2,5–9] It is therefore important to determine baseline performance for $La_{3-x}Te_4$ densified through ultrafast high-temperature sintering (UHS) and compare the thermoelectric properties to those established in the literature for $La_{3-x}Te_4$. The results and analysis presented in this chapter demonstrate that the thermoelectric performance of $La_{3-x}Te_4$ films and pellets prepared via UHS is comparable to that of optimized $La_{3-x}Te_4$ samples processed through hot pressing and SPS. Verification of the thermoelectric performance of UHS $La_{3-x}Te_4$ validates the sintering technique for processing of $La_{3-x}Te_4$ and is a remarkable achievement for rapid, pressure-less sintering of the material.

5.2 Experimental Methods

$La_{3-x}Te_4$ powder ($x = 0.23$, $LaTe_{1.46}$) was synthesized using established mechanochemical methods.[2] Briefly, elemental La and Te were combined in stoichiometric amounts and ball milled to achieve the alloyed powder. The elemental reactants were handled in an Ar-filled glovebox and the ball mill vial was sealed under Ar. The resulting as-synthesized $La_{3-x}Te_4$ powder was used without further treatment.

$La_{3-x}Te_4$ films on BN substrate were synthesized via EPD as described in Chapter 3. The solvent was THF and deposition voltage, time, and particle concentration were 100 V, 10 min,

and 10 mg/mL, respectively. BN was selected as the substrate material for thermoelectric measurements of the thin film $La_{3-x}Te_4$ samples since it is electrically insulating. Bulk $La_{3-x}Te_4$ pellets were prepared by loading as-synthesized $La_{3-x}Te_4$ powder into a stainless-steel pellet die and cold-pressing at 1000 psi. Pellets had a thickness of 1 mm and diameter of 1 cm. All samples were sintered via ultrafast high temperature sintering (UHS) as detailed in Chapter 4.3. For all samples, sintering temperature and time were 1450ºC and 10 seconds, respectively, and heat treatments were performed in flowing ultra-high purity argon. UHS $La_{3-x}Te_4$ pellets generally achieved a density of 86-92% of theoretical as measured by the Archimedes method.

Electrical resistivity and Seebeck coefficient for UHS $La_{3-x}Te_4$ film on BN substrate were measured using a custom two-electrode setup. Electrical resistance was measured using AC impedance which was converted to resistivity using the dimensions of the film. Seebeck coefficient was determined from measurements of the open circuit voltage between the hot and cold side. Property measurements were limited to a maximum temperature of 300ºC due to instability of the contacts at high temperature. Thermal conductivity was not measured due to difficulties in experimental setup and obtaining reliable data for thin films.[10,11]

Thermoelectric properties for UHS $La_{3-x}Te_4$ pellets were measured up to 1000ºC. Electrical resistivity was measured using a four-point probe/Hall effect system. Seebeck coefficient was measured using a custom fabricated light pulse system based on established methods.[2,12] Thermal conductivity was obtained from thermal diffusivity measurements using a Netzsch LFA 457 laser flash analysis system with corrections applied for the temperature-dependent heat capacity and sample density.

5.3 Thermoelectric Properties of UHS $La_{3-x}Te_4$

The temperature-dependent Seebeck coefficients of UHS $La_{3-x}Te_4$ samples are shown in Figure 5.2 where they are compared to those of optimized bulk $La_{3-x}Te_4$ samples prepared by SPS[8] and hot pressing[2]. There is good agreement between the Seebeck coefficient values of the UHS thin film and bulk pellet, and they exhibit a similar increase in absolute value up to 575 K. The Seebeck coefficient of the UHS sample and literature samples have an approximately linear dependence on temperature, with an inflection point at approximately 900 K. This decrease in slope is attributed to a loss of degeneracy and activation of minority carriers which occurs due to the lower free carrier concentration resulting from the high La vacancy concentration.[2,6] The similarities in Seebeck behavior between the UHS and literature samples indicates that the electronic structure of the optimized material is preserved after sintering.

The Seebeck coefficient of the UHS bulk pellet reaches a maximum value at 1273 K of about -165 μV/K, which is lower than that of -206 μV/K for SPS $LaTe_{1.46}$ and -235 μV/K for hot-pressed $La_{3-x}Te_4$. This discrepancy indicates that the composition of the UHS sample has shifted slightly toward a lower x value, possibly due to Te sublimation during sintering or a slight Te deficiency in the starting powder. However, the Seebeck coefficient values suggest a change in composition of $x < 0.04$ since the correlation between Seebeck coefficient and composition is well established for $La_{3-x}Te_4$ based on the concentration of rare-earth vacancies.[2,6,7,21]

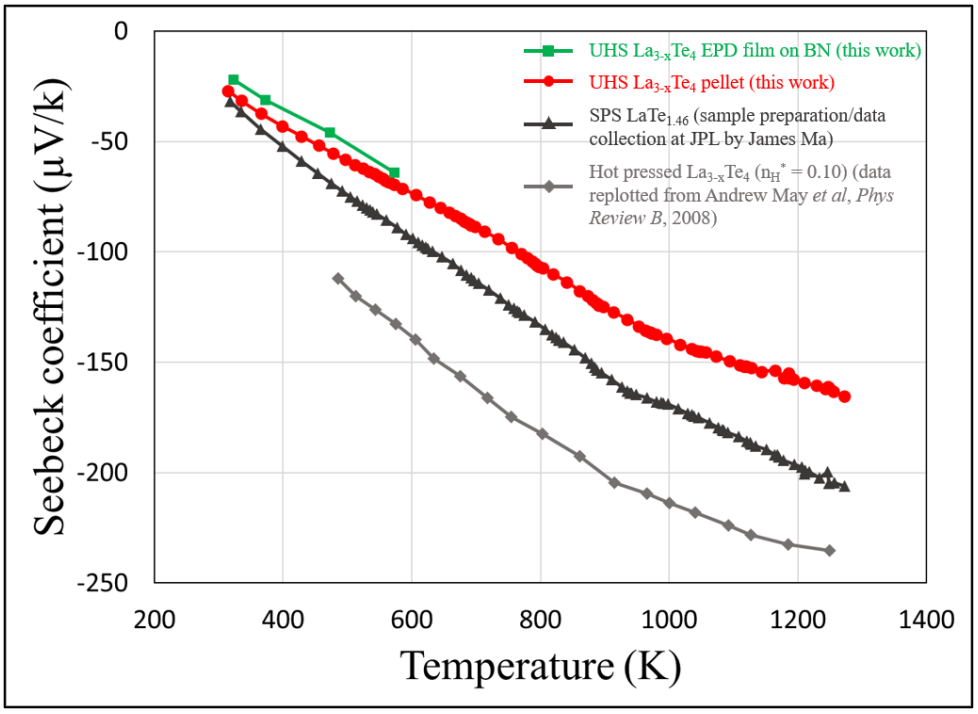

Figure 5.2: Temperature-dependent Seebeck coefficient measured for UHS $La_{3-x}Te_4$ EPD film on BN and UHS $La_{3-x}Te_4$ pellet. Values for bulk SPS $LaTe_{1.46}$ prepared at JPL by James Ma[8] and bulk hot-pressed $La_{3-x}Te_4$ at an optimized carrier concentration of $n_H^* = 0.10$ in the literature (Andrew May *et al*, *Physical Review B*, **78**, 2008)[2] are also shown for comparison.

The temperature-dependent electrical resistivities of UHS $La_{3-x}Te_4$ samples and optimized $La_{3-x}Te_4$ are shown in Figure 5.3. The resistivity of the bulk UHS $La_{3-x}Te_4$ pellet is comparable to that of SPS $LaTe_{1.46}$ and indicates that UHS achieves good bonding and densification of the material for electron transport. The resistivity increases with temperature, indicating degenerate semiconductor/metallic-type conduction which is also observed in SPS and hot pressed $La_{3-x}Te_4$ samples. The room temperature resistivity of bulk UHS $La_{3-x}Te_4$ is about 17% lower than that of SPS $LaTe_{1.46}$, and at 1273 K the difference increases to about 32%. The lower resistivity of the UHS sample is likely due to the slight decrease in *x* value that was also observed in the Seebeck coefficient measurements (Figure 5.2) which increases the free carrier concentration. The large grain size of UHS $La_{3-x}Te_4$ may also contribute to lower electrical

resistivity by reducing the effects of grain boundary scattering and enhancing charge carrier mobility in the material[13–15], though further investigation into this mechanism is necessary.

The resistivity of the UHS $La_{3-x}Te_4$ EPD thin film sample is higher than that of the bulk UHS pellet and SPS $LaTe_{1.46}$, having a value approximately 40% and 20% greater at room temperature, respectively. This most likely results from high contact resistance due to the two-electrode technique employed during measurement as well as defects in the film such as extensive cracking which occur during sintering due to CTE mismatch between the film and substrate (Chapter 4). The true resistivity of the film is likely closer to that of the UHS bulk pellet. This conclusion is further informed by the Seebeck coefficient values for the thin film sample which are similar to those of the bulk pellet (Figure 5.2). The values of Seebeck coefficient are a good indicator of the electronic structure of the material regardless of microstructure since Seebeck coefficient is, in general, independent of microstructure and mechanical defects. Furthermore, samples with a low Seebeck coefficient are expected to also have low electrical resistivity since the correlation between Seebeck coefficient and electrical resistivity is well established.[2,6] Therefore, the Seebeck coefficient indicates that the electronic structure of the UHS $La_{3-x}Te_4$ film is similar to bulk UHS $La_{3-x}Te_4$ and the samples should have similar electrical resistivity. Optimization of the thin film measurement technique is necessary to obtain accurate verification resistivity values for the UHS $La_{3-x}Te_4$ thin film sample.

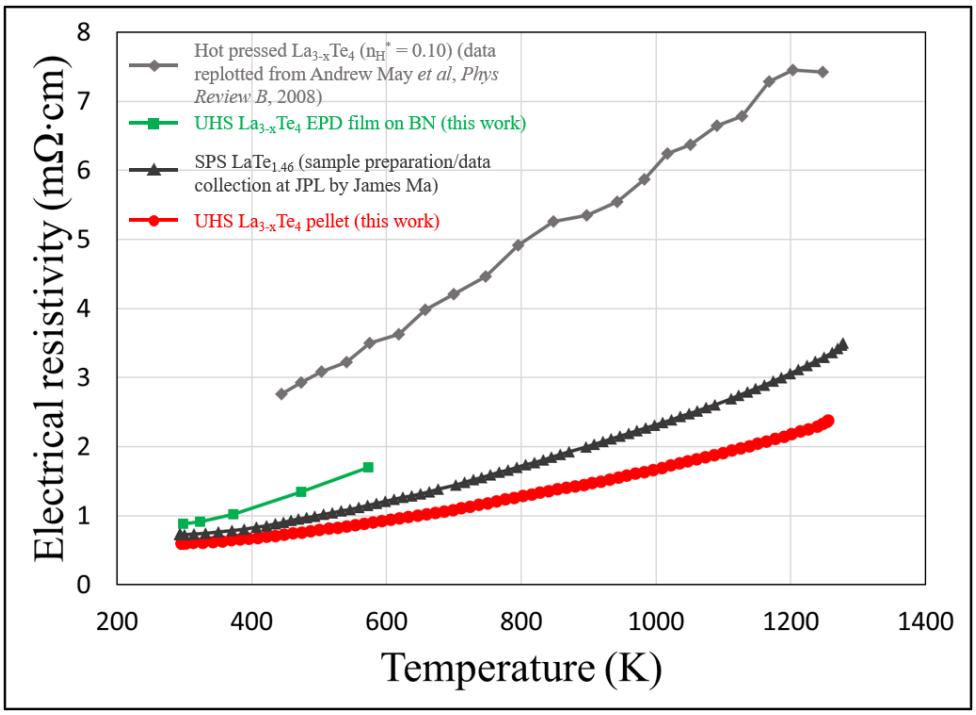

Figure 5.3: Temperature-dependent electrical resistivity measured for UHS $La_{3-x}Te_4$ EPD film on BN and UHS $La_{3-x}Te_4$ pellet. Values for bulk SPS $LaTe_{1.46}$ prepared at JPL by James Ma[8] and bulk hot-pressed $La_{3-x}Te_4$ at an optimized carrier concentration of $n_H^* = 0.10$ in the literature (Andrew May *et al*, *Physical Review B*, **78**, 2008)[2] are also shown for comparison.

The temperature-dependent power factors ($S^2\sigma$) of UHS $La_{3-x}Te_4$ samples and optimized $La_{3-x}Te_4$ are shown in Figure 5.4. The power factor of the UHS $La_{3-x}Te_4$ film is about 30-50% of bulk UHS $La_{3-x}Te_4$ and optimized $La_{3-x}Te_4$ between 323-573 K due to the higher measured electrical resistivity which suppresses the contribution from the Seebeck coefficient. At room temperature, the bulk UHS $La_{3-x}Te_4$ pellet has a 13% larger power factor than SPS $LaTe_{1.46}$ as a result of its lower electrical resistivity and comparable Seebeck coefficient. As temperature increases, the power factor of SPS $LaTe_{1.46}$ exceeds that of UHS $La_{3-x}Te_4$ since the magnitude of its Seebeck coefficient squared exhibits a faster increase with temperature compared to its electrical resistivity. The power factor of hot-pressed $La_{3-x}Te_4$ is much lower at high temperature than that of bulk UHS $La_{3-x}Te_4$ and SPS $LaTe_{1.46}$ due to its ~2-3 times larger resistivity. UHS $La_{3-x}Te_4$ achieves a peak power factor of 11.7 μW/cm·K^2 at 1073 K compared to 13.1 μW/cm·K^2

between 1175-1225 K for SPS $LaTe_{1.46}$. These results demonstrate that UHS $La_{3-x}Te_4$ attains considerable electronic performance that is comparable to optimized $La_{3-x}Te_4$. This favorable combination of electrical resistivity and Seebeck coefficient is necessary for high thermoelectric output.

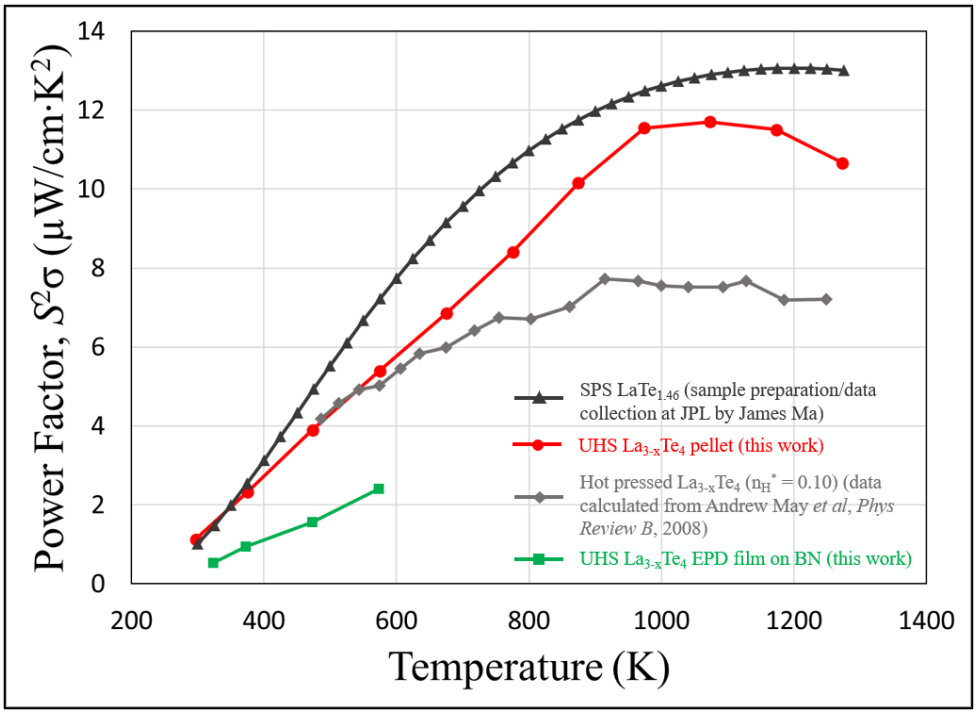

Figure 5.4: Temperature-dependent power factor ($S^2\sigma$) for UHS $La_{3-x}Te_4$ EPD film on BN and UHS $La_{3-x}Te_4$ pellet. The values were calculated from Seebeck coefficient (Figure 5.2) and electrical resistivity (Figure 5.3). Values for bulk SPS $LaTe_{1.46}$ prepared at JPL by James Ma[8] and bulk hot-pressed $La_{3-x}Te_4$ at an optimized carrier concentration of $n_H^* = 0.10$ in the literature (Andrew May *et al*, *Physical Review B*, **78**, 2008)[2] are also shown for comparison. The values for the hot pressed sample (May *et al*) were calculated based on the Seebeck and electrical resistivity data that are replotted in Figure 5.2 and Figure 5.3.

The temperature-dependent thermal conductivities of the bulk UHS $La_{3-x}Te_4$ pellet and optimized $La_{3-x}Te_4$ samples are shown in Figure 5.5A. The thermal conductivity of the UHS $La_{3-x}Te_4$ thin film is not reported due to difficulties in obtaining accurate measurements on thin film samples.[10,11] The values and temperature-dependent behavior of thermal conductivity for UHS $La_{3-x}Te_4$ match well to those of $LaTe_{1.46}$, with a difference of less than 10% across the entire temperature range of measurement (298-1273 K). The thermal conductivity of hot-pressed La_{3-}

$_x$Te$_4$ is ~50-60% of that of UHS La$_{3-x}$Te$_4$ and SPS LaTe$_{1.46}$ due to the higher electrical resistivity of the sample which reduces the electronic contribution to thermal conductivity. The good agreement between the thermal conductivities of UHS La$_{3-x}$Te$_4$ and SPS LaTe$_{1.46}$ indicates that the lower electrical resistivity of UHS La$_{3-x}$Te$_4$ does result in a significant increase of the thermal conductivity. This result is important for maintaining high thermoelectric performance of the material since a low thermal conductivity is necessary to achieve a high ZT value, and a decrease in electrical resistivity typically results in a higher overall thermal conductivity due to the increased electronic contribution.[2,6–8,16]

In Figure 5.5B, the electronic (κ_e) and lattice thermal conductivities (κ_L) of UHS La$_{3-x}$Te$_4$ and SPS LaTe$_{1.46}$ were calculated from the total thermal conductivity (k_{total}) and electrical resistivity using the Wiedemann-Franz law[16]:

$$k_{total} = k_e + k_L = L\sigma T + k_L \qquad \text{(Equation 5.2)}$$

where k_{total} is the total thermal conductivity, κ_e is the electronic thermal conductivity, κ_L is the lattice thermal conductivity, L is the Lorenz number, σ is the electrical conductivity, and T is temperature.

For accuracy of the model, a first order correction of the Lorenz number was performed as a function of Seebeck coefficient due to the degeneracy of La$_{3-x}$Te$_4$ [17]:

$$L = 1.5 + \exp\left(-\frac{|S|}{116}\right) \qquad \text{(Equation 5.3)}$$

where L is the Lorenz number and S is the Seebeck coefficient.

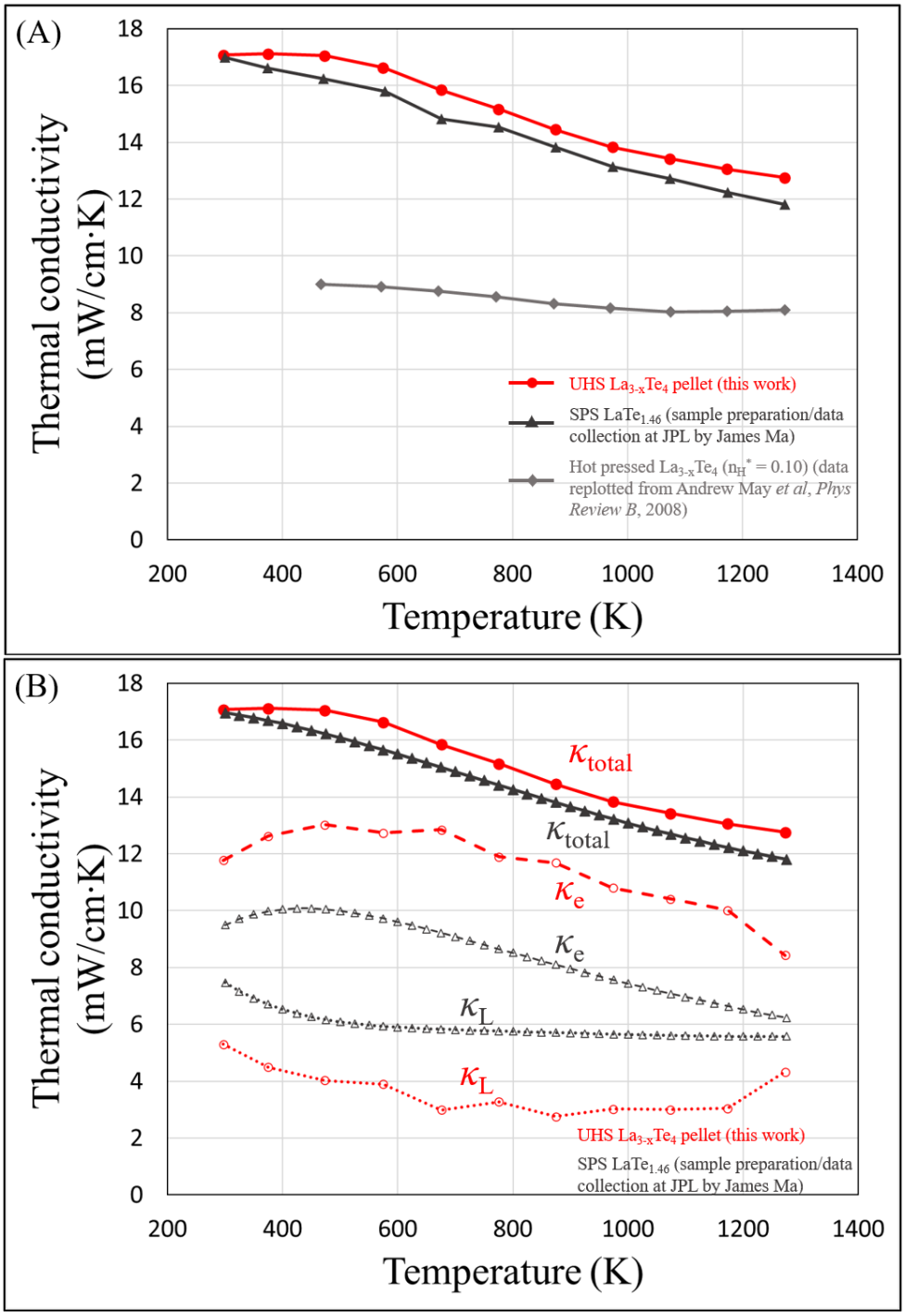

Figure 5.5: (A) Temperature-dependent total thermal conductivity measured for UHS $La_{3-x}Te_4$ pellet. Values for bulk SPS $LaTe_{1.46}$ prepared at JPL by James Ma[8] and bulk hot-pressed $La_{3-x}Te_4$ at an optimized carrier concentration of $n_H^* = 0.10$ in the literature (Andrew May *et al*, *Physical Review B*, **78**, 2008)[2] are also shown for comparison. (B) Temperature-dependent calculations for total thermal conductivity (κ_{total}), electronic contribution to thermal conductivity (κ_e), and lattice contribution to thermal conductivity (κ_L) for UHS $La_{3-x}Te_4$ pellet and SPS $LaTe_{1.46}$ prepared at JPL by James Ma[8]. The electronic and lattice thermal conductivities were calculated using the Wiedmann-Franz Law (Equation 5.2) with a first order degeneracy correction for Lorenz number (Equation 5.3).

As expected, the electronic thermal conductivity of UHS $La_{3-x}Te_4$ is about 20-30% higher than that of SPS $LaTe_{1.46}$ due to the higher electrical conductivity (Figure 5.5B). By contrast, the calculated lattice thermal conductivity of UHS $La_{3-x}Te_4$ is about 30-50% lower than that of SPS $LaTe_{1.46}$. The decrease in lattice thermal conductivity could be caused by the lower density of UHS $La_{3-x}Te_4$ compared to the SPS $LaTe_{1.46}$ samples which enables additional phonon scattering by pores.[18] It is interesting that the porosity appears to affect the lattice thermal conductivity more strongly than it does electrical resistivity, suggesting that the scattering effect of pores is more significant for phonons than electrons. Additionally, the large grain size of UHS $La_{3-x}Te_4$ does not lead to an increase in lattice thermal conductivity. This is contrary to expectation since large-grained materials generally have higher lattice thermal conductivities as a result of reduced grain boundary scattering of phonons.[19] UHS $La_{3-x}Te_4$ appears to deviate somewhat from the expected relationship between microstructure, electrical resistivity, and thermal conductivity. Therefore, the relationship between grain size, density, and electron/phonon scattering mechanisms for UHS $La_{3-x}Te_4$ provides an interesting route for future investigation.

The temperature-dependent ZT values for the bulk UHS $La_{3-x}Te_4$ and optimized $La_{3-x}Te_4$ samples are shown in Figure 5.6. Below 500 K, the ZT of UHS $La_{3-x}Te_4$ is nearly identical to that of SPS $LaTe_{1.46}$ owing to their similar power factor and thermal conductivity at low temperature. The ZT of hot pressed $La_{3-x}Te_4$ exceeds that of UHS $La_{3-x}Te_4$ and SPS $LaTe_{1.46}$ at low temperature due to its considerably lower thermal conductivity. Between 500-1000 K, the ZT of UHS $La_{3-x}Te_4$ is about 70-75% that of the optimized $La_{3-x}Te_4$ samples due to the lower power factor resulting from the slower increase in its Seebeck coefficient with temperature.

Above ~800 K, the higher electrical resistivity of hot pressed $La_{3-x}Te_4$ (Figure 5.3) leads to a plateau in its power factor (Figure 5.4) while the power factor of UHS $La_{3-x}Te_4$ continues to

increase up to ~1000 K before plateauing and eventually decreasing slightly. Therefore, the ZT of UHS $La_{3-x}Te_4$ is similar to that of hot pressed $La_{3-x}Te_4$ at high temperature. By contrast, SPS $LaTe_{1.46}$ maintains a higher power factor above 1000 K such that its ZT value continues increasing at high temperature. UHS $La_{3-x}Te_4$ reaches a maximum ZT of 1.06 at 1273 K compared to a ZT of 1.13 for hot pressed $La_{3-x}Te_4$ [6] and 1.41 for SPS $LaTe_{1.46}$ [7,8] at the same temperature. These results indicate that the overall thermoelectric performance of UHS $La_{3-x}Te_4$ is comparable to that established for optimized $La_{3-x}Te_4$. This demonstration is remarkable and verifies that the material can be processed via rapid, pressure-less sintering while maintaining its proven high ZT value.

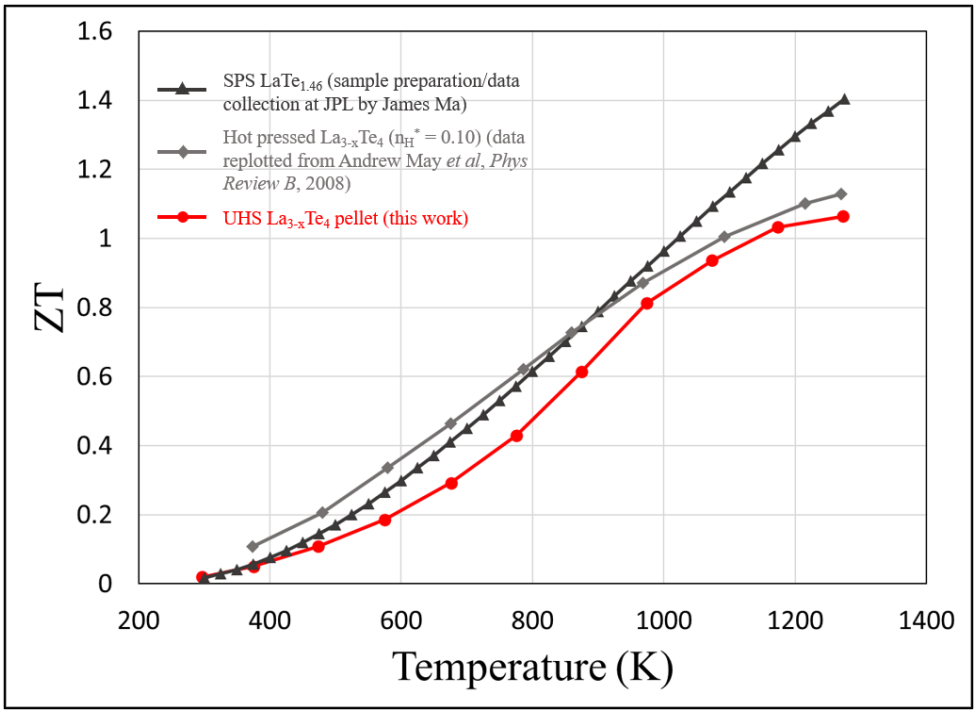

Figure 5.6: Temperature-dependent ZT values calculated for UHS $La_{3-x}Te_4$ pellet. $ZT = \frac{S^2\sigma}{\kappa}T$ was calculated from the values of Seebeck coefficient (S), electrical resistivity ($\rho = \frac{1}{\sigma}$), and thermal conductivity (κ) presented in Figure 5.2, Figure 5.3, and Figure 5.5, respectively. ZT values for bulk SPS $LaTe_{1.46}$ prepared at JPL by James Ma[8] and bulk hot-pressed $La_{3-x}Te_4$ at an optimized carrier concentration of $n_H^* = 0.10$ in the literature (Andrew May *et al*, *Physical Review B*, **78**, 2008)[2] are also shown for comparison.

5.4 Discussion of the Thermoelectric Performance of UHS $La_{3-x}Te_4$

The high thermoelectric performance exhibited by UHS $La_{3-x}Te_4$ is a significant accomplishment. It indicates that UHS achieves excellent bonding and densification in the material to attain proper electronic properties for thermoelectric performance. The Seebeck coefficient, which is independent of density and microstructure, confirms that the electronic structure of $La_{3-x}Te_4$ is not appreciably altered during UHS. However, a small fraction of Te sublimation may occur which slightly decreases the magnitude of Seebeck coefficient due to a small decrease in *x* value. Due to their similar Seebeck coefficient values, the performance of the UHS $La_{3-x}Te_4$ EPD thin films is expected to be comparable to that of bulk UHS $La_{3-x}Te_4$. Further optimization of thin film measurement techniques is necessary to accurately measure the electrical resistivity and thermal conductivity and confirm their thermoelectric performance.

The electrical resistivity of bulk UHS $La_{3-x}Te_4$, which depends on density, microstructure, and bonding, is lower than that of optimized $La_{3-x}Te_4$ samples. This result indicates that the bonding and microstructure of UHS $La_{3-x}Te_4$ are sufficient for efficient electronic transport despite samples having slightly lower density than those synthesized via hot pressing or SPS. The UHS process likely promotes strong sinter bonds between particles and well-defined grain boundaries which facilitates higher electron mobility. Additionally, the large micron-sized grains in UHS samples reduces the total number of grain boundaries which can further mitigate grain boundary scattering effects and enhance electronic conduction.[13–15] In this regard, UHS provides an interesting opportunity to study grain boundary scattering and grain-size dependence of electrical resistivity since it allows for preparation of $La_{3-x}Te_4$ samples with grain sizes that are significantly larger than those achieved during hot pressing or SPS.

The thermal conductivity of UHS $La_{3-x}Te_4$, which depends on structure, density, and electronic properties, is similar to that of SPS $LaTe_{1.46}$. While the electronic thermal conductivity of UHS $La_{3-x}Te_4$ is increased due to the lower electrical resistivity, the lattice thermal conductivity is decreased, leading to only a modest increase in total thermal conductivity compared to the SPS sample. The larger grain size of UHS samples is expected to increase lattice thermal conductivity via reduced grain boundary scattering[18,19], so the low lattice thermal conductivity may result from porosity-induced phonon scattering since UHS samples have lower density than those of SPS samples. This would also suggest that pores scatter phonons more strongly than they scatter electrons since the electrical resistivity of UHS $La_{3-x}Te_4$ is comparatively low.

Additionally, porosity scattering of phonons may be more significant than grain boundary scattering as the large grain size of UHS does not lead to a larger lattice thermal conductivity. However, more investigation into these relationships and scattering mechanisms is necessary to confirm the observed trends. If established, these grain size and porosity effects may provide a method for partially decoupling thermal conductivity and electrical resistivity by enhancing phonon scattering while preserving electron transport. However, the effects of porosity on the mechanical properties of the material cannot be ignored and are expected to reduce strength and fracture toughness.[8] Therefore, tuning the thermoelectric properties of $La_{3-x}Te_4$ with porosity could provide a basis for fundamental study of electron/phonon transport but likely would not be feasible for practical device applications.

UHS $La_{3-x}Te_4$ achieves comparable overall thermoelectric performance to hot pressed $La_{3-x}Te_4$ and SPS $LaTe_{1.46}$ as evidenced by its ZT of 1.06 at 1273 K. The ZT value is a consequence of the high power factor which results from the favorable combination of Seebeck

coefficient and electrical resistivity, as well as the limited increase in total thermal conductivity despite the lower electrical resistivity. The strong thermoelectric performance of UHS $La_{3-x}Te_4$ validates use of the technique for processing of both bulk $La_{3-x}Te_4$ samples and $La_{3-x}Te_4$ films. Furthermore, the ability to obtain dense $La_{3-x}Te_4$ samples with excellent thermoelectric performance via pressure-less sintering is a breakthrough for $La_{3-x}Te_4$ synthesis. UHS simplifies sintering of the material since it does not require complex equipment, loading procedures, or long sintering times, and it is applicable to three-dimensional sample geometries. Subsequent optimization can improve performance further by determining the sintering parameters necessary to achieve sample density >95% and addressing possible Te sublimation by starting with slight Te excess in the starting composition. Additionally, UHS can be applied to other thermoelectric materials systems since it is independent of materials properties.[20]

5.5 Summary and Conclusions

The thermoelectric performance of UHS $La_{3-x}Te_4$ samples was characterized and demonstrated have good agreement with that established for optimized $La_{3-x}Te_4$ samples prepared by hot pressing and SPS. Bulk UHS $La_{3-x}Te_4$ achieves a ZT of 1.06 at 1273 K which is within 5% of the ZT of 1.13 for hot pressed $La_{3-x}Te_4$.[6] The ZT of 1.41 for SPS $LaTe_{1.46}$ is slightly higher due to its increased power factor at high temperature.[7,8] Further optimization of the UHS process is expected to enable a ZT value closer to that of SPS $LaTe_{1.46}$.

Te sublimation during sintering is hypothesized to cause a slight change in composition to smaller x value, yielding $La_{3-x}Te_4$ that is more conductive with lower Seebeck coefficient than the optimized $LaTe_{1.46}$ composition. The change in x is expected to be <0.04 since the magnitude of Seebeck coefficient is larger than that of $LaTe_{1.42}$. The Seebeck coefficient of UHS $La_{3-x}Te_4$ indicates that the electronic configuration and degeneracy of the material are not altered during

sintering, and the low electrical resistivity indicates good bonding and densification. The large grain size of UHS samples may also facilitate electron transport by reducing grain boundary scattering effects. A slight increase in total thermal conductivity is attributed to an increase in the electronic thermal conductivity due to the lower resistivity of the sample. However, a calculated decrease in lattice thermal conductivity suppresses the increase in total thermal conductivity. The decrease in lattice thermal conductivity is unexpected due to the large grain size of the material and may be caused by porosity in the sample, though detailed investigation of the phonon/electron scattering mechanisms is necessary.

The synthesis of high performance $La_{3-x}Te_4$ via UHS represents a significant advancement of thermoelectric processing. Not only does UHS prepare dense $La_{3-x}Te_4$ samples in less than one minute, but it also maintains its excellent thermoelectric performance that is critical for efficient energy conversion. Pressure-less sintering of $La_{3-x}Te_4$ expands opportunities for device fabrication and fundamental study of properties by simplifying processing equipment, reducing sintering time and energy costs, and allowing for densification of complex geometries. Additionally, initial results indicate that the performance of UHS $La_{3-x}Te_4$ EPD films is similar to that of bulk UHS $La_{3-x}Te_4$. Future optimization of UHS and EPD can enable a reproducible, high-throughput processing scheme for sample synthesis and device fabrication. Furthermore, these techniques may be expanded to other thermoelectric material systems to enhance processing capabilities for the field as a whole.

5.6 References

(1) Fleurial, J. P. Thermoelectric Power Generation Materials: Technology and Application Opportunities. *JOM* **2009**, *61* (4), 79–85. https://doi.org/10.1007/S11837-009-0057-Z/METRICS.

(2) May, A. F.; Fleurial, J. P.; Snyder, G. J. Thermoelectric Performance of Lanthanum Telluride Produced via Mechanical Alloying. *Phys Rev B Condens Matter Mater Phys* **2008**, *78* (12), 125205. https://doi.org/10.1103/PHYSREVB.78.125205/FIGURES/11/MEDIUM.

(3) *mp-879: La3Te4 (Cubic, I-43d, 220)*. https://materialsproject.org/materials/mp-879/#properties (accessed 2023-05-15).

(4) Jain, A.; Ong, S. P.; Hautier, G.; Chen, W.; Richards, W. D.; Dacek, S.; Cholia, S.; Gunter, D.; Skinner, D.; Ceder, G.; Persson, K. A. Commentary: The Materials Project: A Materials Genome Approach to Accelerating Materials Innovation. *APL Mater* **2013**, *1* (1), 011002. https://doi.org/10.1063/1.4812323.

(5) Delaire, O.; May, A. F.; Mcguire, M. A.; Porter, W. D.; Lucas, M. S.; Stone, M. B.; Abernathy, D. L.; Ravi, V. A.; Firdosy, S. A.; Snyder, G. J. Phonon Density of States and Heat Capacity of La 3−x Te 4. https://doi.org/10.1103/PhysRevB.80.184302.

(6) May, A. High-Temperature Transport in Lanthanum Telluride and Other Modern Thermoelectric Materials, California Institute of Technology, Pasadena, 2010.

(7) Cheikh, D. Synthesis and Characterization of Rare-Earth Tellurides and Their Composites for High-Temperature Thermoelectric Applications, UCLA, Los Angeles, 2017.

(8) Ma, J. Improving the Mechanical Strength and Power Conversion Efficiency of High Temperature Thermoelectrics, UCLA, Los Angeles, 2014.

(9) Ma, J. M.; Clarke, S. M.; Zeier, W. G.; Vo, T.; Von Allmen, P.; Jeffrey Snyder, G.; Kaner, R. B.; Fleurial, J. P.; Bux, S. K. Mechanochemical Synthesis and High Temperature Thermoelectric Properties of Calcium-Doped Lanthanum Telluride La3−xCaxTe4. *J Mater Chem C Mater* **2015**, *3* (40), 10459–10466. https://doi.org/10.1039/C5TC01648G.

(10) Chi, S. chih. Novel Syntheses of Thermoelectric and Nanostructured Materials and a System for Purifying and Sorting Metallic and Semiconducting Single Walled Carbon Nanotubes in a Mixed Tube Suspension, Johns Hopkins, 2014. https://jscholarship.library.jhu.edu/handle/1774.2/37038 (accessed 2023-04-05).

(11) Zhao, D.; Qian, X.; Gu, X.; Jajja, S. A.; Yang, R. Measurement Techniques for Thermal Conductivity and Interfacial Thermal Conductance of Bulk and Thin Film Materials. *Journal of Electronic Packaging, Transactions of the ASME* **2016**, *138* (4). https://doi.org/10.1115/1.4034605/384410.

(12) Wood, C.; Zoltan, D.; Stapfer, G. Measurement of Seebeck Coefficient Using a Light Pulse. *Review of Scientific Instruments* **1985**, *56* (5), 719–722. https://doi.org/10.1063/1.1138213.

(13) Qiu, Q.; Liu, Y.; Xia, K.; Fang, T.; Yu, J.; Zhao, X.; Zhu, T.; Qiu, Q. Y.; Liu, Y. T.; Xia, K. Y.; Fang, T.; Yu, J. J.; Zhao, X. B.; Zhu, T. J. Grain Boundary Scattering of Charge Transport in N-Type (Hf,Zr)CoSb Half-Heusler Thermoelectric Materials. *Adv Energy Mater* **2019**, *9* (11), 1803447. https://doi.org/10.1002/AENM.201803447.

(14) Wu, Y.; Liu, F.; Zhang, Q.; Zhu, T.; Xia, K.; Zhao, X. Enhancing the Average Thermoelectric Figure of Merit of Elemental Te by Suppressing Grain Boundary Scattering. *J Mater Chem A Mater* **2020**, *8* (17), 8455–8461. https://doi.org/10.1039/D0TA02660C.

(15) Hu, C.; Xia, K.; Fu, C.; Zhao, X.; Zhu, T. Carrier Grain Boundary Scattering in Thermoelectric Materials. *Energy Environ Sci* **2022**, *15* (4), 1406–1422. https://doi.org/10.1039/D1EE03802H.

(16) Tritt, T. M.; Subramanian, M. A. Thermoelectric Materials, Phenomena, and Applications: A Bird's Eye View. *MRS Bull* **2006**, *31* (3), 188–194. https://doi.org/10.1557/MRS2006.44/METRICS.

(17) Kim, H. S.; Gibbs, Z. M.; Tang, Y.; Wang, H.; Snyder, G. J. Characterization of Lorenz Number with Seebeck Coefficient Measurement. *APL Mater* **2015**, *3* (4). https://doi.org/10.1063/1.4908244/14557427/041506_1_ACCEPTED_MANUSCRIPT.PDF.

(18) Toprak, M. S.; Stiewe, C.; Platzek, D.; Williams, S.; Bertini, L.; Müller, E.; Gatti, C.; Zhang, Y.; Rowe, M.; Muhammed, M. The Impact of Nanostructuring on the Thermal Conductivity of Thermoelectric CoSb3. *Adv Funct Mater* **2004**, *14* (12), 1189–1196. https://doi.org/10.1002/ADFM.200400109.

(19) Rowe, D. M.; Shukla, V. S. The Effect of Phonon-grain Boundary Scattering on the Lattice Thermal Conductivity and Thermoelectric Conversion Efficiency of Heavily Doped Fine-grained, Hot-pressed Silicon Germanium Alloy. *J Appl Phys* **1981**, *52* (12), 7421–7426. https://doi.org/10.1063/1.328733.

(20) Boldrini, S.; Ferrario, A.; Fasolin, S.; Miozzo, A.; Barison, S. Ultrafast High-Temperature Sintering and Thermoelectric Properties of n-Doped Mg2Si. *Nanotechnology* **2023**, *34* (15). https://doi.org/10.1088/1361-6528/ACB15A.

(21) Cheikh, D.; Hogan, B. E.; Vo, T.; Von Allmen, P.; Lee, K.; Smiadak, D. M.; Zevalkink, A.; Dunn, B. S.; Fleurial, J. P.; Bux, S. K. Praseodymium Telluride: A High-Temperature, High-ZT Thermoelectric Material. *Joule* **2018**, *2* (4), 698–709. https://doi.org/10.1016/J.JOULE.2018.01.013.

Chapter 6 Conclusions and Future Work

6.1 Oxidation Mechanism of $La_{3-x}Te_4$

In Chapter 2, temperature-dependent oxide formation in $La_{3-x}Te_4$ was studied and a detailed oxidation mechanism for the material was proposed. These results represent the first comprehensive investigation of the oxidation mechanism of $La_{3-x}Te_4$ and provide improved understanding of the process by which thermoelectric performance degrades. The oxide is non-passivating, and incomplete oxidation of the material at its surface produces changes in the bulk composition which harm thermoelectric performance. Since preparation of $La_{3-x}Te_4$ samples with minimal oxide are well-established for thermoelectric characterization, these results are most relevant for device fabrication which will be the next step in $La_{3-x}Te_4$ processing.

Service conditions will require extended exposure to temperatures >600^{o}C that can lead to oxidation even at low oxygen partial pressures. Since the oxide phases are thermodynamically favorable, device design should incorporate a combination of materials-based and environmental barrier approaches to mitigate oxidation through surface passivation and minimized oxygen exposure. Future research should focus on studying composite structures such as $La_{3-x}Te_4$-Ni that may enhance surface passivation as well as oxide prevention coatings such as aerogels to minimize oxygen exposure. Additionally, oxide formation in dense $La_{3-x}Te_4$ bulk pellets should be investigated and compared to that of the powder since dense pellets exhibit a higher stability in oxidizing conditions.[6]

6.2 Electrophoretic Deposition of $La_{3-x}Te_4$ Films

In Chapter 3, $La_{3-x}Te_4$ thin films were deposited on planar and non-planar substrates by electrophoretic deposition (EPD) of the as-synthesized powder suspended in THF. The ability to produce $La_{3-x}Te_4$ films significantly expands processing opportunities for the material. It allows

for exploration of the effects of thin film microstructure on thermoelectric performance and enables study of a wider range of inclusion morphologies for $La_{3-x}Te_4$-Ni composites structures.

The ability of EPD to fabricate complex components without requiring machining of bulk material expands the device architectures available to $La_{3-x}Te_4$. Since $La_{3-x}Te_4$ can be deposited on various metallic substrates without binder additives or bonding layers, EPD also potentially simplifies metallization steps during device fabrication. The versatility and scalability of EPD make it a promising technique for implementation as a high-throughput processing scheme for material synthesis and device fabrication. Furthermore, EPD can enable similar processing enhancements for other thermoelectric materials systems which will form other segments in the overall thermoelectric device. The fundamental study of the $La_{3-x}Te_4$/THF suspension and EPD properties can guide the selection of appropriate suspensions for those materials.

Future research should focus on additional characterization of the $La_{3-x}Te_4$/THF suspension and optimization of the EPD process. Experimental measurements of zeta potential and electrophoretic mobility should be performed to confirm the calculated values and proposed charging mechanisms. Thicker EPD coatings may be synthesized through optimization of the suspension and deposition cell to mitigate sedimentation effects. The EPD process should be applied to deposition of $La_{3-x}Te_4$ onto substrate geometries that are relevant for device manufacturing as well as Ni substrates that are directly of interest for composite study such as Ni nanowire arrays.

6.3 Ultrafast High-Temperature Sintering of $La_{3-x}Te_4$

In Chapter 4, ultrafast high-temperature sintering (UHS) was utilized to achieve rapid, pressure-less densification of $La_{3-x}Te_4$ EPD films and bulk cold-pressed pellets. Rapid

densification results from the extremely high heating rate associated with UHS which minimizes low-temperature coarsening and quickly activates grain boundary diffusion which produces rapid densification.

The first-time demonstration of rapid, pressure-less sintering of $La_{3-x}Te_4$ is remarkable and provides the foundation for simplifying synthesis of the material and reducing processing time/cost. Pressure sintering techniques such as hot pressing and spark plasma sintering, which involve complex equipment and loading procedures, are not required for densification. Free sintering of $La_{3-x}Te_4$ allows for more facile and high-throughput processing and expands the geometries which can be sintered. Since the $La_{3-x}Te_4$ grain size is controlled by sintering parameters, UHS also provides an opportunity to study the effects of grain size on thermoelectric performance. Additionally, these results represent the first application of UHS to films prepared via EPD, and the unique combination of EPD and UHS creates a novel high throughput processing scheme. Lastly, since UHS does not depend on material properties, it can be applied to other high-temperature thermoelectric materials to improve overall device fabrication.

Future work should focus on additional fundamental study of the UHS process as well as optimization of the experimental setup. A broader study of the influence of UHS temperature, time, and heating rate on the microstructure of $La_{3-x}Te_4$ should be performed to verify the mechanisms of rapid densification and improve the established relationship between UHS parameters and $La_{3-x}Te_4$ microstructure. The possibility of UHS inducing a non-equilibrium flash sintering state in the material should also be explored. The experimental setup of UHS should be optimized by using thermal insulation to ensure uniform sample heating and minimize radiative heating losses as well as more rigorously define the relationship between applied current and

sample temperature.[8] Application of UHS to other high-temperature thermoelectric materials should be explored.

6.4 Thermoelectric Properties of UHS $La_{3-x}Te_4$

In Chapter 5, the thermoelectric performance of bulk UHS $La_{3-x}Te_4$ was characterized and compared to that of optimized $La_{3-x}Te_4$ prepared by hot pressing and SPS. Bulk UHS $La_{3-x}Te_4$ achieves similar overall thermoelectric performance to those established for the material. Initial measurements of power factor up to 573K show promising performance for UHS EPD $La_{3-x}Te_4$ films on BN, though improved thin film measurement techniques are needed.

Demonstration of exceptional thermoelectric performance for UHS $La_{3-x}Te_4$ is a major validation of the sintering technique. These results verify that bulk and EPD $La_{3-x}Te_4$ can be densified in seconds while maintaining the thermoelectric properties of the material. The ability to produce dense samples in seconds with excellent thermoelectric performance reduces synthesis time, cost, and complexity, which dramatically improves processing. UHS also achieves these results despite the high sintering temperatures and oxygen sensitivity of $La_{3-x}Te_4$ and is therefore a significant breakthrough for $La_{3-x}Te_4$ and other high-temperature thermoelectric materials.

Future research should focus on further optimization and characterization of UHS. Electron/phonon transport and scattering mechanisms in the material should be investigated to establish better fundamental understanding. Full characterization of UHS $La_{3-x}Te_4$ EPD film performance will require improved thin film measurement techniques and selection of an appropriate insulating substrate material facilitate measurements while minimizing film cracking. The process can then be extended to complex $La_{3-x}Te_4$ coating geometries for characterization of novel composite and device structures. Finally, UHS and EPD can be applied to other

thermoelectric materials for enhanced processing of a wide range of material systems that can improve overall device fabrication.

6.5 References

(1) May, A. High-Temperature Transport in Lanthanum Telluride and Other Modern Thermoelectric Materials. Pasadena 2010.

(2) May, A. F.; Fleurial, J. P.; Snyder, G. J. Thermoelectric Performance of Lanthanum Telluride Produced via Mechanical Alloying. *Phys Rev B Condens Matter Mater Phys* **2008**, *78* (12), 125205. https://doi.org/10.1103/PHYSREVB.78.125205/FIGURES/11/MEDIUM.

(3) Cheikh, D. Synthesis and Characterization of Rare-Earth Tellurides and Their Composites for High-Temperature Thermoelectric Applications. Los Angeles 2017.

(4) Ma, J. Improving the Mechanical Strength and Power Conversion Efficiency of High Temperature Thermoelectrics. Los Angeles 2014.

(5) Ma, J. M.; Clarke, S. M.; Zeier, W. G.; Vo, T.; Von Allmen, P.; Jeffrey Snyder, G.; Kaner, R. B.; Fleurial, J. P.; Bux, S. K. Mechanochemical Synthesis and High Temperature Thermoelectric Properties of Calcium-Doped Lanthanum Telluride La3−xCaxTe4. *J Mater Chem C Mater* **2015**, *3* (40), 10459–10466. https://doi.org/10.1039/C5TC01648G.

(6) Delaire, O.; May, A. F.; Mcguire, M. A.; Porter, W. D.; Lucas, M. S.; Stone, M. B.; Abernathy, D. L.; Ravi, V. A.; Firdosy, S. A.; Snyder, G. J. Phonon Density of States and Heat Capacity of La 3−x Te 4. https://doi.org/10.1103/PhysRevB.80.184302.

(7) Talebi, T.; Ghomashchi, R.; Talemi, P.; Aminorroaya, S. Suspension Characteristics and Electrophoretic Deposition of p -Type Bi 2 Te 3 Films for Thermoelectric Applications. *J Electrochem Soc* **2018**, *165* (9), D364–D369. https://doi.org/10.1149/2.0301809JES/XML.

(8) Dong, J.; Pouchly, V.; Biesuz, M.; Tyrpekl, V.; Vilémová, M.; Kermani, M.; Reece, M.; Hu, C.; Grasso, S. Thermally-Insulated Ultra-Fast High Temperature Sintering (UHS) of Zirconia: A Master Sintering Curve Analysis. *Scr Mater* **2021**, *203*, 114076. https://doi.org/10.1016/J.SCRIPTAMAT.2021.114076.

Appendix A Supporting Information for Chapter 2 (Oxidation Mechanism of $La_{3-x}Te_4$)

A.1 Detailed XPS Analysis

XPS was employed to analyze the surface species of as-synthesized powder at room temperature. Figure 2.2 shows the XPS spectra for the La 3d, Te 3d, O 1s, and C 1s regions. The La 3d signal (Figure 2.2A) exhibits spin-orbit and multiplet splitting (four components corresponding to one valence state) which is consistent with La in the 3+ state.[1] There are two main components at 834.4 eV and 851.2 eV, with respective satellite components at 837.9eV and 854.7eV. These values are tabulated in Table 0.1 where they are compared to literature values. Since La is almost always reported in the 3+ state in literature, this result by itself is not unique to any specific compounds or species. The binding energy values are similar to literature for La_2Te_3 nanowires which suggests La-Te bonding and is consistent with La^{3+} existing in $La_{3-x}Te_4$.[2] However, the binding energy difference of 3.5eV between the main and satellite components suggests the presence of carbonate species as well.[1]

Table 0.1. Binding energy values for La 3d components with comparison to literature.

	La $3d_{5/2}$ (main)	**La $3d_{5/2}$ (satellite)**	**La $3d_{3/2}$ (main)**	**La $3d_{3/2}$ (satellite)**
$La_{3-x}Te_4$ powder (this work)	834.4eV	837.9eV	851.2eV	854.7eV
La_2Te_3 nanowires ([11])	834.7eV	838.0eV	851.5eV	854.9eV

The Te 3d signal (Figure 2.2B) exhibits three cases of spin-orbit splitting (six components corresponding to three valence states), which are consistent with Te^{2-}, Te^{4+}, and Te^0.[3] The binding energy values are tabulated in Table 0.2 along with comparisons to literature. The strongest components at 572.0eV and 582.4eV are attributed to Te^{2-} which exists in $La_{3-x}Te_4$ and is

associated with La-Te bonding. The weaker components at 575.4eV and 585.8eV are attributed to Te^{4+} which is typically present in TeO_2 and is associated with Te-O bonding. The binding energy values for Te^{2-} and Te^{4+} are similar to literature for La_2Te_3 nanowires in which a surface oxide was also observed.[2] The asymmetry of the Te^{2-} peaks is accounted for by fitting two additional components at 572.8eV and 583.2eV which are attributed to Te metal (Te^0). Te metal is often observed in conjunction with oxide as a stable intermediate in the first step of tellurium oxidation.[4, 5, 6, 7, 8] The presence of tellurium oxide is further confirmed in the O 1s signal (Figure 2.2C), where the component at 530.7eV is attributed to Te-O bonding. The assignment of this peak is informed by the work of Kong *et al* with TeO_x thin films in which they observed a peak in the O 1s spectrum between 530.4-531.0eV.[5]

Table 0.2. Binding energy values for Te 3d components with comparison to literature.

	Te $3d_{5/2}$			**Te $3d_{3/2}$**		
	Te^{2-}	Te^0	Te^{4+}	Te^{2-}	Te^0	Te^{4+}
$La_{3-x}Te_4$ powder (this work)	572.0eV	572.8eV	575.4eV	582.4eV	583.2eV	585.8eV
La_2Te_3 nanowires (reference)	571.6eV (La_2Te_3 nanowires[11])	573.2eV (Pt_3Te_4 [9])	575.6eV (La_2Te_3 nanowires[11])	582.0eV (La_2Te_3 nanowires[11])	583.5eV (Pt_3Te_4 [9])	586.1eV (La_2Te_3 nanowires[11])

Analysis of the O 1s (Figure 2.2C) region provides additional evidence of hydroxide and carbonate species as suggested by the La 3d region. The components in the O 1s region at 531.7eV and 532.7eV are attributed to hydroxyl groups (-OH) and carbonate groups $(-CO_3)^{2-}$, respectively.[9] On a pure La_2O_3 surface, hydroxide ($La(OH)_3$) and carbonate ($La_2O_2CO_3$) compounds are expected to form as a result of exposure to moisture and CO_2.[10, 11] An atmosphere-exposed La_2O_3 surface is known to rapidly hydroxylate at room temperature,

forming $La(OH)_3$ and small amounts of oxycarbonate ($La_2O_2CO_3$).[11] Li *et al* treated the surface of La_2O_3 samples with water and observed a component in the O 1s region at 531.8eV which they attributed to $La(OH)_3$.[10] In the same study, they treated the surface of La_2O_3 samples with CO_2 and observed a component in the O 1s region at 532.6eV which was attributed to $La_2O_2CO_3$.[10] These values are very close to the components attributed to hydroxide (531.7eV) and carbonate (532.7eV), respectively, for the as-synthesized $La_{3-x}Te_4$ surface. However, there is the lack of a peak associated with La-O bonding, which would be expected at 528.6eV.[1] This result suggests that hydroxylation and carbonation at the surface are incomplete and, unlike pure La_2O_3, also involve Te such that there is a partially hydroxylated and carbonated lanthanum telluride surface.

Further analysis of the C 1s region (Figure 2.2D) confirms the presence of carbonate species, where the component at 285.8eV is associated with C-O bonding and the component at 288.7eV is associated with C=O bonding.[12] The peak at 284.8eV is adventitious carbon which is used for binding energy reference.[12] Li *et al* observed a C 1s component at 290.6eV after CO_2 treatment of the La_2O_3 surface which was associated with carbonate.[10] This value is higher than the components seen for as-synthesized $La_{3-x}Te_4$, and Li *et al* observed components at 285.9eV and 287.9eV on the surface of clean La_2O_3 which were attributed to incompletely oxidized carbon species (C-O-C and C=O).[10] The component at 288.7eV for as-synthesized $La_{3-x}Te_4$ lies between the 287.9eV value for incompletely oxidized carbon and 290.6eV for carbonate in literature, which suggests a mix between the two. Fleming *et al* observed a C 1s component at 289.0eV for La_2O_3 exposed to atmosphere at room temperature[11], which is much closer to the value of 288.7eV for $La_{3-x}Te_4$ powder. These results provide further evidence that the

carbonation reaction on the $La_{3-x}Te_4$ surface is incomplete and is consistent with a partially carbonated surface.

A.2 Mass change of $La_{3-x}Te_4$ powder after oxidation and oxygen exposure calculations

Mass change of $La_{3-x}Te_4$ powder after oxidation at 1000°C

Table 0.3 shows the experimentally measured mass change of 50 mg of $La_{3-x}Te_4$ powder after heat treatment in flowing forming gas at 1000°C for 2 hours. The mass of the oxidized powder was 27.8 mg after heat treatment, corresponding to a measured mass loss of 22.2 mg. This mass change informs assignment of the overall oxidation reaction as:

$$10\ La_3Te_4 + 21\ O_2 \rightarrow 12\ La_2O_3\ (\text{glass}) + 3\ La_2O_2Te\ (\text{crystalline}) + 37\ Te\ (\text{vapor}) \qquad \text{(Equation 0.1)}$$

The calculated mass loss for (Equation 0.1, assuming 50 mg of $La_{3-x}Te_4$, is 21.8 mg, which agrees well with the experimentally measured mass change. This result indicates a significant amount of glassy La_2O_3 is present after oxidation in addition to the crystalline La_2O_2Te identified in XRD.

Table 0.3 Experimental and calculated mass change of $La_{3-x}Te_4$ after 1000°C heat treatment.

Initial mass of La_3Te_4	**Measured mass of La_2O_2Te (heat treat at 1000°C 2 hrs)**	**((Equation 0.1) Calculated mass of La_2O_3 (glass) + La_2O_2Te**
50 mg	27.8 mg (Decrease of 22.2 mg)	28.2 mg (Decrease of 21.8 mg)

Calculation of oxygen exposure

The amount of oxygen required for (Equation 0.1 was calculated to estimate the oxygen exposure during heat treatment. For a starting mass of 50 mg of La_3Te_4, 1.13×10^{-4} mols of O_2 are required for the completion of the reaction in (Equation 0.1. For a nominal O_2 concentration of 1 ppm in the forming gas [35] and a flow rate of 15 mL/min, 7.36×10^{-8} mols of O_2 pass through the tube furnace in 2 hours (dwell time) and 4.41×10^{-7} mols of O_2 pass through in 12 hours

(total heat treatment time at 1000ºC including ramp rate). This calculation indicates that trace oxygen in the forming gas alone is insufficient to cause the extent of oxidation observed. An O_2 concentration on the order of 100-1000ppm would be sufficient to cause severe oxidation and may be due to oxygen in the tube from inadequate purging or a small leak in the furnace.

A.3 Detailed $La_{3-x}Te_4$ Oxidation Mechanism

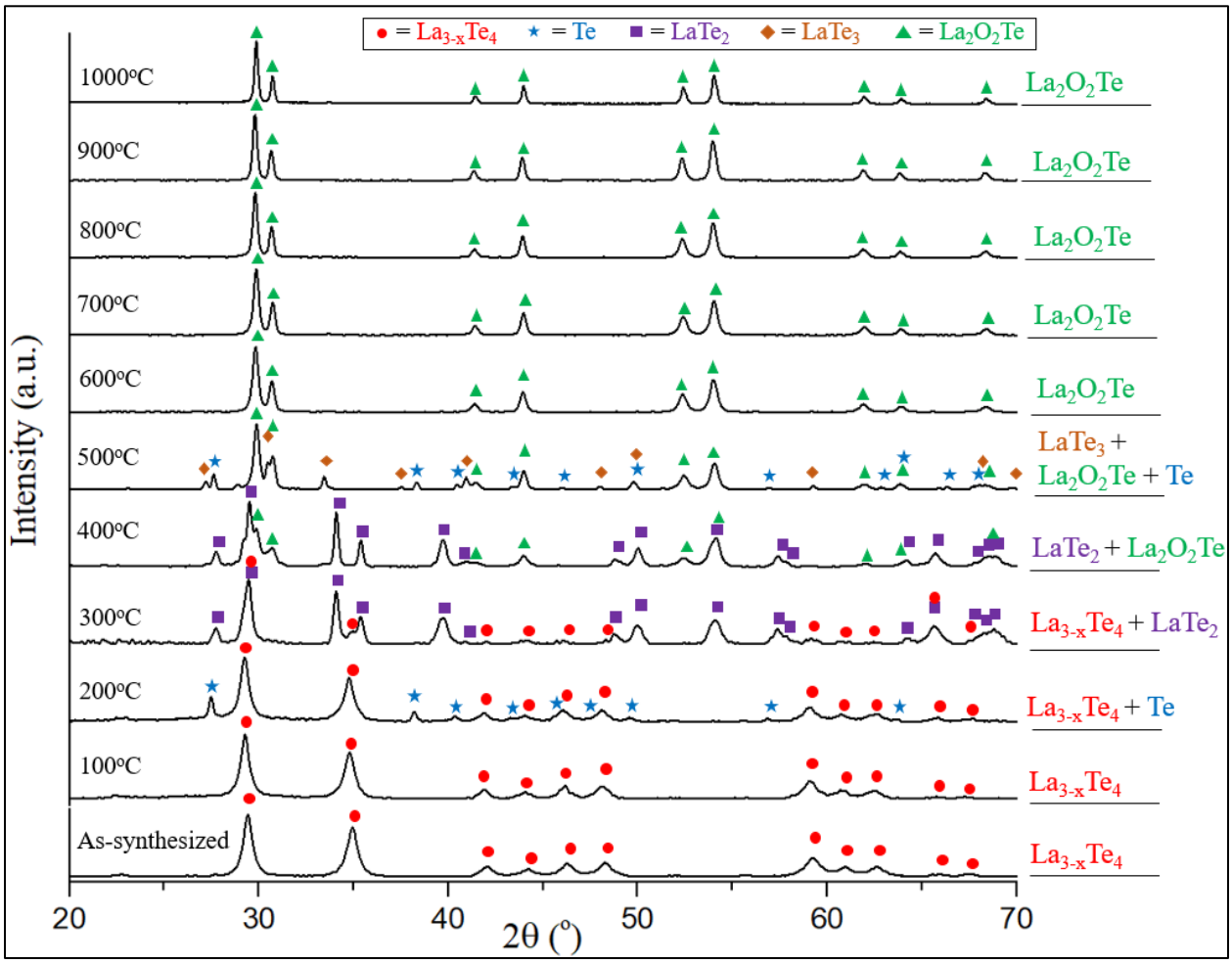

Figure 0.1: XRD scans for $La_{3-x}Te_4$ powder after tube furnace heat treatment for 2 hours in flowing forming gas 95% Ar, 5% H_2. The temperatures for each heat treatment are listed on the left, and identified phases associated with the scan for that heat treatment temperature are listed on the right.

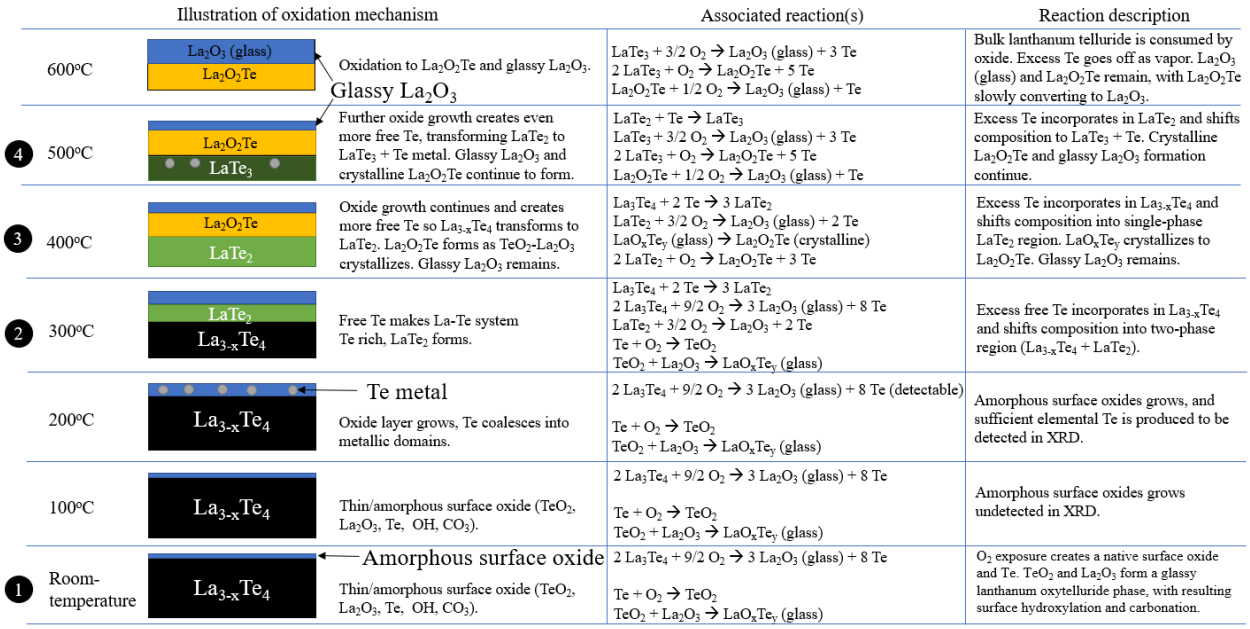

Figure 0.2. Illustration of the $La_{3-x}Te_4$ oxidation mechanism. Included are proposed reactions associated with observed XRD phases. Points 1-4 are used to qualitatively reference the oxidation mechanism to the phase diagram (Figure 2.6B) and show how the formation of Te causes the bulk lanthanum telluride to become Te-rich.

Figure 0.2 illustrates the $La_{3-x}Te_4$ oxidation mechanism in detail. Associated chemical reactions are proposed from observed XPS species and phase changes in XRD as well as knowledge of the La-Te phase diagram. Below, the chemical reactions are discussed for each heat treatment temperature for ease of reference to Figure 0.1 and Figure 0.2, though it should be noted that the oxide progression is also expected to occur kinetically (Figure 0.3) and the processes can likewise be referenced to longer heat treatment times at a given temperature. For simplicity of writing the reactions, the lanthanum telluride stoichiometry is assumed to be La_3Te_4 for the solid solution existing from 57-60 at% Te and $LaTe_2$ for the solid solution existing from 63-67 at% Te.

Room temperature to 100°C

As shown in Figure 2.3 and Figure 0.2, oxidation at room temperature leads to the formation of an amorphous surface oxide. Initial oxygen exposure creates La_2O_3 and elemental Te:

$$2\ La_3Te_4 + 9/2\ O_2 \rightarrow 3\ La_2O_3 + 8\ Te \qquad \text{(Equation 0.2)}$$

Some of the Te from (Equation 0.2 eventually reacts with oxygen to form TeO_2, which subsequently forms a glassy phase with La_2O_3 which likely exists as an amorphous lanthanum oxytelluride phase (LaO_xTe_y):

$$Te + O_2 \rightarrow TeO_2 \qquad \text{(Equation 0.3)}$$

$$TeO_2 + La_2O_3 \rightarrow LaO_xTe_y\ (glass) \qquad \text{(Equation 0.4)}$$

The oxides are sensitive to moisture and CO_2 and will rapidly react to form a partially hydroxylated and carbonated surface which is observed in XPS. Additionally,

200°C

The oxidation reactions in (Equation 0.2,(Equation 0.3, and (Equation 0.4 continue until sufficient elemental Te forms and coalesces into domains large enough to be observable in XRD.

300°C

The free Te formed from the oxidation reactions incorporates into the $La_{3-x}Te_4$ matrix and makes it more Te-rich. This pushes the composition into the two-phase region between La_3Te_4 and $LaTe_2$ (between 60-63 at% Te) such that some La_3Te_4 transforms to $LaTe_2$:

$$La_3Te_4 + 2\ Te \rightarrow 3\ LaTe_2 \qquad \text{(Equation 0.5)}$$

Oxidation of La_3Te_4 continues via (Equation 0.2 and additional oxidation of the $LaTe_2$ phase can proceed via the reaction:

$$LaTe_2 + 3/2\ O_2 \rightarrow La_2O_3 + 2\ Te \qquad \text{(Equation 0.6)}$$

Subsequent growth of the amorphous surface oxide continues via (Equation 0.3 and (Equation 0.4.

400°C

Further formation of Te continues to make the lanthanum telluride matrix more Te-rich such that the composition enters the single-phase $LaTe_2$ region (Equation 0.5). Additionally, the glassy LaO_xTe_y phase crystallizes at this temperature such that crystalline La_2O_2Te is observed in XRD:

$$LaO_xTe_y\ (glass) \rightarrow La_2O_2Te\ (crystalline) \qquad \text{(Equation 0.7)}$$

According to (Equation 0.1, glassy La_2O_3 is still present at higher temperature in addition to crystalline La_2O_2Te. The presence of glassy La_2O_3 is due to the thermodynamic driving force in which La_2O_3 is the most stable state, so some of the La_2O_2Te subsequently converts to La_2O_3:

$$La_2O_2Te + 1/2\ O_2 \rightarrow La_2O_3\ (glass) + Te \qquad \text{(Equation 0.8)}$$

Since Te has high mobility and is volatile at higher temperature, a significant portion of the elemental Te produced likely sublimates or incorporates into the matrix faster than it is oxidized to TeO_2. Therefore, additional glassy La_2O_3 formation may occur via (Equation 0.2, (Equation 0.6, and (Equation 0.11. Furthermore, La_2O_2Te may also form through direct reaction of O_2 with $LaTe_2$:

$$2\ LaTe_2 + O_2 \rightarrow La_2O_2Te + 3\ Te \qquad \text{(Equation 0.9)}$$

500°C

Incorporation of Te formed from oxidation (Equation 0.6 and (Equation 0.9 into the lanthanum telluride matrix causes the composition to become Te-rich enough to reach the $LaTe_3$ composition (75 at% Te):

$$LaTe_2 + Te \rightarrow LaTe_3 \quad \text{(Equation 0.10)}$$

Reaction of $LaTe_3$ with oxygen produces glassy La_2O_3 and Te:

$$LaTe_3 + 3/2\ O_2 \rightarrow La_2O_3\ (glass) + 3\ Te \quad \text{(Equation 0.11)}$$

La_2O_2Te may also result from direct reaction of $LaTe_3$ with oxygen:

$$2\ LaTe_3 + O_2 \rightarrow La_2O_2Te + 5\ Te \quad \text{(Equation 0.12)}$$

600°C

Oxidation of remaining $LaTe_3$ to glassy La_2O_3 and crystalline La_2O_2Te occurs via (Equation 0.11 and (Equation 0.12 and any remaining excess Te is given off as vapor. Transformation of La_2O_2Te to La_2O_3 continues via (Equation 0.8.

A.4 Kinetic Aspects of $La_{3-x}Te_4$ Oxidation

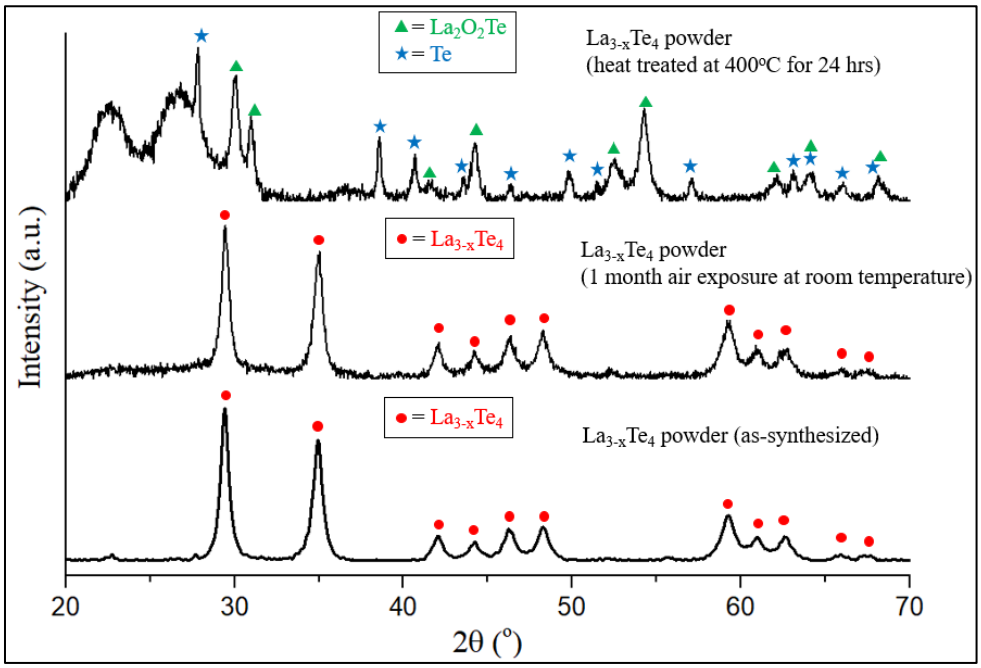

Figure 0.3. XRD scans of: (Top) $La_{3-x}Te_4$ powder after tube furnace heat treatment for 24 hours at 400°C in flowing forming gas (95% Ar, 5% H_2). The two broad features below 26° are due to the sample holder; (Middle) $La_{3-x}Te_4$ powder after one month of air exposure at room temperature; (Bottom) as-synthesized $La_{3-x}Te_4$ powder.

In Figure 0.3, the identified phases after the heat treatment at 400ºC for 24 hours are La_2O_2Te and Te. These products are similar to the products of heat treatment at 600ºC for 2 hours and indicative of late-stage oxidation before Te sublimates. This result highlights that the higher temperature heat treatments in Figure 0.1 speed up the kinetics of oxidation, allowing the stages of oxidation to be systematically observed in a shorter time period. After 1 month of air exposure, $La_{3-x}Te_4$ is the only phase identified in XRD, showing that the oxide does not crystallize or fully consume the powder at room temperature after long-term exposure. The XRD scan for the as-synthesized powder is smooth while the scans for the powder after heat treatment at 400ºC for 24 hours and after 1 month of air exposure have more noise and a slightly rougher baseline. These features are likely caused by the presence of glassy oxide phases (LaO_xTe_y at room temperature and La_2O_3 at 400ºC).

A.5 Effect of oxidation on electrical conductivity of $La_{3-x}Te_4$ and $La_{3-x}Te_4$/Ni

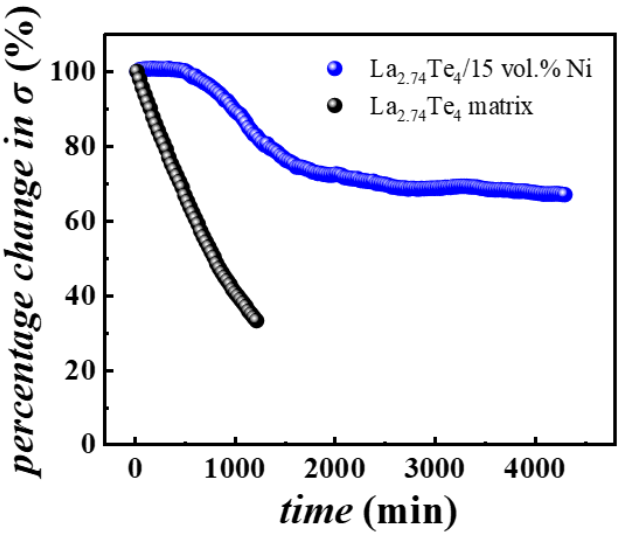

Figure 0.4. (Reprinted from Acta Materialia 224, Li *et al*, Enhanced thermal stability and oxidation resistance in $La_{3-x}Te_4$ by compositing metallic nickel particles, Copyright (2022)[21]). Percentage change in electrical conductivity as a function of time for $La_{2.74}Te_4$ and $La_{2.74}Te_4$/15 vol.% Ni composite exposed to 1 kPa oxygen partial pressure at 1000K.

Measurements for *S* and *k* are not shown because the researchers noted that pure $La_{2.74}Te_4$ samples "crash" in their measurement system above 700K due to oxidation. This issue could not be solved even by flushing the system with high purity argon which highlights the oxygen sensitivity of $La_{3-x}Te_4$.

A.6 References

(1) *Lanthanum | XPS Periodic Table | Thermo Fisher Scientific - US*. https://www.thermofisher.com/us/en/home/materials-science/learning-center/periodic-table/lanthanide-rare-earth/lanthanum.html (accessed 2023-03-06).

(2) Samal, A. K.; Pradeep, T. Lanthanum Telluride Nanowires: Formation, Doping, and Raman Studies. *Journal of Physical Chemistry C* **2010**, *114* (13), 5871–5878. https://doi.org/10.1021/JP911658K/SUPPL_FILE/JP911658K_SI_001.PDF.

(3) *Tellurium | Periodic Table | Thermo Fisher Scientific - US*. https://www.thermofisher.com/us/en/home/materials-science/learning-center/periodic-table/metalloid/tellurium.html (accessed 2023-03-06).

(4) Samal, A. K.; Pradeep, T. Pt3Te4 Nanoparticles from Tellurium Nanowires. *Langmuir* **2010**, *26* (24), 19136–19141. https://doi.org/10.1021/LA103466J/SUPPL_FILE/LA103466J_SI_001.PDF.

(5) Kong, H.; Yeo, J. Bin; Lee, H. Y. A Study on the Properties of Tellurium-Oxide Thin Films Based on the Variable Sputtering Gas Ratio. *Journal of the Korean Physical Society* **2015**, *66* (11), 1744–1749. https://doi.org/10.3938/JKPS.66.1744/METRICS.

(6) Kotina, I. M.; Tukhkonen, L. M.; Patsekina, G. V.; Shchukarev, A. V.; Gusinskii, G. M. Study of CdTe Etching Process in Alcoholic Solutions of Bromine. *Semicond Sci Technol* **1998**, *13* (8), 890. https://doi.org/10.1088/0268-1242/13/8/011.

(7) Neudachina, V. S.; Shatalova, T. B.; Shtanov, V. I.; Yashina, L. V.; Zyubina, T. S.; Tamm, M. E.; Kobeleva, S. P. XPS Study of SnTe(1 0 0) Oxidation by Molecular Oxygen. *Surf Sci* **2005**, *584* (1), 77–82. https://doi.org/10.1016/J.SUSC.2005.01.061.

(8) Badrinarayanan, S.; Mandale, A. B.; Sinha, A. P. B. Photoelectron Spectroscopy Study of Surface Oxidation of SnTe PbTe and PbSnTe. *Mater Chem Phys* **1984**, *11* (1), 1–14. https://doi.org/10.1016/0254-0584(84)90084-1.

(9) *Oxygen | XPS Periodic Table | Thermo Fisher Scientific - US*. https://www.thermofisher.com/us/en/home/materials-science/learning-center/periodic-table/non-metal/oxygen.html (accessed 2023-03-06).

(10) Li, J. P. H.; Zhou, X.; Pang, Y.; Zhu, L.; Vovk, E. I.; Cong, L.; Van Bavel, A. P.; Li, S.; Yang, Y. Understanding of Binding Energy Calibration in XPS of Lanthanum Oxide by in Situ Treatment.

Physical Chemistry Chemical Physics **2019**, *21* (40), 22351–22358. https://doi.org/10.1039/C9CP04187G.

(11) Fleming, P.; Farrell, R. A.; Holmes, J. D.; Morris, M. A. The Rapid Formation of La(OH)3 from La2O3 Powders on Exposureto Water Vapor. *Journal of the American Ceramic Society* **2010**, *93* (4), 1187–1194. https://doi.org/10.1111/J.1551-2916.2009.03564.X.

(12) *Carbon | XPS Periodic Table | Thermo Fisher Scientific - US*. https://www.thermofisher.com/us/en/home/materials-science/learning-center/periodic-table/non-metal/carbon.html (accessed 2023-03-06).

(13) *Airgas Product Catalog*. https://www.airgas.com/airgascatalog/catalog/index.html (accessed 2023-03-06).

(14) *La-Te Binary Phase Diagram (1990 Okamoto H.)*. ASM Alloy Phase Diagram Database. https://matdata.asminternational.org/apd/viewPicture.aspx?dbKey=grantami_apd&id=10713366&revision=399310# (accessed 2023-03-06).

(15) Li, J.; Liu, R.; Song, Q.; Gao, Z.; Huang, H.; Zhang, Q.; Shi, X.; Bai, S.; Chen, L. Enhanced Thermal Stability and Oxidation Resistance in La3-XTe4 by Compositing Metallic Nickel Particles. *Acta Mater* **2022**, *224*, 117526. https://doi.org/10.1016/J.ACTAMAT.2021.117526.